Exoplanet Transit Follow-Up Tool

Author:
Luke Robson

Supervised by:
Professor Hugh Jones
Professor William Martin
Dr Ronny Errmann

Centre for Astrophysics Research School of Physics, Astronomy and Mathematics
University of Hertfordshire

Submitted to the University of Hertfordshire in partial fulfilment of the requirements of the degree of Master of Science by Research

March 2020

Abstract

This thesis describes the development of a website called the Transit Follow Up Tool (https://observatory.herts.ac.uk/exotransitpredict) in order to plan exoplanet transit observations. Website models have been developed to predict the photometric precision for observations using telescopes from the University of Hertfordshire's Bayfordbury Observatory, Thai Robotic Telescope Spring Brook Observatory, Thai National Telescope and the Open University PIRATE facility. The website can predict the transit times for exoplanets and TESS objects of interest (TOI) and predict the precision that would be achieved. Ten transits have been recorded during the thesis, four of these are TOIs. For the confirmed exoplanets, two transits for HAT-P-20 b and single transits for HAT-P-44b, KPS-1 b, WASP-12 b and WASP-52 b were recorded. The TESS Objects of interest 516.01, 689.01, 1164.01 and 1455.01 were all found to be false positives. The predictions of uncertainty for the transit fit are within 0.1 ppt over nine of the transits for six different telescope setups. The transit fits are within the expected literature results. Much of the work has been concerned with improvement of observing procedures for different telescopes and in particular calibration measurements. For example, comparing the predicted uncertainty for the PIRATE telescope over 1x1 and 2x2 binning, it is found that 2x2 is always better by around 20%. It was also found that precision in mmag could be improved by approximately 5-20% depending on the combination of exposure time and magnitude combination due to underexposed flat field images.

Declaration

I declare that no part of this work is being submitted concurrently for another award of the University or any other awarding body or institution. This thesis contains a substantial body of work that has not previously been submitted successfully for an award of the University or any other awarding body or institution

Sections 2.1 and 2.2 have been published Beck, P., Robson, L. et al. (June 2019). "Efficient Follow-up of Exoplanet Transits Using Small Telescopes". In: Publications of the Astronomical Society of the Pacific, 131.1002 doi:10.1088/1538-3873/ab1eb4. This work was started by Peter Beck who unfortunately died after an extended period of illness during the preparation of the final manuscript. In this thesis, Section 2.2 has been expanded and contains new information whereas Section 2.1 contains most of the same information as in the paper but presented in a slightly different way.

Except where indicated otherwise in the submission, the submission is my own work and has not previously been submitted for any award.

Contents

List of Figures

List of Tables

1 Introduction

1.1 Basic Concepts

Exoplanets are planets that orbit other stars. When they transit they pass in front of the star from the observer's point of view blocking out some of the light. The change in brightness can indicate the size ratio of the star and the exoplanet. Photometry is the technique of measuring the brightness of astronomical objects.

Exoplanet History

Alex Wolszczan and Dale Frail found the first exoplanet on January 9, 1992 (Wolszczan and Frail 1992) although Latham first proposed a candidate exoplanet in 1989 (Latham et al. 1989). There are various ways to detect exoplanets like radial velocity, astrometry, pulsar timing, gravitational microlensing and transits.

The transit technique has been the most powerful tool at detecting exoplanets as more than 75 % of all known exoplanets have been detected using this method[1].

There are problems with this method as the orbit needs to be aligned in a way that the transit can be viewed from the observer's prospective. So only a small number of the total exoplanets that are out there in the galaxy are visible through this method.

In order to measure the transit depth, a suitable period of observation is needed when the transit is not occurring. This is ideally done before and after the transit has occurred. This period is most commonly known as the off-transit time.

There are two notable periods: just after the start of the transit and the other is just before the end of a transit. This is when not all of the exoplanet is in front of the star from the observer's perspective. They are called ingress and egress respectively. Figure 1.1 shows how the flux from the planetary system changes over the period of the planet's orbit.

[1] https://exoplanetarchive.ipac.caltech.edu/cgi-bin/TblView/nph-tblView?app=ExoTbls&config=planets

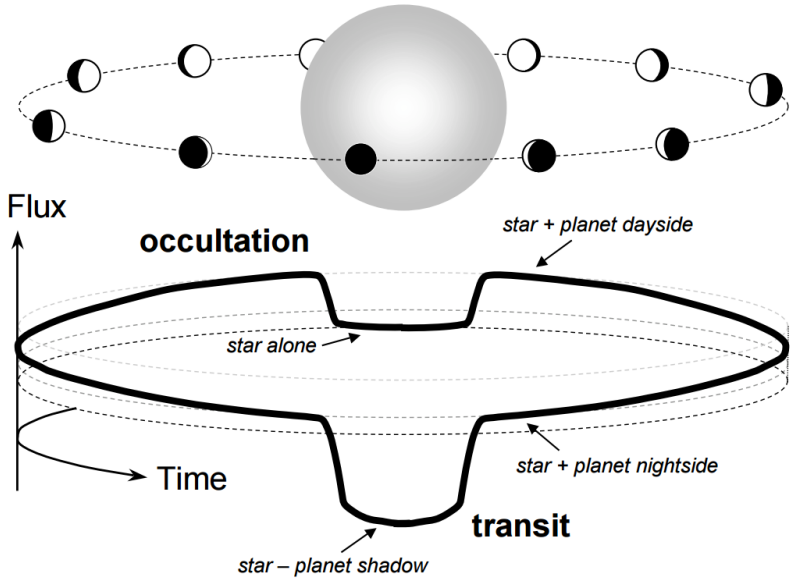

Figure 1.1: The top image shows the different phases of the planet depending on where the planet is in its orbit. The phases are similar to the phases of the Moon. The bottom shows the corresponding observed flux (brightness) from the host star. There is a difference in the amount of flux received depending on where the planet is in its orbit. From Ofir (2016).

There have been quite a few exoplanet surveys to find exoplanets around stars. For example, WASP (Pollacco et al. 2006), HAT (G. Bakos et al. 2004), TrEs (Alonso et al. 2007), CoRoT (Deleuil and Fridlund 2018) are some of the surveys that have been conducted. By number, the most successful survey for exoplanets has been the Kepler space telescope.

Legacy of the Kepler Space Telescope

The Kepler space telescope was a part of NASA's Discovery Program. It continuously observed the same area of sky field in the northern constellations of Cygnus, Lyra and Draco with a field of view of 113 square degree (Borucki 2020). Kepler was designed for a precision of around 20 ppm for a 12th magnitude star in Kepler's own filter for six and a half hours observation (Gilliland et al. 2011).

The Kepler space telescope was successful for around three and a half years before, it developed a fault in two of its reaction wheels (in July 2012 and May 2013). This meant the telescope could no longer work correctly as intended because it could not point to the target area of the sky.

After trying to fix the faults (Cowen 2013), the new mission was designated as the K2[2]. This used light pressure from the sun as a reaction wheel. This meant that the telescope could not look at the same area of the sky as it had before. To stop the sun light getting into the telescope different campaigns were conducted looking at different areas of the sky near the ecliptic. Each lasted approximately 80 days before moving to the next.

Kepler was retired in 2018 after nearly all of its fuel had been used by the K2. By this point it had found that exoplanets are abundant around stars (e.g.,Fressin et al. 2013) and that they have different sizes and periods compared to the solar system (e.g., Foreman-Mackey et al. 2016). By the time it was retired it had discovered over 2,600 exoplanets.

Kepler was great for population statistics and views of multi exoplanet systems but quite a lot of the exoplanets that it found were far away (Batalha 2014). This meant that their host stars were faint so were very hard to follow-up compared to the exoplanets found from Transiting Exoplanet Survey Satellite (TESS, section 1.1.2) as they are closer.

Photometry

In order to see the change in the brightness, multiple images are needed with the same exposure time. After the exposure time, the electrical charges on the pixels are progressively read and digitized to generate a frame of data called a raw image. The raw images are then calibrated and stored in a form suitable for analysis.

Pixel binning is where the electron counts from adjacent pixels are merged to form a single value. It was introduced to reduce noise, but at the expense of reduced resolution. The most common pixel binning options are 1x1, 2x2, 3x3 and 4x4 for 1, 4, 9 and 16 adjacent pixels respectively. Pixel binning also reduces the download time compared to not doing it, giving a slightly higher sampling cadence (Romanishin 2006).

Changing the binning option also changes the image scale, which is the angular size that one pixel has with respect to the sky. It is commonly reported in arc seconds per binned pixel. It is calculated by the pixel size in micrometres, the binning number and the focal length in metres, like below:

$$Scale = \frac{pixel_{\text{size}} * binning * 10^{-6}}{(focal_{\text{length}}/206264.8062)} \tag{1.1}$$

Stars need to be sampled to centre and shape the Point Spread Function,

[2]https://keplerscience.arc.nasa.gov/publications.html

having a sampling parameter (r) used that is defined by Howell (2000):

$$r = seeing_{\text{pixel}} = Seeing/Scale \tag{1.2}$$

Where *Scale* is the arc second per pixel and *Seeing* is the Full Width Half Maximum in arc seconds. A value of r less than 1.5 is considered to be under sampled and lower values will result in increasingly larger errors (Howell 2000).

Filters

It is standard practice to use filters to restrict the measurements to photon wavelengths within a specified wavelength. For example, the Johnson Cousins photometric system has filters called U (ultraviolet), B (blue), V (visible), R (red) and I (near infra-red), which are wide overlapping filters . However, this has limitations in having some wide overlapping bandwidths so other systems such as Sloan filters (SDSS) are also employed. Figure 1.2 shows examples of the different types of filters over their respected wavelengths.

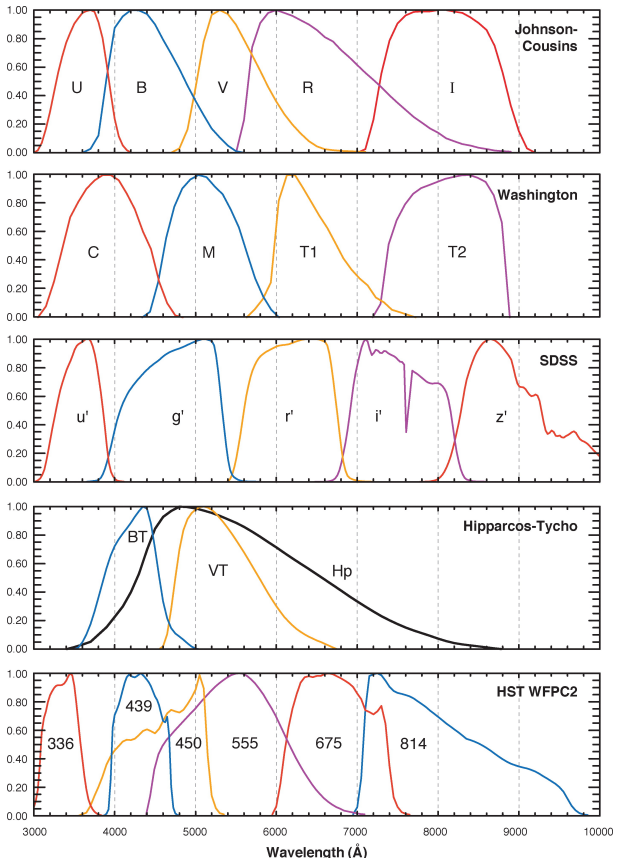

Figure 1.2: The wavelengths that different filters use and their corresponding efficiencies over the wavelengths from Bessell (2005)

Some filters are chosen to isolate specific spectral line features like H_α. Most cameras can only use one filter at any one time to observe a target. The earth's atmosphere reduces the light. The greater the distance that the light travels through the atmosphere represented by a term called "air mass", the greater the effect. The air mass can be approximated by;

$$Airmass = \frac{1}{cos(z)} \tag{1.3}$$

Where z = 90 - h and h is the altitude of the object. At high values of air mass, there can be significantly more reduction in blue light when compared to red light. The light from a predominantly red star will have significantly less effect at high air mass compared to that with a predominantly blue star.

1.1.1 Exoplanet Transits

The depth of the transit gives to the first order the ratio of the radii of the planet and star:

$$Depth = \left(\frac{R_\mathrm{p}}{R_*}\right)^2 \tag{1.4}$$

Where R_p radius of the planet and R_* is the radius of the star. The impact parameter, b varies from zero at the centre of stellar disk with one being on the cusp of the disc. The relation between the impact parameter, the orbital inclination angle i of the planetary system to the plane of the sky from Earth's point of view (Todorov 2008) and the semi-major axis a, is given according to the following expression;

$$b = \frac{a\cos i}{R_*} \tag{1.5}$$

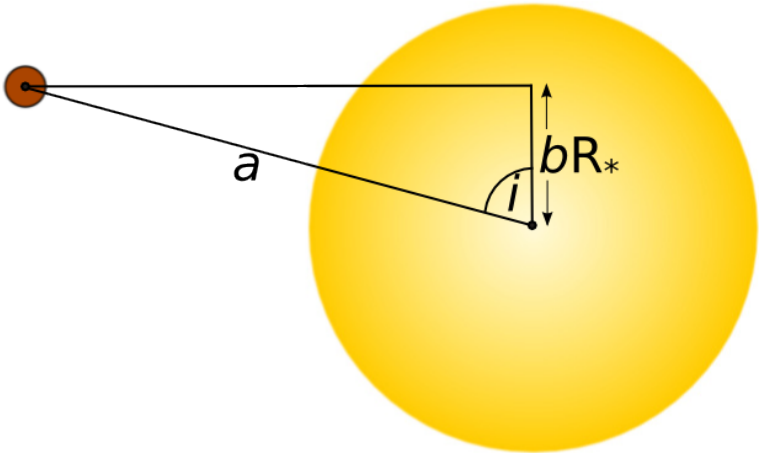

Figure 1.3: Figure from Wilson (2015) showing an exoplanet and its corresponding impact parameter.

The transit duration is given by:

$$T_{\text{dur}} = \frac{2\sqrt{(R_* + R_{\text{p}})^2 - (bR_*)^2}}{v_{\text{p}}} \tag{1.6}$$

where v_{p} is the velocity of the planet. Transit Time Variations (TTV) are variations in the transit time caused by other exoplanets in the system, which speed up or slow down the speed of the known transiting exoplanet causing variations in the orbital period of the exoplanet.

The period must be well known so that the predicted transit time has a small uncertainty in order to determine the transit variations. For an unknown exoplanet the expected TTV is in the order of a few minutes and for exomoons (extrasolar moons) TTV are expected to be in the order of seconds (Kipping 2009) but do depend on the mass and semi-major axis of the objects.

In order to calculate when exactly a transit starts and ends, a timing system needs to be used that is constant over time. UTC has leap seconds added to it so is not constant with time. Julian date is the number of days since 12:00 UT on 1st of January 4713 BC.

Due to the time needing to be constant, Barycentric Julian Date (BJD) is used, which corrects for the difference in the Earth's position with respect to the centre of mass of the Solar System. (BJD_{TDB}) is the Barycentric Julian Date in the Barycentric Dynamical Time which accounts for relativistic effects (Eastman, Siverd, and B.Gaudi 2010).

Reference Stars

Differential photometry is the simplest type of photometry, where both the target and reference stars are in the same image so they have the same filters and atmospheric disruption. Reference stars are stars that are known not to be variable or at least are not highly variable over periods of hours.

To calculate the magnitude difference between the target and reference stars, the background sky count is removed from each total count. Then divide by each other before taking the log_{10} of it and multiplying it by -2.5.

$$\Delta\text{Mag} = -2.5 log_{10}\left(\frac{Target - sky}{Reference - sky}\right) \tag{1.7}$$

As both the target and reference star have their own absolute errors, the overall error needs to be calculated by squaring them and adding them together before taking the square root.

$$\sigma_{\text{all}} = \sqrt{\sigma^2_{\text{Target}} + \sigma^2_{\text{Reference}}} \tag{1.8}$$

If N reference star are used then the reference component becomes:

$$\sigma_{\text{Reference}} = \frac{\sqrt{\sigma^2_{\text{REF1}} + \sigma^2_{\text{REF2}} + \ldots + \sigma^2_{\text{REFN}}}}{N} \tag{1.9}$$

Let $\sigma_{\text{Ref1}} = \sigma_{\text{Ref2}} = \sigma_{\text{REFN}}$, 1.9 becomes

$$\sigma_{\text{Reference}} = \frac{\sigma_{\text{REFN}}}{\sqrt{N}} \tag{1.10}$$

This means that the more reference stars, the lower the Standard Deviation (SD), provided that the SD for the extra reference are not larger than the other reference stars. But also that there are other check stars to determine that the reference stars are not too variable.

There are two main ways that photometric errors are presented either in milli-magnitude (mmag) or parts per thousand (ppt);

$$n\ mmag = 1000 * (2.5 \log_{10} \left[1 + \frac{m\ ppt}{1000}\right]) \tag{1.11}$$

Where m and n are algebraic terms. 1 ppt = 1.0852 mmag, so for small transit depths they are similar. Due to Transiting Exoplanet Survey Satellite (TESS) mission and Astroimagej software using ppt and previous work on the website was done in mmag as this is the unit predominately used by telescope control software and astronomers at large. The units in this dissertation are switched between ppt and mmag over different sections depending on the context.

Limb darkening

Limb darkening is an optical effect seen in stars, where the centre part of the disk appears brighter than the edge or limb of the star. When the exoplanet crosses the star it blocks out the light that is behind it from the observer's perspective. The limb darkening changes the brightness of the star behind the exoplanet as it crosses the star. This inputs a effect that can extend the depth of a perceived transit so it has to be corrected.

The limb darkening effect is largest at short wavelengths where a highly rounded light curve is observed. For longer wavelengths the effect is less severe and the centre of the transit takes on a flatter shape.

There are many different limb darkening correction (Claret and Bloemen 2011). However, the quadratic equation one is the most used:

$$I(\mu) = I_0[1 - c_1(1 - \mu) - c_2(1 - \mu)^2] \tag{1.12}$$

Where $\mu = \sqrt{1 - x^2}$, and x is between one and zero. μ of zero refers to the edge of the star and a μ of one refers to the centre of the star. I_0 is a normalization constant, the specific intensity at the centre of the star's disk.

The variables c_1 and c_2 can be set on theoretical models of the system or empirical models. However, when theoretical predictions are based on the type of star the planet goes around and the filter that is being used, they do not allow us to reach accuracy in the planetary radius of better than 1-10% (Csizmadia et al. 2013).

1.1.2 TESS

TESS (Transiting Exoplanet Survey Satellite) will survey most of the entire sky over the course of two years by breaking it up into 26 different sectors, each is 24 degrees by 96 degrees across (Ricker et al. 2014). The cameras on the spacecraft will stare at each sector for at least 27 days, looking at the brightest stars at a two minute cadence and full images at 30 minutes. Figure 1.4 shows the different sectors that the TESS will observe over the first two years.

The stars TESS will study are 30 to 100 times brighter than those the Kepler mission and K2 follow-up surveyed, which will enable far easier follow-up observations with both ground-based and space-based telescopes. TESS will also cover a sky area 400 times larger than that monitored by Kepler.

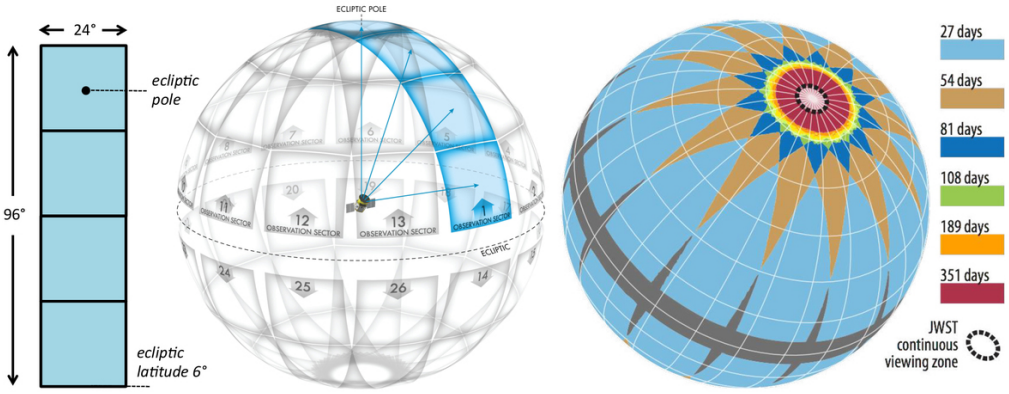

Figure 1.4: Left: combined field of view of the four TESS cameras in degrees. Middle: the celestial sphere subdivided into the 26 observation sectors. Right: the total duration of observations on the celestial sphere, taking into account the overlap between sectors for the first two years of TESS. From Ricker et al. (2014).

In addition to its search for exoplanets, TESS will allow scientists from the wider community to request targets for astrophysics research on approximately 20,000 additional objects during the mission through its Guest Investigator program.

The TESS mission has overlapping sectors at the poles which means an area around the poles will be observed for nearly a year over the 2 year program. The area around the north pole is apart of the continuous viewing zone for the James Webb Space Telescope (JWST) (Jansen and Windhorst 2018). This means that longer period exoplanets found by TESS can be followed up by JWST and might have their atmospheres characterised (Louie et al. 2018).

TESS Follow-up Observing Program

The primary goal of the TESS Follow-up Observing Program (TFOP) working group is to provide follow-up observations that will facilitate the achievement of the Level One Science requirement, which is to measure the masses for 50 transiting planets smaller than 4 Earth radii.

The secondary goal of the TFOP working group is to foster communication and coordination both within the TESS Science Team and with the community at large in order to minimize wasteful duplication of observations and analysis.

Before TESS was built it was expected to find around 1700 exoplanets in the first 2 years including 556 that are smaller than 2 $R_{\oplus}$ (Sullivan et al. 2015). After TESS was built that was revised to around 1250 exoplanets from its 2-minute cadence (Barclay, Pepper, and Quintana 2018) including 250 smaller than 2 $R_{\oplus}$. An additional 3100 planets are expected to be found from the full-framed images.

The TESS Objects of Interest (TOI) will be followed up with imaging, reconnaissance spectroscopy, and precise Doppler spectroscopy. The TOI numbering system gives each star system a number starting with 101, then a decimal with corresponds to the planet candidate period e.g. 103.01 or 104.02. The number will not be reused so if a system is a false positive then it will have the same number.

False positives are where an exoplanet transit signal turns out not to be an exoplanet but something else like a Nearby Eclipsing Binary (NEB) for example. Exoplanet Follow-up Observing Program (ExoFOP) is a 'sandbox' for the community to share information and data. It was originally used for the Kepler follow-up observations.

There are two main pipelines for TOIs: the Quick Look Pipeline (QLP) and the Science Processing Operations Center (SPOC). The QLP only uses the 30 minute full images whereas SPOC uses both the two minute cadence images and the full images.

The TFOP Working Group is run by Dave Latham and is separated into 5 Sub Groups (SG):

SG1 is seeing-limited photometry which is used to identify false positives and check for chromaticity in different filters if transit is found.

SG2 is recon spectroscopy which is used to help identify stars that are unsuitable for radial velocity.

SG3 is high-resolution imaging to detect nearby objects that are not resolved in the TESS catalogue.

SG4 is precise radial velocity which helps to derive the orbit for the planet and the planetary mass relative to the host star.

SG5 is Space-based photometry used to confirm and/or improve the period for small transits depths that cannot be seen with ground based telescopes.

There are lots of different dispositions that the TFOP Working Group can be given, all starting blank then changing when significant evidence is found to support the decision. The most common types are planet candidate, known planet and false positive.

TESS is only 2 more sectors away from completing its first 2 year mission. It has found 2,044 candidates exoplanets of which 177 are 2 $R_{\oplus}$ or less. Only 55 of them have been confirmed exoplanets[3]. However, 484 of the candidates have been found to be false positive and 253 are already known exoplanets.

1.1.3 Website

A website (The Transit Follow Up Tool[4]) was created to calculate the transit times of the selected exoplanets. Other websites exist that can calculate the transit times like the Exoplanet Transit Database (Poddaný, Brát, and Pejcha 2010) and Swarthmore Transit Finder (Jensen 2013) but having the transit times calculated inside the website means that this information can be used to calculate other things like the air mass of the observations.

The website also lays out the method for calculating the information from the telescope setup so that it can predict the uncertainty for a target. This method is the same as the one outlined in section 3, (Method) but with the addition of images and videos to help guide a person through.

The website has 4 different data sources that can be used to find transits. They come from the Exoplanet Transit Database, NASA Exoplanet Archive, Exoplanet Orbit Database and the ExoFOP TOIs. Exoplanet Orbit Database was the first data source for the website but is not being updated with new sources (Han et al. 2014).

[3]https://exoplanets.nasa.gov/tess/

[4]https://observatory.herts.ac.uk/exotransitpredict/

There are small differences between the exoplanet information that is given by Exoplanet Transit Database and NASA Exoplanet Archive. This is mainly due to missing/ not entered information from one being entered in. The ExoFOP TOIs are the alerts from the TESS team. The website outputs more information for the TESS than the confirmed exoplanets and can be sorted based on the priority that the TESS team has given to the star.

The website can produce a timeline plot showing the transits over the night with respect to the hours after sunset. Figure 1.5 shows an example of this plot. It can be used to work out quickly if more than one transit is possible to observe for a given night. For this example HAT-P-9 b and WD 1145+017 b could be observed on the same night without affecting each other.

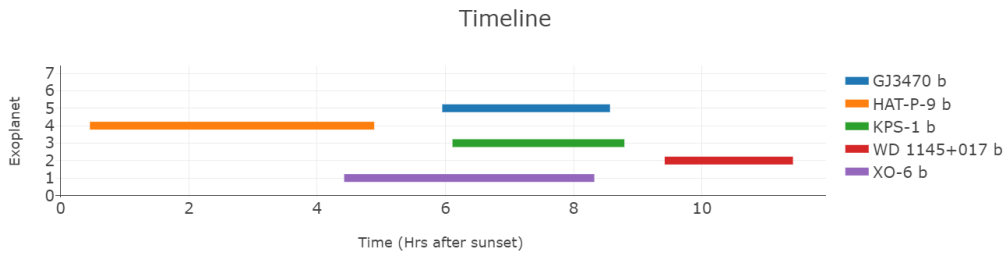

Figure 1.5: An example of the timeline plot from the Transit Follow Up Tool website.

Inside the website, there is a page that is able to predict the weather using data from the Dark Sky (Grossman and Turner 2019). It can produce many plots but the most important is the 48 hrs Cloud coverage, Precipitation Probability and Precipitation intensity. This helps to know when not to attempt to observe, particularly when it is predicted to be rainy or very cloudy.

Chapter 2.2 explains how the website uses the predicted precision from Chapter 2.1 to predict the expected uncertainty for a target. The chapter 10.6 (Appendices) details how the website works to predict the exoplanet transit.

1.1.4 Charged Coupled Devices

Charged Coupled Devices are the main type of cameras used for photometry. There are 3 main systematic errors that need to be corrected due to using Charge Coupled Device (CCD): readout noise (bias), dark current and flat fielding.

The readout noise is the number of electrons introduced per pixel into the final signal upon readout of device, by two parts:
Conversion from analogue to a digital number
The electronics themselves will add random fluctuations in the output.

The dark current comes from the CCD being above absolute zero, so it is subjected to thermal noise. When it is high enough, electrons will be freed. As the dark current is in a strong relationship to the temperature, reducing the temperature of CCD will reduce the amount of thermal noise that is created, and reduce the amount of dark current.

Flat fielding is needed as each pixel has a slightly different quantum efficiency so the response needs to be flattened out. This takes a uniform illuminated image in each filter to create an image that can be divided to help remove the variation, which also helps with dust accumulation and optical vignetting (Howell 2000).

When taking extremely short exposure times with mechanical shutters, some part of the image will be exposed for longer than other parts. There are 2 main types of mechanical shutters: iris and vane (Zissell 2000). If short exposure images are taken, then there may be a correction needed by a shutter map.

CCDs are mainly linear as there is a simple relation between charge collected by each pixel and digital number sorted in the output image. However, due to the CCDs bias there is a constant number removed. At high inputs the CCD becomes nonlinear due to it becoming more difficult to add electrons.

Calibration Images

In order to get photometry data (accurately) into the milli-magnitude range, calibration images are needed. There are 3 different types that are taken: Bias, Dark and Flat images. Multiple images of each calibration type are taken to create three master calibration images. So that each pixel in each master has the average value for that pixel location for that calibration type. By taking the average, the effects of random cosmic rays are reduced.

Bias images are taken in order to obtain the true zero level. The images are taken with an exposure time of 0 seconds so that it is only the readout signal that is collected. Dark images are taken similarly to Bias images but have an exposure time above zero but the shutter is kept closed.

Flat images are taken in order to reduce the flat fielding problem. These images are taken with the shutter open unlike the bias and the dark. There are typically 3 main approaches to flats: sky, twilight and dome flats. They all have their own advantages and disadvantages.

Dome flats use artificial light to produce a 'uniform' light in order to flatten out the different quantum efficiencies. One of the advantages is that they do not have to be taken during the observing nights but can be taken in the afternoon before and after the observations. One of the main disadvantages is that the light used is never really as uniform over the spectrum as sky flats are.

Sky and twilight flats are more similar than dome flats as they use the sky rather than artificial light. The main difference between sky and twilight is that twilight flats are taken during twilight whereas sky flats are taken at astronomical night time. During the twilight flats the sky is brighter so they do not have to be exposed for as long so it is easier to take more.

As the sky brightness changes very quickly during twilight, the timing of the flats and the exposure time have to be taken carefully so that the flats are not over-exposed and go past the nonlinear point. That is especially true when taking multiple different filter sets as the sky's brightness changes differently over different filters.

1.1.5 Telescope Sites

There were three main telescope networks that were used for this work: Bayfordbury, Thai Telescopes and the Pirate Telescope (Open University). However, as they are run separately from each other, they each have their own way of operating that is different to each other. Chapter 10.2 (Appendices) details more information about the telescopes and sites.

Bayfordbury site

Bayfordbury is the University of Hertfordshire's Observatory site. It has three working telescopes and is situated less than 20 miles from the centre of London with its light pollution. The Chris Kitchen Telescope (CKT) and Jim Hough Telescope (JHT) both have the same camera type (SBIG STL-6303E) while the Robert Priddey Telescope (RPT) has a different camera (Moravian Instruments G4-9000). All the telescopes have the same base of Meade LX200 series which means that they have the same aperture and focal length.

Bayfordbury uses Real Time Markup Language (RTML) plans to control the telescopes, whereas the Thai Robotic Telescope (TRT) & Pirate use different web-based online tools to create the plans that control the telescopes.

For the Bayfordbury site, each telescope has a master set of 1x1, 2x2, 3x3 and 4x4 pixel binning calibration frames that are produced at the CCD operating temperature of -20°C. The appropriate master frames are selected automatically when calibrating the images. The dark images are taken at set exposure times. This means that only the selected exposure times can be used as the automated calibration system used at Bayfordbury could not deal with different exposure times.

As Bayfordbury deals directly with the calibration files itself, only the calibrated images can be downloaded individually, or the folder that contains all the images for that plan can be opened. The calibration masters are stored on the computer server, with the individual calibration stored on the computer that controls that telescope. They are not as easy to access as the calibrated images.

Due to England's weather, dome flats are used as it may be rainy or too cloudy to take twilight flats, but clear up for a few hours during the night when images can be taken. The calibration masters are redone every couple of months, due to the amount of time that it takes to do all the calibration options. There are four binning options each of which has 5 filters and that is just for one telescope out of the three. Bayfordbury uses 20 individual calibration images to make a master.

Thai Telescopes

The Thai National Telescope (TNT) is a 2.4 metre telescope, which is located in Chiang Mai Province, Thailand. The main CCD camera for the TNT has a specific built camera called 'ULTRASPEC'. The TRT Network has three different sites around the world, one in Australia, one in China and the other in the USA. They are all the same type of telescope (0.7m CDK700) but with different cameras attached to them.

One of the problems with the TRT, is that if a plan is created after the start of the night, the calibration files will not be created after the images start. So sometimes one or more of the calibration files will be missing, meaning the data cannot be used or different calibration files from different days have to be used.

The TRT website does not create the final calibration images and there is no way of directly downloading all the images at once within the website. The individual files must be downloaded individually as well as the individual calibration images.

Open University site

The Open University has two telescopes, Physics Innovations Robotic Telescope Explorer (PIRATE) and COmpletely Autonomous Service Telescope (COAST) on the island of Tenerife. This research will focus on PIRATE as it is the main telescope that has been used to look at exoplanet transits. The PIRATE has a focal length of 2.94m.

The telescopes take the calibration images each night before and after observations are taken so the changes in the CCD are managed. They use twilight flats as good weather is expected most nights. As the timing for twilight flats is small only 5 flat calibration images are created for each filter.

The Open University telescope website uses a folder system which splits up the calibration images and the observation images. The individual observation images must be downloaded individually, then the individual calibration images that go with that observation.

1.2 Study Aims

The primary study aims are to:-

1. Use the TRT network and Bayfordbury to help verify TOIs to see if they are real transit events or false positives.
2. Use the TRT network, Bayfordbury and PIRATE to get transits on confirmed exoplanets to look for TTV.

P. J. Beck (2018) showed that the predicted uncertainty is close to the achieved precision, but that was only considering both the target and a reference star. So by using multiple reference stars the predicted uncertainty may get closer to the achieved precision.

The PIRATE archive has a large data set of images in 1x1 and 2x2 binning. The data can be used to calculate what effects the changes in the binning has on the predicted uncertainty over different magnitudes and exposure times.

The secondary study aims are to:-

1. Compare the predicted precision for each setup to the Root Mean Square (RMS) of the transit fit.
2. Calibrate the PIRATE telescope over different binning options and filters, then compare the effect the different binning options have on the predicted uncertainty.

2 Technical Background

This chapter deals with the technical information that is needed in order to understand the other chapters. The predicted precision describes the equations that were used to predict the uncertainty for the different systems. The Website section then details how the predicted precision was used by the website.

The main tool used for the analysis of the transits was AstroImageJ. It can perform the photometry and produce transit light curve plots. It was also used for the calibration and analysis that was needed for the predicted precision.

Analogue-to-digital units (ADU) are the units that data in the images are in but the equations use electrons, so they have to be converted into electrons by using the gain (e/ADU) which is electrons per ADU.

2.1 Predicted precision

The predicted precision is based on work by Southworth et al. (2009) and P. J. Beck (2018). It uses knowledge about the system setup in order to predict what the expected uncertainty for the target is going to be.

It takes into account errors from the bias calibration images as well as the dark and flat calibrations, while also taking into account the scintillation from the telescope, the sky brightness and the error in the target counts. The predicted precision on the target alone in electrons is represented by the following equation from P. J. Beck (2018);

$$J = \sigma^2_{\text{bias}} + \sigma^2_{\text{dark}} + (\sigma_{\text{flat}})^2_{\text{target}} + (I_{\text{RMS}})^2_{\text{target}} + \sigma^2_{\text{sky}} + \sigma^2_{\text{target}} \quad (2.1)$$

$$(\sigma_{\text{total}})_{\text{target}} = \sqrt{J} \quad (2.2)$$

Where σ_{bias}, σ_{dark} and σ_{flat} are the bias noise, dark current noise and the flat field noise respectively. The values are obtained from an analysis of the corresponding calibration images.
I_{RMS} is the scintillation noise due to air turbulence and the telescope size as defined by equations (2.8) and (2.9).
σ_{sky} is the sky noise at that specific observation location and is defined by equation (2.10).
σ_{target} is the target noise and is defined by equation (2.12). All of these terms relate to integration of the target over an aperture.

$$(\sigma_{\text{total}})_{\text{target in magnitude}} = 2.5 \log_{10}[1 + \frac{(\sigma_{\text{total}})_{\text{target}}}{N_{\text{target}}}] \tag{2.3}$$

$(\sigma_{\text{total}})_{\text{target}}$ is then divided by a prediction of the total counts from the target (N_{target}) in electrons to give the relative error. Or, this is inputted into the equation above to get the error in magnitudes.

The bias and dark noise values for a particular camera are established from the calibration images. The values are calculated by the SD from each pixel location over a stack of calibration images. Then taking the average of the pixel location values for the bias and dark noise values.

As the dark current noise is linked to the exposure time, it needs to be worked out for any exposure time. So $\dot{\sigma}_{\text{dark}}$ is calculated. This is the value of the gradient of a plot of different exposure times versus the dark current noise squared, where t_{exp} is the user selected exposure time. Then the dark current noise for a selected exposure time can be calculated by:

$$\sigma^2_{\text{dark}} = \dot{\sigma}_{\text{dark}} * t_{\text{exp}} \tag{2.4}$$

In order to predict the uncertainty for different magnitude stars, the number of counts expected from a star is predicted too. This is also important as the flat field, scintillation noise and the target error all depend on the target count (N_{target}) as well.

For the flat fields, the noise is assumed to be only affected by the number of counts from the target. So the general case for the flat field noise with any target count (N_{target}) is;

$$(\sigma_{\text{flat}})_{\text{target}} = (\sigma_{\text{flat}})_{(N_{\text{target}=1})} N_{\text{target}} \tag{2.5}$$

Where $(\sigma_{\text{flat}})_{\text{target}}$ is the flat field noise for that target. $(N_{\text{target}})_{\text{flat}}$ is the total electron count per pixel averaged over the flat images.
$(\sigma_{\text{flat}})_{(N_{\text{target}=1})}$ is the SD that a count of 1 would give. In order to find this it is back calculated by the following equation;

$$(\sigma_{\text{flat}})_{(N_{\text{target}=1})} = \sigma_{\text{flat}}/(N_{\text{target}})_{\text{flat}} \tag{2.6}$$

σ_{flat} is the reduced flat noise value. That is calculated in 2 parts as it contains the bias and dark errors inside it. First σ_{cal}, is calculated by taking the average of the SD for each pixel location over the flat stack. Then this is recalculated to remove the bias and dark noise from the calculated value by;

$$\sigma_{\text{flat}} = \sqrt{\sigma^2_{\text{cal}} - \sigma^2_{\text{bias}} - \sigma^2_{\text{dark}}} \tag{2.7}$$

This is then divided by the average counts over the flats. This may be smaller on a target as it is integrated over an aperture rather than the whole image especially when their is a very steep drop off around the edge of the CCD. But this can be corrected by using just the middle bit of the image.

The scintillation error with a small telescope and a bright target has been shown to be the dominant source of error. So it is important to maximize the exposure time, since the longer exposure time, the lower the noise due to scintillation (Dravins et al. 1998). The normalized scintillation noise is given by;

$$\sigma_{\text{scint}} = \frac{0.09}{100^{(2/3)}} D^{(-2/3)} X^{(7/4)} e^{(-h/H)} (2t_{\text{exp}})^{-0.5} \tag{2.8}$$

Where D is the telescope aperture in metres, X is the air mass, h is the altitude of the telescope in metres. H is equal to 8000 metres which is the scale height of the atmosphere.

$(I_{RMS})_{\text{target}}$ is the scintillation noise from the air turbulence for the target. It is obtained by scaling σ_{scint} by the total electron count for the target (N_{target});

$$(I_{\text{RMS}})_{\text{target}} = N_{\text{target}} \sigma_{\text{scint}} \tag{2.9}$$

The sky noise (σ_{sky}) is established from values that are obtained from an analysis of areas of the sky, in lots of images in the absence of a target. This can give what the 'typical' sky condition is going to be, based on the images that are analysed. Where σ'_{sky} is the total noise from a region of the sky (image) that has no stars in it.

$$\sigma_{\text{sky}} = \sqrt{\sigma'^2_{\text{sky}} - \sigma^2_{\text{cal}} - (I_{\text{RMS}})^2_{\text{sky}}} \tag{2.10}$$

Where $(I_{\text{RMS}})^2_{\text{sky}} = (N_{\text{sky,t=1}} t_{\text{exp}} \sigma_{\text{scint}})^2$ and that $N_{\text{sky,t=1}}$ which is the expected electron count from the sky background for a 1 second exposure time. Also $\sigma^2_{\text{cal}} = \sigma^2_{\text{bias}} + \sigma^2_{\text{dark}} + \sigma^2_{\text{flat(sky)}}$ and $\sigma_{\text{flat(sky)}}$ is $(\sigma_{\text{flat}})_{(N_{\text{target=1}})} N_{\text{sky}}$. Which results in:

$$\sigma_{\text{sky}} = \sqrt{\sigma'^2_{\text{sky}} - \sigma^2_{\text{bias}} - \sigma^2_{\text{dark}} - \sigma^2_{\text{flat(sky)}} - (N_{\text{sky,t=1}} t_{\text{exp}} \sigma_{\text{scint}})^2} \tag{2.11}$$

For the target counts, the standard assumption is made that the target signal follows Poisson noise characteristics. As the counts are at a constant rate with a probability of independence of time since the last event, so the target noise is given by:

$$\sigma_{\text{target}} = \sqrt{N_{\text{target}}} \tag{2.12}$$

Predicting Target Counts

The derivation of the predicted value of N_{target} is the most important part for predicting the precision. N_{target} is predicted by using a number of equations, after working out the constants for the equipment. Only the catalogue magnitude of the target star, exposure time and the air mass are needed to predict the target counts.

The key relationship is between the catalogue magnitude and instrument magnitude, for an air mass of 1.0 and an exposure time of 1 second, which is obtained from a series of observations. This has to be worked out for each particular telescope/ camera combination.

Many observations are needed, that cover a wide range of target magnitudes, exposure times, values of air mass and observing conditions. The only prerequisite in the choice is that there are no clear problems with the images. Also that the star was not past the linearity limit for the CCD.

$$[m'_{\text{t=1s,X=1.0}}]_{\text{predicted}} = Gradient * m_{\text{target}} + Bias \tag{2.13}$$

Where *Gradient* and *Bias* come from the trendline of the Catalogue Magnitude (m_{target}) Versus Instrument Magnitude ($[m'_{\text{t=1s,X=1.0}}]_{\text{measured}}$) plot, where m_{target} is the catalogue magnitude of the target. The predicted instrument magnitude for the target with an exposure time of 1 second and an air mass of one is $[m'_{\text{t=1s,X=1.0,target}}]_{\text{predicted}}$. The air mass term is then added;

$$[m'_{\text{t=1s,X=X}}]_{\text{predicted}} = [m'_{\text{t=1s,X=1.0}}]_{\text{predicted}} - \varepsilon(1.0 - X) \tag{2.14}$$

$[m'_{\text{t=1s,X=X}}]_{\text{predicted}}$is the predicted instrument magnitude for the target with an exposure time of 1.0s and where air mass is the observed air mass. Where ε is the air mass extinction coefficient in magnitudes per unit airmass which can be based on theoretical values or measured values.

$$[(N_{\text{target}})_{(\text{t}=t_{\text{exp}}\ \text{X=X})}]_{\text{predicted}} = t_{\text{exp}} 10^{-\frac{1}{2.5}\left[m'_{(\text{t=1s,X=X})}\right]_{\text{predicted}}} \tag{2.15}$$

Where $[(N_{\text{target}})_{(\text{t}=t_{\text{exp}}\ \text{X=X})}]_{\text{predicted}}$ is the predicted electron total count for the target with an exposure time of t_{exp} and air mass of X. The trendline (eq.2.13) gives the equation that can then be used to predict the value of instrument magnitude for the target for t=1.0s and X=1.0 based solely on the target's catalogue magnitude.

Having derived the best fit line (eq.2.13), the formulation can then be verified by using the catalogue magnitude to back calculate a predicted value for the instrument magnitude for each target and then subtract it from the measured instrument magnitude to give ($\Delta m'$). The average and SD of the values of $\Delta m'$ gave an estimate of the intrinsic error in the fit. P. J. Beck (2018) found results of 0.45 mmag and 195 mmag respectively for the CKT.

P. J. Beck (2018) showed 211 completely independent observations from what was used to produce the instrument to catalogue magnitude plot. It validated that the predicted instrument magnitude would on average have a very small (0.068 mag) difference between the measured instrument magnitudes, but that the SD was around 0.15-0.2 magnitudes. The images covered a wide range of catalogue magnitudes, exposure times and air masses and observing conditions.

The validation process produced figure 2.1, where a matching set of predicted instrument magnitudes (in green) and measured instrument magnitudes (in red) were produced from the completely independent observations. The inspection of figure 2.1 shows that a good match was achieved over a range of catalogue magnitudes, exposure times and air masses. The same catalogue magnitude but with different measured magnitudes is due to the differences in the air masses.

To produce the measured instrument of the star for an air mass of 1 and exposure time of 1 second, the following equation is used:

$$[m'_{\text{t=1s,X=1.0}}]_{\text{measured}} = -2.5 \log_{10}[\frac{N_{\text{target}}}{t_{\text{exp}}}] + \varepsilon(1 - X) \tag{2.16}$$

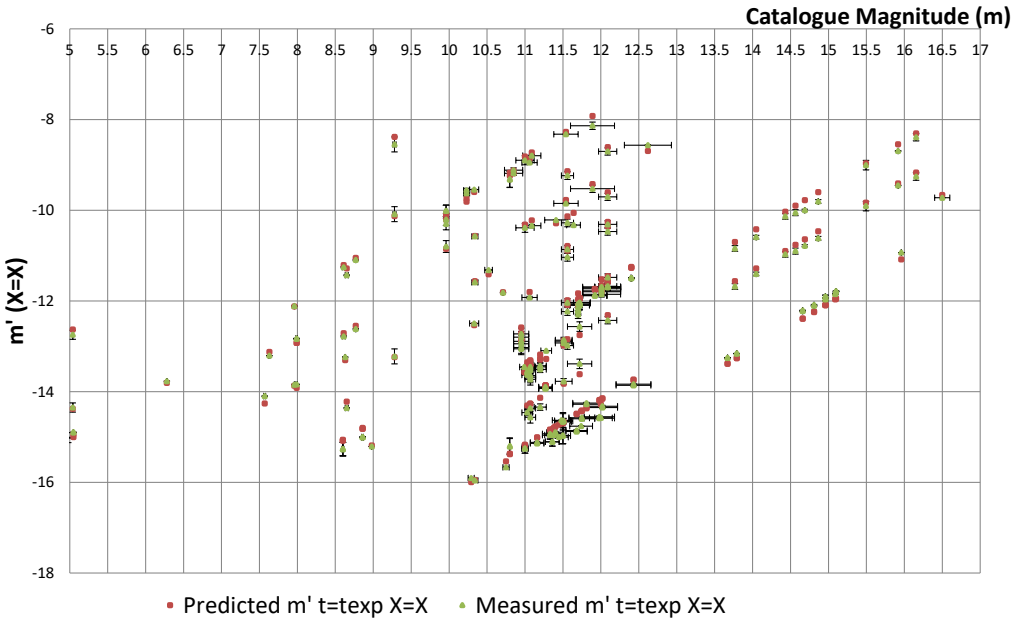

Figure 2.1: The predicted and measured instrument magnitude ($m'_{\mathrm{t}=t_{\mathrm{exp}}\ \mathrm{X}=\mathrm{X}}$) versus the catalogue magnitude (m) from P. J. Beck (2018).

P. J. Beck (2018) found that the predicted uncertainty was typically within 2 mmag (1.84 ppt) of the measured values. That was for when the target and a reference star was combined. However, when the number of reference stars increases the overall uncertainty decreases, so the less effect a particular reference star should have. The predicted uncertainty would be expected to be closer to the measured value.

2.2 Website

The formula for the Predicted Precision is not a simple calculation for a person to work out due to the number of terms involved, so it was integrated into a program to automate the calculation as a tool for planning observations (P. J Beck et al. 2019).

The website was created so that it could do the calculation. The Predicted Precision reduces down to the instrumental values: Bias, Dark, Flat, Scintillation, Sky Constant, Sky SD, ϵ, *Gradient* and *Bias*.

With only the magnitude of the target, the exposure time and the air mass during the observations needed, assuming that the focal length, pixel size, expected seeing and the linearity limit are known. The peak pixel value for that particular telescope/camera setup can be calculated. This part only needs to be done once.

Table 2.1: Units for the Predicted precision inputs for the website.

Type	Units	Symbol from Predicted precision
Bias	electron	σ_{bias}
Dark	electrons/s	$\dot{\sigma}_{\text{dark}}$
Flat	Unit less	$(\sigma_{\text{flat}})_{(N_{\text{target}=1})}$
Sky	electrons/s	$N_{\text{sky,t=1}}$
Sky SD	electrons/s	σ'_{sky}

Table 2.1 shows the units of the values that the website takes for the predicted precision. The flat value is unit-less which is unlike the rest.

Peak pixel value

The Peak pixel value is important to know so that the saturation of the CCD is not reached based purely on the object that is being observed.

$$peakval = \frac{objcount}{2\pi(seeing_{\text{px}}0.51)^2} + bgcount \tag{2.17}$$

Where *objcount* comes from equation 2.15 and $seeing_{\text{px}}$ from equation 1.2.

$$bgcount = t_{\text{exp}}N_{\text{Sky}} \tag{2.18}$$

Where N_{Sky} is the sky background count per second. The user selects the exposure time and enters the magnitude of the star in the filter and the website will output the peak pixel value. This helps select the exposure time so that the saturation of the CCD is not reached.

2.2.1 Website Plots

The website has a graphs tool, which uses PLOTLY JAVASCRIPT. The graphs tool is used to produce the plots on the website. There are many different plots that can be produced, from the weather, to a timeline, to the predicted precision.

One of the plots that can be created from the website shows the breakdown of the different errors types, which are used to create the predicted precision. Figure 2.2 shows the breakdown of the errors for the CKT for a 60 second exposure time. Inspection of this plot shows that stars brighter than 11.25 are dominated by flat fielding errors, so if more flats were taken maybe this would lower the overall uncertainty.

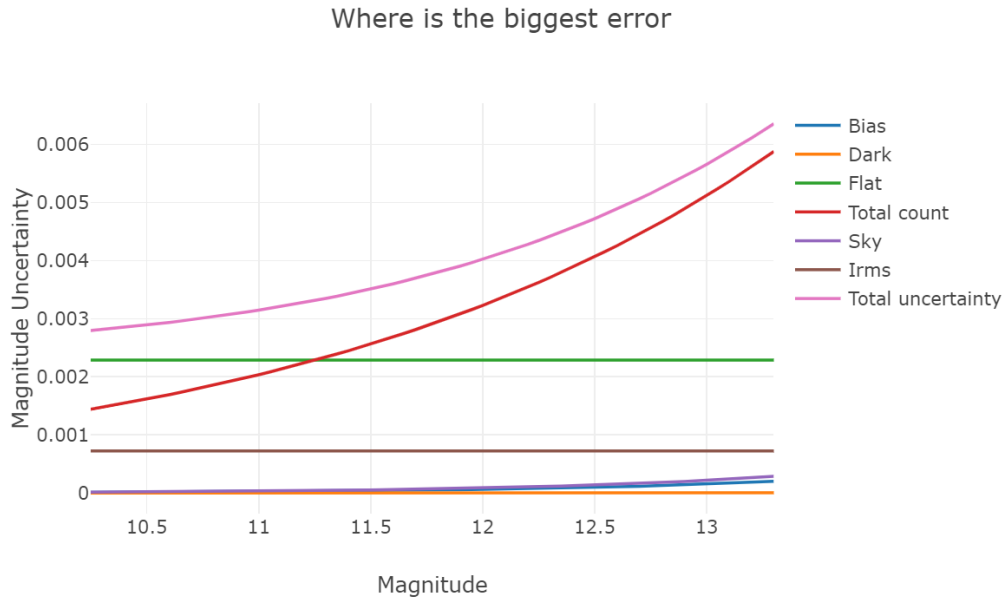

Figure 2.2: An example of the breakdown plot from the website. It shows the errors from the CKT for an image with an exposure of 60 seconds and an air mass of 1. The magnitude range is based on what the seeing and the linearity limit estimate to be valid. In the key, 'total counts' is target error.

The website can also create a predicted plot based on the transit details and predicted precision. The trapezoidal transit model is used as the basis for the plot so that only the transit time and depth is needed. An assumption that it uses is that the first contact to second contact and the third contact to fourth contact are a quarter each of the total transit time. So the second contact to the third contact is half the transit time.

The assumption about the transit time and form being trapezoidal transit model was made so that only the transit time and depth would be needed. This meant that TOIs could also be predicted as only the depth and duration of the event was released and not the inclination or the impact parameter, which meant other models could not be used.

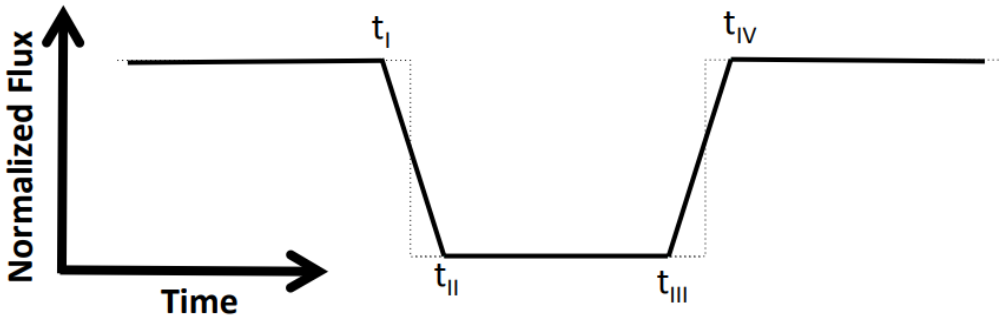

Figure 2.3: Plot showing the trapezoidal transit model and the four contact positions (t_{I}-t_{IV}) from Agol (2012).

Figure 2.3 shows the positions of 4 contact points. It uses the exposure time and time separation between the images to work out the number of images before during and after the transit.

Then using the predicted precision, a random number between 0.035 and 0.965 is input into a normal distribution function which turns the number into a SD between about -2.5 and 2.5. This is then multiplied by the predicted precision and then added to the value of the trapezoidal model for that time. The predicted precision used is then the uncertainty in the value.

This only takes into account the target's uncertainty as the reference star's magnitude may not be known. So the model assumes there are 5 good references of the same standard as the main target. This works out as $\sigma_{Target}\sqrt{1.2}$ which is about 1.095 times the predicted uncertainty of the main target. This value was obtained by comparing the overall error predicted with the reference stars and seeing which number of references predicted the overall error based only on the target's predicted error.

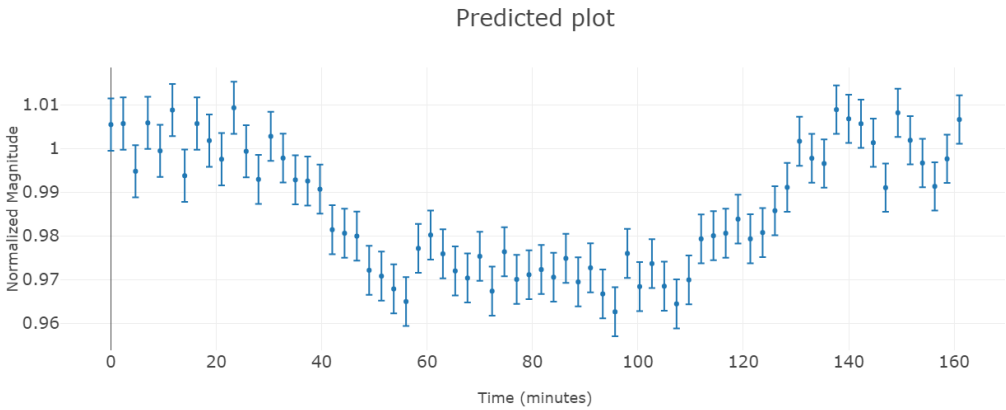

Figure 2.4: Example of the predicted plot for WASP-52 b with the CKT for a 90 second exposure time.

Due to the random numbers used each time, the plots cannot be recreated unless the data is saved. The transit depth, transit duration, magnitude of star all vary with different exposure times. This can be used to assist which transit to select and the exposure time. Figure 2.4 shows an example from the website.

The main aim of the predicted plot is to show the differences between exposure times and the number of images that will be collected and what effect each has. As the exposure time increases the uncertainty decreases but fewer images are collected.

2.3 AstroImageJ

AstroImageJ (AIJ) is an astronomical image processing, interactive time-series multi-aperture differential photometry with detrending parameters and exoplanet model fitting. It is the preferred software package for TESS WG SG1. AIJ does not currently provide estimates of the parameter uncertainties from the model that it fits.

2.3.1 AstroimageJ Uncertainty

AIJ calculates the photometric error by first calculating N for each aperture/star (Collins et al. 2017).

$$N = \frac{\sqrt{GF_* + n_{\text{pix}}(1 + \frac{n_{\text{pix}}}{n_{\text{b}}})(GF_{\text{S}} + F_{\text{D}} + F_{\text{R}}^2 + G^2\sigma_{\text{f}}^2)}}{G} \tag{2.19}$$

Where G is the gain of the CCD (electrons/ADU)
F_* is the net counts on the targets in ADU
n_{pix} is the number of pixels in the aperture
n_{b} is the number of pixels in the region used to estimate sky background
F_{S} is the number of sky background counts per pixel in ADU
F_{D} is the total dark counts per pixel in electrons
F_{R} is read noise in electrons/pixel/read
σ_{f} is the SD of the fractional count lost to digitization in a single pixel

Then all the comparison stars noises are combined into a total comparison noise by:

$$N_{\text{E}} = \sqrt{\sum_{i=1}^{n} N_{C_i}^2} \tag{2.20}$$

Where i indexes the comparison stars.
N_{C_i} is the noise for each comparison star as calculated by equation 2.19.

$$\sigma_{\text{rel-flux}} = \frac{F_{\text{T}}}{F_{\text{E}}}\sqrt{\frac{N_{\text{T}}^2}{F_{\text{T}}^2} + \frac{N_{\text{E}}^2}{F_{\text{E}}^2}} \tag{2.21}$$

Where F_{T} is the net counts of the target
F_{E} is the sum of the net counts in the ensemble of comparison star apertures
N_{T} is the noise in the target star aperture from equation 2.19
N_{E} is the ensemble noise from equation 2.20.

AIJ estimates the uncertainty in each measurement based only on the factors included in equation 2.19.

This means that additional sources of photometric uncertainty are not accounted for by AIJ. They include atmospheric scintillation, variable leakage of flux from neighbouring stars into the aperture as seeing changes slightly from exposure to exposure. As well as the poisson noise in the master dark and master flat images, slight variations in CCD bias in the time-series and inaccurate determination of sky-background from exposure-to-exposure.

This means that there will be a difference between the predicted errors from equation 2.3 and the outputted AIJ errors especially when atmospheric scintillation, poisson noise in the flat images are the dominant or have a significant effect.

2.3.2 AstroImageJ Plots

AIJ has a plotting tool for the data that is analysed. It is a complex tool as it is able to analyse exoplanet transits, variable stars and light curve from Asteroids.

The light curve from the main target can be plotted. Other data than the main target can also be plotted, which shows what the conditions are like over the observation. They appear only at the bottom quarter of the plot. They are the following;

The Sky count per Pixel shows the change in the background sky that can be associated with systematics. The width of target is the mean of the X and Y direction of the Full Width Half Maximum (FWHM) on the target. The total counts of the reference stars and the Air mass inverted shows what the transparency was like during the observation. The X and Y position of the centre of the aperture of the main target shows the image shift during the observation.

In order to produce a light curve fit, the predicted ingress and egress times are inputted then the fit mode can be moved around if there appears to be a shift in the timings.

For ExoFOP TESS the target are plotted 3 times over with a shift in the y-axis. The 3 plots are the target not detrended then detrended with air mass and finally, the model fit. Then 5 to 6 reference stars are plotted on the same plot with shifts in the y-axis applied. If there are a lot of reference stars then they can be plotted on a separate plot to the target.

AIJ uses all the stars that are labelled "C_X" where X is the number of that star in the selection, where the target star and removed reference stars are "T_X". As stars can change from a reference star to a target/ check star and vice versa, the X is a constant for that star.

As the number of reference stars increases the better the light curve plot is produced, Figure 2.5 shows this. Due to the random noise between each reference star the light curve produced gets slowly smoothed out by the other reference stars. This happens up to the point where either the target SD becomes dominant or if an added reference star is too noisy and adds too much noise so the SD goes up.

AstroimageJ reports the RMS rather than the SD. The RMS is proportional to the SD through R, where R is the correlation between the X (Time) variable and Y (magnitude/ relative flux) variable. The R for exoplanets should be close to zero so the SD and RMS should be approximately the same.

$$RMS = \sqrt{1 - R^2} SD \tag{2.22}$$

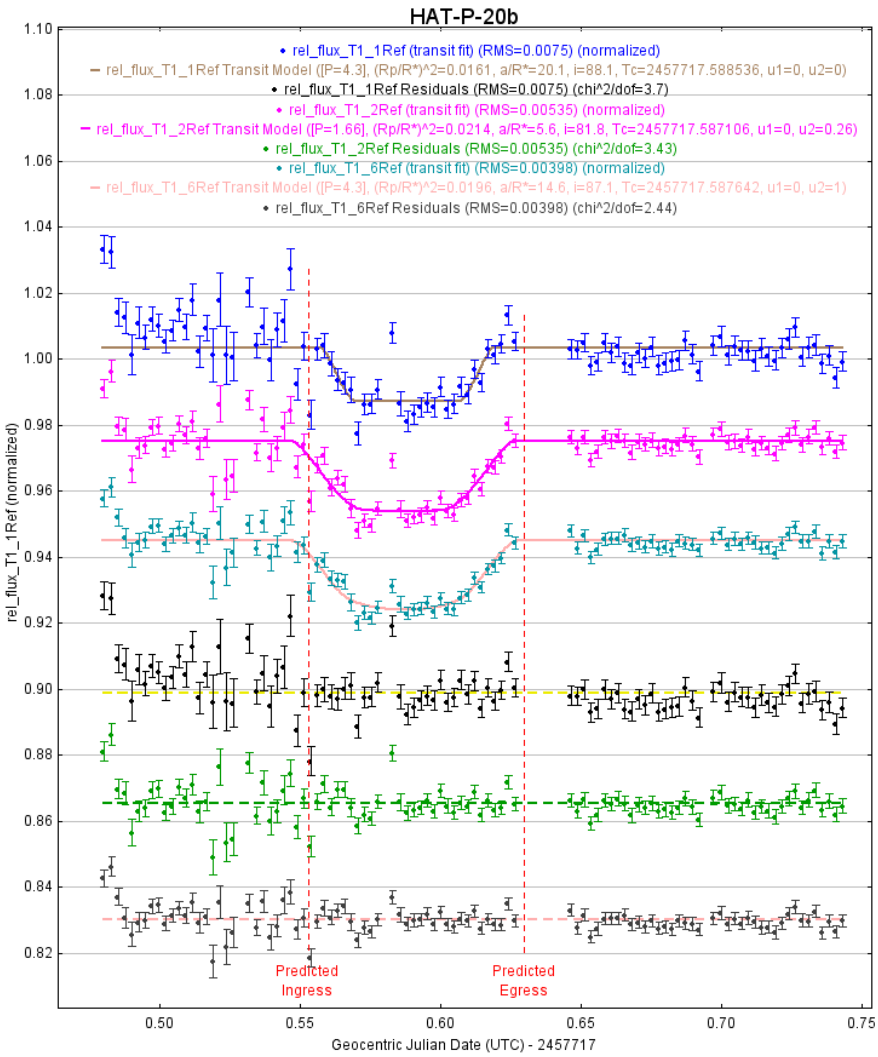

Figure 2.5: A comparison between one reference star, two reference stars and six reference stars with a transit of HAT-P-20 b. The light curves are first, then the residuals from the transit plot. The first light curve has one reference star, the second has two and the third has six reference stars.

3 Method

Chapter 2.1 outlined the background to the predicted precision. There are three main steps used: (1) Calibrating the setup for the predicted precision, (2) Selecting which exoplanet to go for, (3) Analysing the data through AIJ.

Due to the number of different telescopes and pipelines that the scientific images come from, a near universal method for calibrating the images and getting the data from the images was used. However, images from Bayfordbury are already calibrated and plate solved, whereas with all the other telescopes the images are not calibrated and plate solved. However, sometimes the Bayfordbury images were also not plate solved due to it failing mainly because of a lack of stars in the image.

Primarily the R filter was the first filter that was looked at for each telescope, due to it being close to the TESS filter (Sullivan et al. 2015). That is apart from Bayfordbury which was only calibrated for the V filter. Though as chromaticity tests for TESS needed to be done, all the filters that had a big enough archival data set were used for the predicted precision setup.

The data was all analysed through AIJ, which was constantly being updated with more functions to help with the TESS follow-up. Once a transit had been observed then it was compared to the predicted uncertainty and the predicted plot.

3.1 Calibration

This section presents how the values for the predicted uncertainty were worked out for the website. It also describes how the raw scientific images where calibrated and plate solved.

3.1.1 Calibrating Images

Calibrating the images is an important part, to remove the problems that are due to using CCDs. It is also important to plate solve the images, so that the positions of the stars are known. This has changed over time in order to speed up the process, the final way to calibrate the images was using the AstroImageJ's CCD data Processor function:

1. Find the plate scale of the scientific image in arcsec per pixel. If it is known already then next stage. If not then nova.astrometry from Lang et al. (2010) is used to plate solve one of the images in the sequence before the calibrations.

2. Looking at some of the calibration files in Aperture Photometry Tool (APT), with the image histogram to see if anything is suspect (flats should be above 10,000 ADU, bias near uniform).

3. Then the AIJ CCD data Processor is used to create the master bias, dark and flat files from the individual calibration images. This step and the next step can be done in one go. But doing it this way allows the master calibration images to be viewed before being applied to the scientific images.

4. Enter the Right Ascension (RA) and Declination (DEC) of the target and the telescope location in AIJ. Then enter the plate scale into the AIJ plate solver tool. Then process the scientific images that need correcting and the master files. AIJ will then go through and calibrate the images before plate solving them.

The scientific images are then ready for either, the calibration of the setup or for analysing a transit.

3.1.2 Calibrating a Setup for the Website

This subsection details how the information, which the website requires in order to predict the uncertainty, is worked out. The website requires specific information about the telescope and camera, some that can be worked out and others that need to be calculated by images.

The website splits the information that needs to be worked out into 4 parts (phases). This is so that not all the information has to be worked out all at once. For each part that is completed more tools are unlocked. The predicted uncertainty is provided once all the information has been worked out.

For the first part, get the specific latitude and longitude of that telescope in degrees; the horizon limit of the telescope, assuming a non-equatorial telescope or the lowest altitude that can be observed with it. This is all the information that is needed for part 1.

For part 2, the binning, filter type, telescope and name of the organization use required for the RTML. Then the time separation (dead time) needs to be calculated. This is the time between the end of an image and the start of the next. This is mostly the same for each binning for a particular camera/ telescope. This is done by getting a sequence of at least 5 images back to back and then calculating the time difference between the images with respect to the previous image and subtracting the exposure time to work out the time separation.

Part 3 of the setup requires calibration files as well as actual images for the analysis of the sky. For this reason it is split into 2 sections, the calibration files and the sky background. This part is necessary for the predicted uncertainty and is based on the work by P. J. Beck (2018).

Calibration files

The individual calibration images are analysed through PYTHON programs that were created by P. J. Beck (2018). Each calibration image set bias, dark and flats has to be calibrated independently. The bias and dark images are processed by the same PYTHON program, whereas the flats are processed through a slightly different program.

During this a quicker method was found, due to the changes that had to be done in order to make PYTHON work with twilight flats. This changed the time from up to 2 hours per calibration set to 15 minutes. However, it is now all manually done using AIJ rather than by code.

The code works out the values by calculating the SD at each pixel location over the calibration images. This produces an image with each pixel location and it's SD. Then depending on the type of calibration image different things are done to this SD image. For the Bias the average is taken. For the dark the average is also taken but is divided by the exposure time used.

The flats have to be normalised so that each file has an average of 1. Then the SD image can be made. This removes the problem of twilight flats having different average counts. The SD image for the flat then has the SD of it taken as the value used.

Sky Background

There are two numbers that are used to predict the noise expected from the sky background, sky constant and sky SD. Sky Constant is the number of electron counts per second, the sky background is expected to be the sky background with no objects in the field, whereas sky SD is the variation of the sky over the image and over time.

As the brightness of the sky is closely tied to the moon phases, there could be differences in the values. So these numbers could be calculated for different conditions, like Southworth et al. (2009), that has dark, grey and bright sky conditions. This has not been done as the effects of the sky noise has been low (<1%) compared to the other sources of errors.

The Sky Constant and Sky SD are worked out by using APT, with calibrated scientific images at different times/ locations/ moon phases. This is done by applying a large non-sky background subtraction aperture on the image, in an area that is devoid of stars. This process is then applied over different areas of the same image as well as many different images.

Once all the images have been analysed. The total counts in the aperture is then divided by the aperture size and the exposure time of the image. This is then averaged to get the sky count per pixel per second. The sky SD is then the average of the sky sigma divided by the exposure time used.

The final bit of information needed for part 3, is the scintillation value for the telescope. This is worked out by using equation 3.1. The telescope aperture diameter (D) and the telescope altitude in metres (h) which are input into the equation. This works out the scintillation error, for the telescope at an air mass of 1 and an exposure time of 0.5 seconds.

$$\sigma_{\text{scint}} = \frac{0.09}{100^{(2/3)}} D^{(-2/3)} e^{(-h/H)} \tag{3.1}$$

Part 4 is also split into 2 sections, like part 3. The catalogue to instrument magnitude conversion requires a lot of images and processing. The first section though just requires some more information about the telescope and camera: the focal length in mm, the pixel size in μ m, the number of pixels that the smallest axis has and the extinction coefficient for the airmass based on the filter being used.

The final bit for this section, is to work out the linearity limit for the CCD being used. CCDs are mainly linear in terms of the number of photons to electrons but, as the CCD approaches the saturation limit there is a much larger nonlinear relationship due to the reduced probability of capturing photons in nearly full pixels (Baldry 1999).

There are many different ways to find out the linearity limit of a CCD. There were 2 methods used depending on whether dome flats were available or not. Dome flats make it easier to work out the linearity limit as the source light will be constant over the different flats.

When dome flats were available, flats were taken with different exposure times. Then they were plotted with the mean count over the flat versus the exposure times used. With enough data points it can be seen where the CCD is linear up to in electrons.

If dome flats were not available, then this was calculated after the catalogue to instrument magnitude section, as it used the plot that was created to roughly estimate the linearity limit. This was done by looking at stars that had a high peak pixel value with a known magnitudes and checking to see if there was an undercount compared to the predicted counts. That would suggest that the star was past the linearity limit, giving an upper bound for the linearity limit.

Catalogue to Instrument Magnitude

This is the final section and part for calibrating the telescope setup for the website. It involves using lots of images to analyse them for standard stars. Then a plot can be produced that shows the instrument magnitude at an airmass of 1 and an exposure time of 1 second against the catalogue magnitude. From this the instrument magnitude can be predicted based on the catalogue magnitude.

Due to the amount of time that the method from P. J. Beck (2018) took, which was by using APT on each target for each standard star which is very time consuming, a new method was needed to speed up the process. Using AIJ as it has the ability to place apertures based on where stars should be, which speeds up the process considerably. For each binning and filter combination the following was done for each sequence of images from the same campaign or individual image:

1. One of the raw images in the sequence was downloaded.
2. Using nova.astrometry to plate solve the image. (http://nova.astrometry.net/)
3. The centre of the image in right ascension and declination from the plate solved image was used to look up the stars in the field. A function on the website processed the known magnitude value for the filter used. This creates an RA/ DEC list of the stars for AIJ.
4. If there were no stars of known magnitude in the filter being used, then that image sequence was skipped, until there were stars with known magnitudes in the image.
5. Then the remaining images from that sequence of images were downloaded and the calibration images for it as well.
6. The images where then calibrated as described by section 3.1.1.
7. Once the images were calibrated and plate solved, they were opened in AIJ and the aperture sizes were set based on the seeing profile of a non-saturated star.

8. Then the RA / Dec list is imported into AIJ. This places the apertures automatically around the stars in the field that have a known magnitude in the filter being used.

9. Then the multi-aperture photometry is performed, using the previous loaded apertures and varying the aperture size based on the stars individual FWHM. The data is then saved after it has been processed.

10. Afterwards the data was input into the website so that it could be reduced, to only the information that was needed. This process also added information about the targets like, the name of the star and its magnitude and magnitude uncertainty. It took the exposure time, filename, airmass, ADU count on the target and its peak pixel value. Then converting the ADU into electrons.

11. The data is then saved into a table so that it can edited together for each setup.

12. If the linearity limit is known, then any star that is above it in the brightest pixel is removed. The rest are checked to see if they have a large magnitude error. If so then they are removed too.

13. The process is then repeated with lots of images and targets. The method below is used once a few images have been processed but is best once many different images have been processed.

In order to compare the instrument magnitude to the catalogue magnitude, the instrument magnitude has to be adjusted for the exposure time and air mass. This is done by using equation 2.16 to work out the instrument magnitude for a one second exposure time and at air mass of one.

The atmospheric extinction coefficient ε, that is needed for equation 2.16 is set by an extinction model based upon which filter was being used (Schmude 1994). This is different to P. J. Beck (2018) method that used observations of a target as its air mass increased, to model the airmass, as this method gave different extinction coefficients depending on where the air mass started.

The instrument magnitude from equation 2.16, is then plotted against the catalogue magnitude. Afterwards a linear trendline is added to the plot. The linear trendline gives the *Gradient* and *Bias* values, which are used to predict the instrument magnitude from the catalogue magnitude.

The linear trendline can fluctuate, if there are not enough good data points. So a large amount of images are needed in order to get a good fit. The images need to be from different exposure times, target magnitudes and air masses.

The last bit of information needed for part 4 is the expected atmospheric seeing. This is important when calculating the peak linearity. By using the data from the catalogue to instrument magnitude. It is possible to get a good idea of what the typical seeing is and what the best seeing is. The best seeing seen is used, as it has a strong effect on the expected peak pixel. This is done by back-calculating the seeing from the following equation:

$$Seeing = \frac{Scale}{0.51}\sqrt{\frac{Count}{2\pi * (peak + (sky * t_{\text{exp}}))}} \tag{3.2}$$

Where,
Scale is the plate scale in arcsec per pixel,
Count is the total ADU count from the target,
peak is the peak pixel value,
sky is the sky constant from the sky background,
t_{exp} is the exposure time in seconds.

Twilight flats

Due to the PIRATE and the TRT Network using twilight flats, the timings of the flats were analysed as well as the mean counts from them, in order to compare different twilight flats, from different days. The angle of the Sun was used at the mid-exposure of the flats.

3.2 Selecting Exoplanet Transit

This subsection deals with the information, which needs to be looked at before trying to observe a transit. The most significant bit of information was to look at the expected weather pattern.

The website uses the dark sky website (Grossman and Turner 2019) to see what the cloud coverage is likely to be over the next 48 hours to 7 days. It also predicts what the expected rainfall and wind speeds will be. This helps to plan which telescope sites are going to be the best for observing transits.

The data from the dark sky website (Grossman and Turner 2019), about the cloud coverage is best at predicting whether or not it is going to be clear that night, rather than when during that night it will be clear. This is due to the imprecise nature of predicting the weather.

Below is a list of questions that were used once a night was predicted to be clear or mostly clear and to see if a particular transit should be observed or not. The following list details things that had to be worked out before trying to observe the transit. It is mostly in the order that was used, though some parts can be reordered;

1. How long can the target be observed, before the start of the transit and after the end of the transit with at least 30 minutes either side of the transit but preferably an hour if not longer?
2. What is the transit length? If it is too long, then there is more of a chance that the weather could stop the observing?
3. What is the change of the air mass over the observation? How low to the horizon does it get?
4. If a TOI then has it been observed before, what did they find?
5. What's the uncertainty in the transit time? Especially for TOIs.
6. What's the filter that is going to be used and what's the magnitude of the star in that filter?
7. What phase will the moon be during the observation, and will it be above the horizon?
8. What exposure times, are valid for observing that magnitude for the proposed telescope?
9. What is the transit depth expected to be?
10. What exposure times are needed in order to get the required uncertainty to see the transit?
11. What is the ratio of the expected uncertainty to the transit depth? If the transit depth is less than the expected uncertainty the transit is unlikely to be seen in the data.
12. How many images are going to be made for the selected exposure time?
13. How crowded is the area that is going to be observed, are there any stars that could affect the photometry data?

The Transit Follow Up Tool was used to predict the transit events for confirmed planets, and most TOIs. Not all TOI were made public at the same time early on, due to the system not being all up and running in time[1].

[1] https://tess.mit.edu/toi-releases/toi-release-faqs/

The website tool could also not show the comments from the TESS transit finder, which detailed what the previous observations found as well as what data should be collected to help the TESS follow-up program. So the TESS transit finder was used for the TESS follow-up sections.

3.3 Analysing through AstroImageJ

This subsection deals with how the images were analysed for transits through AIJ once they had been obtained. AIJ is the preferred photometry tool for uses with TESS data as it creates a standard output.

It also can produce most of the data sets, which the ExoFOP-TESS want to see, in order to check how good your data is. The raw images are calibrated and plate solved through the process described in section 3.1.1

There were two different processes used depending if it was a TOI or a confirmed exoplanet. They are similar in approach but differ a lot if the TOI being looked at does not have a transit. Firstly the aperture positions of all stars in the images that have known catalogue magnitude are downloaded.

If a TOI then the apertures were downloaded by using the link from the TESS Transit Finder (Jensen 2013). If a confirmed exoplanet then one of the tools from the website (Transit Follow Up Tool) is used. The RA and Dec from the centre of the image is used to download the apertures.

The calibrated images were then opened in AIJ, with the apertures being imported onto them. The next bit was to select the aperture sizes by using the AIJ seeing profile. This was done by finding the main target (T1) then clicking on it and saving the recommended aperture sizes. Once the aperture sizes were selected the multi-aperture photometry tool was used.

As all the images were plate solved, the aperture positions and previous apertures could be used. The reference stars were then selected, using stars that had a similar total ADU counts to the target star, making sure not to select stars that have peak pixel values that are above the linearity limit. As AIJ has warnings when a star has gone past the linearity limit and saturation point, this is less important. For confirmed exoplanets, the reference stars were primarily the closest stars to the target star.

For TOIs, the reference stars were not the closest stars to the target due to them being in the aperture that the TESS data would have used. But by using the downloaded apertures, the stars in the TESS aperture were automatically selected. Thus they could be checked if no obvious transit could be detected on the main target.

Once all the images have been analysed, the main target and some of the reference stars are plotted. The reference stars are then analysed by deselecting one of them to see if it is good or not removing any that are suspect. This is repeated for each reference star and then repeated again to see if any of the removed reference stars have effected a reference star enough to now be a bad. The reference stars are removed if they have high RMS, or trends in a different direction compared to the other reference stars. If all the data points on the same image show something odd then the image may be rejected.

The predicted start and end time of the transit in Barycentric Dynamical Time (BJD_{TDB}) is input into the AIJ transit model. The title of the plot is changed to match the system being analysed. If a TOI, the title is set by the TESS input catalogue number rather than the TOI number. The start of the observation in UTC days is added to the title as well.

The subtitle of the plot comes in 4 parts: the site/telescope that was used, the filter that was used, the exposure time in seconds and the final part is the aperture sizes used in the photometry. This is based on what is used for the SG1 TESS follow-up program[2].

The target is added to the light-curve plot, where a transit model fit is then added. The period of the exoplanet and the radius of the star is input into the transit model fit. The residuals from the transit fit is then plotted under the transit fit.

The data is then detrended, first by airmass and then trying other detrending parameters until the lowest BIC (Bayesian Information Criterion) is achieved. At most two detrended parameters were used, unless the X and Y positions of the target were used, in which case one more detrended parameter could be used. If a TOI and no clear transit is seen, then the stars enclosed in the TESS aperture were checked to see if they had any transit or eclipsing binary like events.

Once the detrending parameters were set, the transit fit was saved and the light curve plot was made with 4 plots, one with just the data of the target, one detrended with air mass and another with the transit model and the detrended parameters. The final plot is the residuals from the transit fit.

There are six data sets, which are always at the bottom of the plot. They collectively give details about the changes of the conditions over the observation. They are: the air mass, the sky counts per pixel, the mean FWHM of the target (width), the total counts from the reference stars and finally the X and Y position of the main target.

[2]https://astrodennis.com/SG1Guidelines.pdf

An example of the plot that is produced by AIJ is Figure 3.1, showing the light curve for WASP-52 b from the CKT in V. The main 3 plots: raw flux change (blue), detrended by airmass (red) and the transit fit (green) with the residuals (black). The six others are at the bottom: width (mean FWHM) of the target (light grey), the sky counts per pixel (yellow), air mass (teal), the total counts from the reference stars (brown) and finally the X and Y position of the main target (pink and light blue respectively).

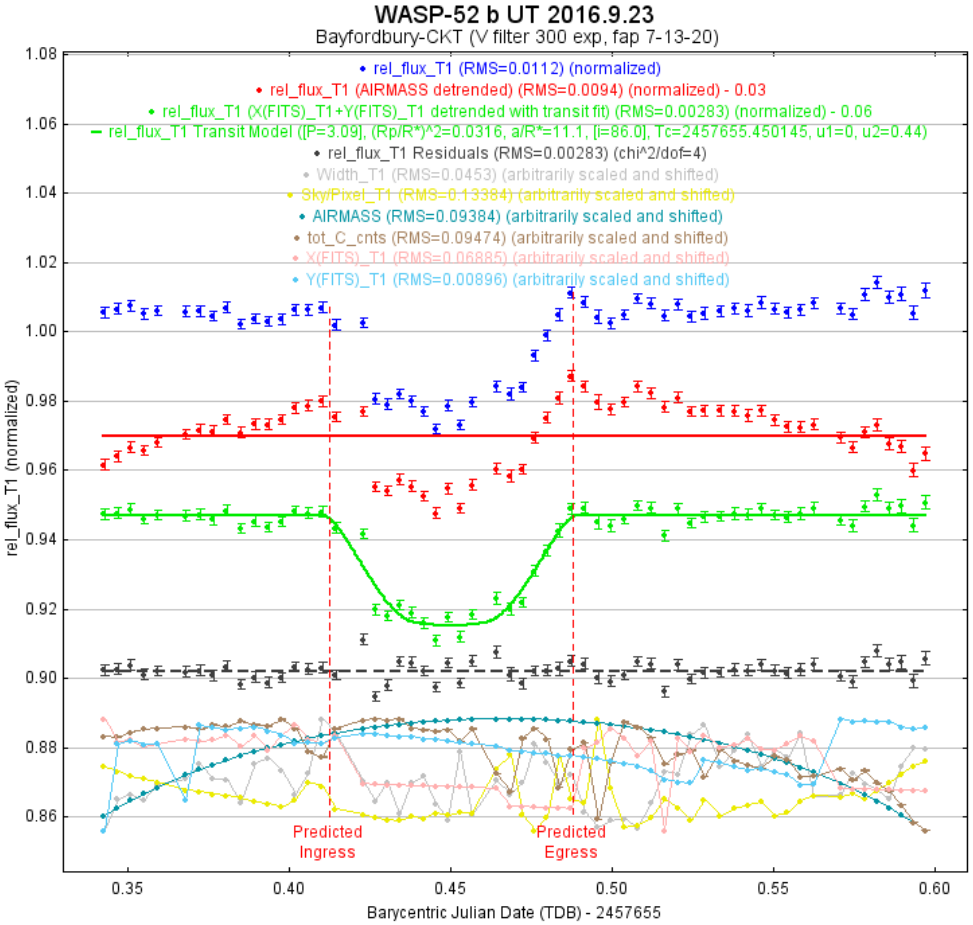

Figure 3.1: An example of the plot that is produced by AIJ showing the light curve for WASP-52 b from the CKT in V for a exposure time of 300 seconds. In order, going down the legend: the raw flux change, detrended by airmass, the transit fit, the residuals, width (mean FWHM) of the target, the sky counts per pixel, the air mass, the total counts from the reference stars and finally the X and Y position of the main target.

All the data files (measurements table, apertures and light curve plot) that are produced though AIJ, are saved in a new folder with the aperture sizes used. Then the images are reanalysed using different aperture sizes (unless a nearby star was in the way) to check if this results in a reduction of the RMS of the transit fit and transit itself. If it does then this is used the reported light curve plot and fit model. If the exposure time is short enough and has enough data points, then the data might also be binned to see if this gives a better fit.

Transit vs Predicted uncertainty

As P. J. Beck (2018) only used one reference star for the analysis, the effects of the reference star could have affected the precision. So for this analysis multiple reference stars were used in order to reduce the reference star effects. The RMS of the target fit was then compared to the predicted uncertainty based upon the system setup that was used.

The predicted uncertainty was worked out for the average airmass over the whole observation, rather than the start, middle and end of the observation. The airmass was rounded to the nearest 0.05. This is so that the air mass could have been calculated based upon the start and end time of the observation. The magnitude of the target star was also rounded to the nearest 0.05 magnitudes.

Where the magnitude of the star in the filter being used was not known, the instrument magnitude of the star, over the observation was plotted against the airmass. This was used to work out what the instrument magnitude would be for an airmass of 1. That was then inputted into the predicted uncertainty, rather than the actual counts from the target.

If the observed data showed a clear transit, then the predicted transit plot was overlaid with the data and compared. The data that comes from the predicted transit model, is in magnitude and minutes, where the base line of the off-transit time is set to one. In order to analyse it with the observed it needed converting.

The time was set by using the mid-transit time, from the transit model fit for the observed data which the mid-transit of the predicted transit was set to. The magnitude was adjusted by just adding a constant to the value, which was calculated to either match the off-transit or the transit depth. The transit depth was less preferable but depending on how much off-transit was observed.

4 Results

The transits have been broken down into each organisation with a telescope(s) and then their chronological order. Table 4.1 shows the transits that have been analysed and include whether or not it was a false positive (FP) or a confirmed planet (CP), the RMS from the transit fit, the predicted uncertainty and then the percentage error.

Table 4.1: List of transit results

	Exoplanet	FP/CP	RMS of fit (ppt)	Predicted uncertainty (ppt)	Percentage error (%)
TRT	TOI 689.01	FP	2.538	2.583	1.77
	TOI 516.01	FP	10.574	10.638	0.60
Bayford-bury	WASP-52 b	CP	4.275	4.306	0.72
	HAT-P-20 b	CP	3.314	3.319	-0.15
	HAT-P-20 b	CP	2.761	2.763	0.06
	KPS-1 b	CP	3.562	3.577	0.42
	TOI 1164.01	FP	3.40	3.373	-0.79
	TOI 1455.01	FP	2.61	N/A	N/A
PIRATE	WASP-12 b	CP	2.977	2.960	-0.56
	HAT-P-44 b	CP	3.186	3.219	1.06

The predicted precision for TOI 1455.01 was not available as it was observed in a filter that was not setup for prediction. The RMS from the fit is the RMS from the corresponding transit fit for un-binned data.

For the TOIs that were observed, only the ones that had no obvious transit event were checked to see if there were any eclipsing binaries within the TESS aperture.

For the confirmed exoplanets, the observed model fits have been compared to the literature. Some of the exoplanets observed have very few papers that detail the system. The model fits from AIJ do not give uncertainties, so the observed RMS and exposure time have been used. The percentage errors from them have been rounded to 1 decimal place.

The mid-transit times have been compared by using the published period and mid-transit time and their associated uncertainties, in order to calculate the mid-transit time of the transit that has been observed and compare that with the observed mid-transit time.

4.1 Thailand Robotic Telescopes Transits

Only 2 transits were observed using the Thailand telescopes. TOI 689.01 was observed by the Spring Brook Observatory (SBO) telescope. The TNT was used to observe TOI 516.01.

4.1.1 TOI 689.01 on 2019 05 11 with TRT SBO

The plan was to start observing about 30 minutes before the predicted start then stop about 1 hour after the predicted egress. The weather was clear. The start was first delayed due to the observing site not starting until the Sun is 18 degrees below the horizon rather than the predicted 12 degrees. It was then further delayed due to the bias and dark calibrations images being taken. That meant the telescope only started about halfway through the transit.

The exposure time was 60 seconds as the main aim was to see if the event on target could be detected. The binning was set to 1x1 binning, as the field was very crowded with 34 other stars in 1 arcmin and 180 more in 2.5 arcmin of the target.

On 31st May 2019 it was reported that for the QLP TOIs $(R_{\rm p}/R_*)^2$ is the transit depth, instead of the flux deficit at mid-transit. Those two numbers can be vastly different for V-shaped or near-V-shaped transits (many are, since the QLP uses the 30 minute full-frame images). In order to know which stars need to be searched for NEBs, the depth in terms of flux deficit at mid-transit is needed (Collins 2019).

The QLP pipeline was later updated to report the needed depths. The target was meant to have a depth of 8 ppt but due to the QLP problem this was revised down to 2.5 ppt at the mid-point. So the likelihood of seeing the transit depth was reduced.

There was a problem with the flats as no new twilight flats had been taken. So an older flat master was used. They were taken 3 months ago and were not the best as the raw mean count over the flats were around 5,000 ADU. Given that the bias shows around 1,011 ADU, which means the signal to noise of the flats is low.

The RMS of the target was 2.538 ppt when detrended by airmass. The predicted uncertainty was 2.583 ppt based on 5 reference stars of the same type. This means the predicted uncertainty is off by 1.77%. Figure 4.1 shows the light curve for the target showing no transit.

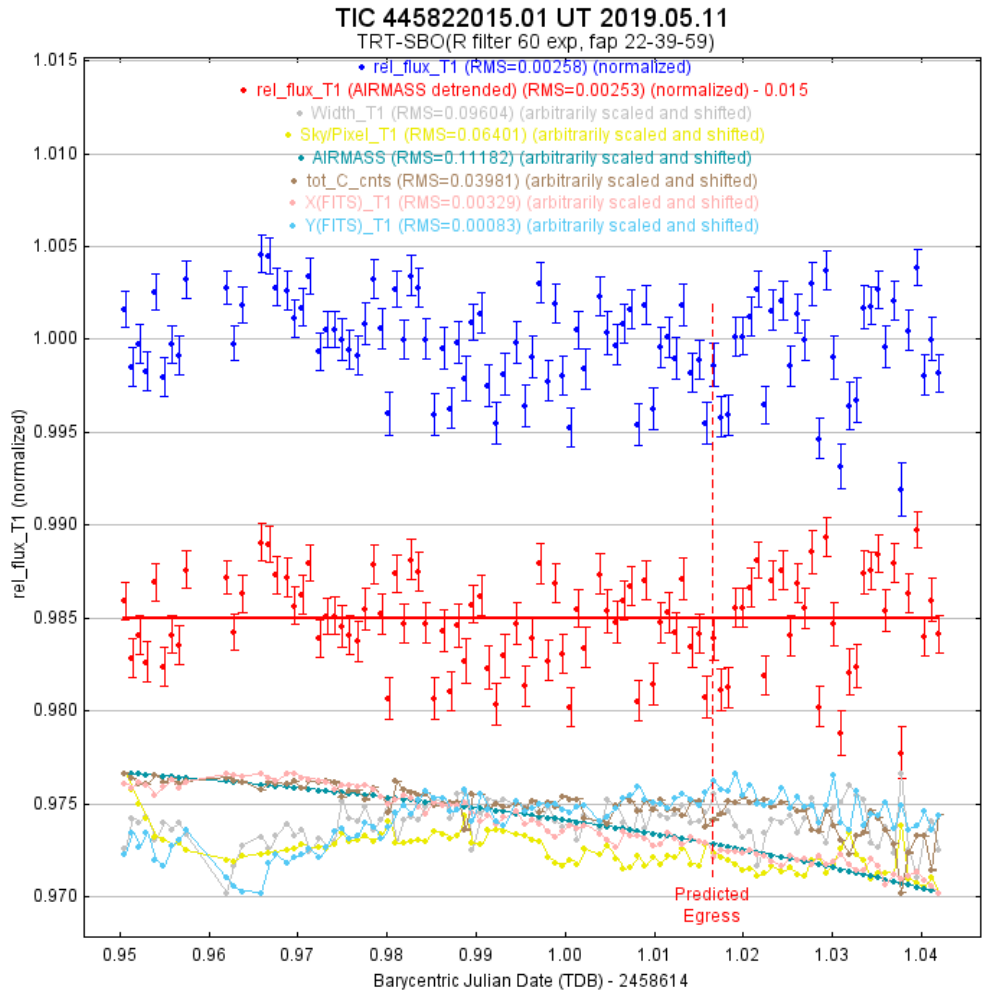

Figure 4.1: Target light curve then it detrended by air mass. There is no clear transit.

Overall results from TESS: "Phil Evans observed a full event on 2019 05 13 in Rc and confirmed a greater than 130 ppt on a star that was 3.1 magnitudes fainter in one of a pair of stars 44 arcseconds to the north of the target which would be an NEB." That would be consistent with the offset suggested by the QLP report. Also, "the target star light curve excludes the predicted 2.5 ppt event on target". (Relles, Kielkopf, and Evans 2019).

Then, "Howie Relles observed an egress that was the full transit and roughly 50% of off transit time on 2019 06 08 in I-band. That reconfirmed the NEB previously detected in the pair of stars 44 arcsec to the north". In Howie's data, "the pair is resolved and the fainter star (T25) hosts a 250+ ppt eclipse" (Relles, Kielkopf, and Evans 2019).

The target star light curve mostly rules out the 2.5 ppt TESS detection. The QLP suggests an approximately 2 TESS pixel offset to the north that is consistent with the NEB position. So the TOI was retired as an NEB (Relles, Kielkopf, and Evans 2019).

When looking at the fainter star, that was the actual source of the event. It was not possible to separate it from its nearby star from the SBO data due to the plate scale and the seeing.

4.1.2 TOI 516.01 on 2019 10 31 with TRT TNT

Before the observation with the TNT, the TOI 516.01 had been observed five times before all within a week of each other and just 2 weeks after it was published on the ExoFop TESS (2019 08 18).

Eric Girardin, "observed a full transit on 2019 03 29 in a clear filter and confirmed a roughly 35 ppt event on target using a 9 arcsec aperture" (Girardin, Collins, and Bieryla 2019). Giovanni Isopi and Andrea Ercolino, "observed a full transit on 2019 03 30 in a clear filter and confirmed a roughly 30 ppt event on target" (Girardin, Collins, and Bieryla 2019).

Howie observed it on 2019 04 29 in ip filter and detected a 30 ppt event on target using an 5.1" aperture (Girardin, Collins, and Bieryla 2019). Kevin and Karen," observed a full transit on 2019 04 02 with 2 different filters and found 30 ± 2 ppt in Zs and 27 ± 5 ppt in gp" (Girardin, Collins, and Bieryla 2019).

Allyson Bieryla, "observed a full transit but with no pre-out of transit time but very long post-out of transit on 2019 04 05 in V filter and confirmed a 25-30 ppt V-shaped transit" (Girardin, Collins, and Bieryla 2019).

The ExoFOP said that "the next observation should attempt simultaneous full transits in blue (U, u', B, g') and very red (zp, Zs) filters to check for chromaticity".

The aim was to start observing TOI 516.01, 60 minutes before the start of the transit and continue until 60 minutes after the end of the transit. The observations were cut short by a few images in order to take calibration images that had not been taken yet. The target was a very faint star in the filter being used, 18.56 in B.

The exposure time was settled on 200 seconds, so that enough images were taken. This meant that the peak count was around 4,000 ADU before the calibrations were applied. There was a problem with the filter changer that meant it could not be observed in a red filter during the same transit.

CCD Flat

The flat field images were taken at twilight and showed that the CCD had a very steep drop off around the edge of the CCD which can be seen in Figures 4.2 and 4.3. The steep drop off may affect the results as it may bias the centre to be too positive.

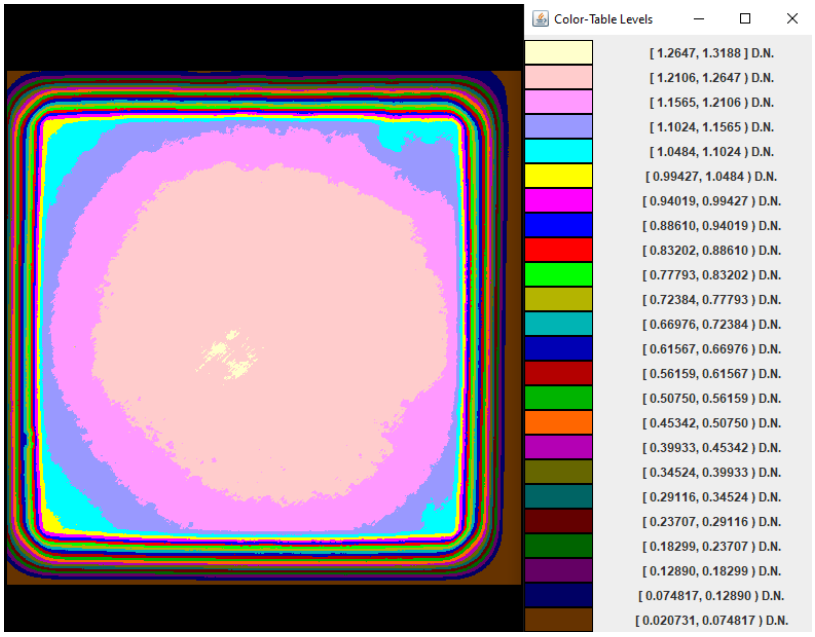

Figure 4.2: The master flat from TNT, showing the master flat and the colour-table from APT.

A test was conducted to see whether it would give a better fit if only the centre part of the flats were used. It was found that it made no real difference in the analysis of the transit, apart from setting a barrier on the calibrated images that could be used to make sure that stars were not taken in that section where the flat values would change a lot.

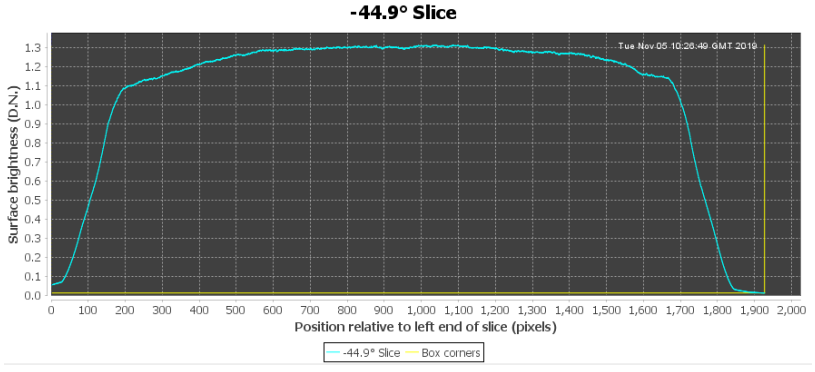

Figure 4.3: Slice plot of the Master flat at an approximate 45 degree angle going from the top left to bottom right of the flat, showing what the drop off at the edge of the flat is like.

Light curve

The transit was predicted to start at BJD fraction 0.319 and finish at 0.363, whereas figure 4.4 shows that the transit has moved by about 30 minutes later than predicted, which is what the uncertainty of the transit time was.

There is a drop in all the stars at the predicted ingress which goes back up at the predicted egress. That is likely due to cloud as the drop in the instrument magnitude of the stars is around 0.5 mag. That is more than ten times the expected transit depth and it can be seen in all the stars' data.

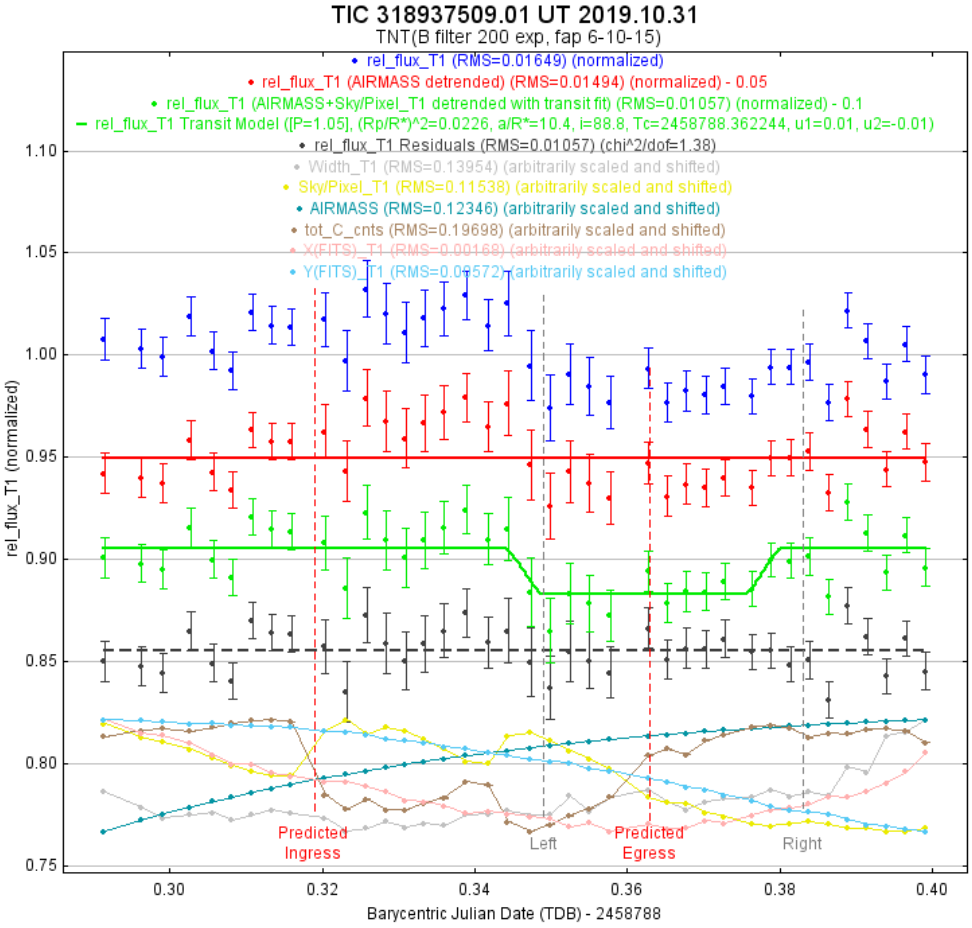

Figure 4.4: Light curve for TIC 516.01 from AIJ. Showing the data for the target, then detrended by airmass. Then the transit fit detrended by airmass and sky brightness with the residuals from the fit.

The sky counts per pixel increases at the ingress and decreases at egress, showing that it might be cloud that picked up the moon light which was at 17% brightness. This cannot be configured due the remote sky camera being offline during the observation.

The predicted uncertainty was calculated based on the average counts over the observation rather than the catalogue magnitude. This is because there was not enough data to calculate the instrument magnitude versus catalogue magnitude plot for the TNT. The predicted uncertainty was 10.638 ppt. The fit gave a RMS of 10.574 ppt which means the predicted uncertainty is only 0.6% off.

Period

The period of the target is of 1.04855 ±0.000073 days from ExoFOP. The uncertainty in the period would lead to an uncertainty of about 30 minutes in the transit time based upon the number of periods that have occurred since the TESS mid-point.

As the Table 4.2 shows there is a positive drift from the other observations based on the difference between the predicted mid-point and the data model mid-point. This gives evidence that the transit is not where the predicted ingress and egress is.

Table 4.2: Table showing the drift from the TESS with T_{mid} in BJD_{TDB} - 2450000

	Eric Girardin (Clear)	Kevin and Karen (zs)	Kevin and Karen (gp)	Allyson Bieryla (V)	TNT (B)
T_{mid}	8572.3434	8576.5388	8576.5404	8578.6340	8788.3628
Orbits	76	80	80	82	282
T_{mid} TESS	8572.3398	8576.5340	8576.5340	8578.6311	8788.3411
Δ	0.00355	0.00479	0.00641	0.00294	0.02166
Δ in mins	5.1	6.9	9.2	4.2	31.1

Result

With the transit not being where it was thought to appear, it means that a good model is hard to fit as there is very little post out of transit data. Later HIRES spectrum showed a double-lined H-alpha emission, with a delta-V of around 137 km/s (Crossfield 2019). That suggests that the TESS event is caused by a blended or hierarchical eclipsing system that means it is a false positive.

4.2 Bayfordbury Telescopes Transits

4.2.1 WASP-52 b on 2018 11 02 with CKT

The plan was to observe WASP-52 with a shorter exposure time than had been attempted at Bayfordbury before to get a better fit for the transit. This is because it has been observed at Bayfordbury 4 times before but with an exposure time of 300 seconds to get the best performance. The exposure time of 60 seconds was used to get more data points but the performance would be worse than past Bayfordbury work on WASP-52 b.

It was observed 40 minutes before the transit started, and stopped observing 30 minutes after the predicted end of the transit. The moon was 27% full during the observation. Due to the shorter exposure time the data was also binned by 2 to see if this would give a more robust fit. There is a small gap of around 14 minutes just before the egress where the telescope re-positioned itself.

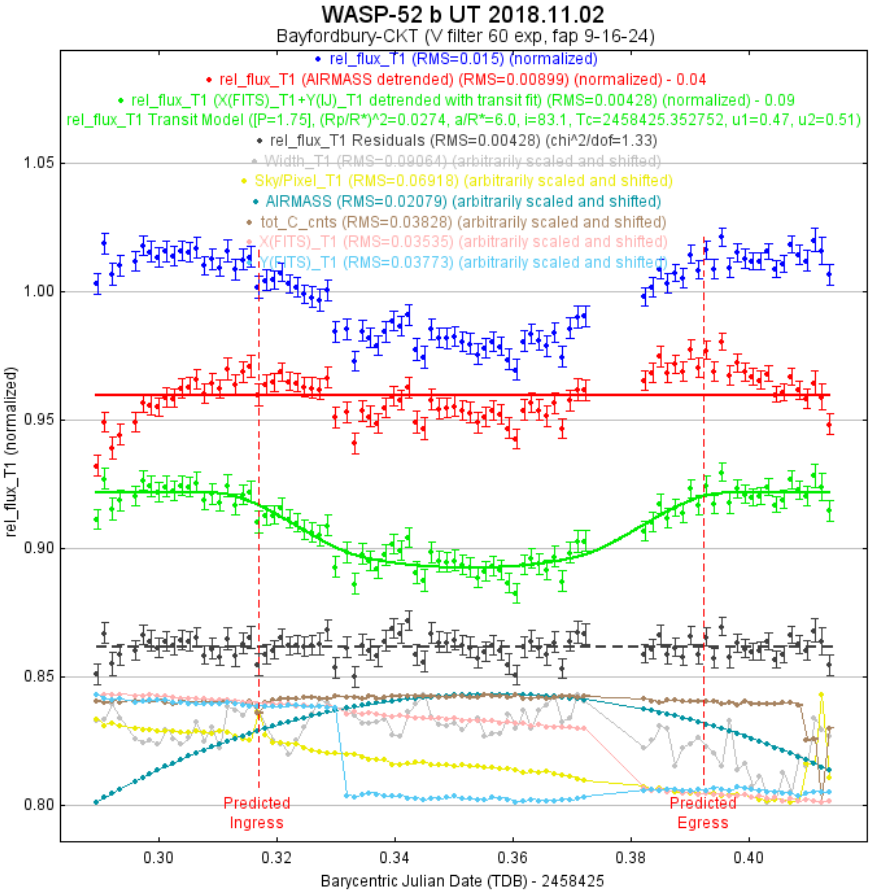

Figure 4.5: WASP-52b transit fit using AIJ. The target then detrended by air mass, with the model fit detrended by the position of the target on the image and its residuals.

The transit light curve for WASP-52 b is Figure 4.5, showing the transit data then detrended by airmass, finally the model fit with the residuals. Due to the telescope re-positioning itself, the X and Y positions was used as the detrended parameters rather than airmass for the model fit.

The predicted uncertainty over the observation was 4.306 ppt, the residuals of the fit giving a RMS of 4.275 ppt. That means that the predicted performance is only 0.72% off. Figure 4.6 was produced to compare the light curve fits of the data that had not been binned to the data that had been binned by 2.

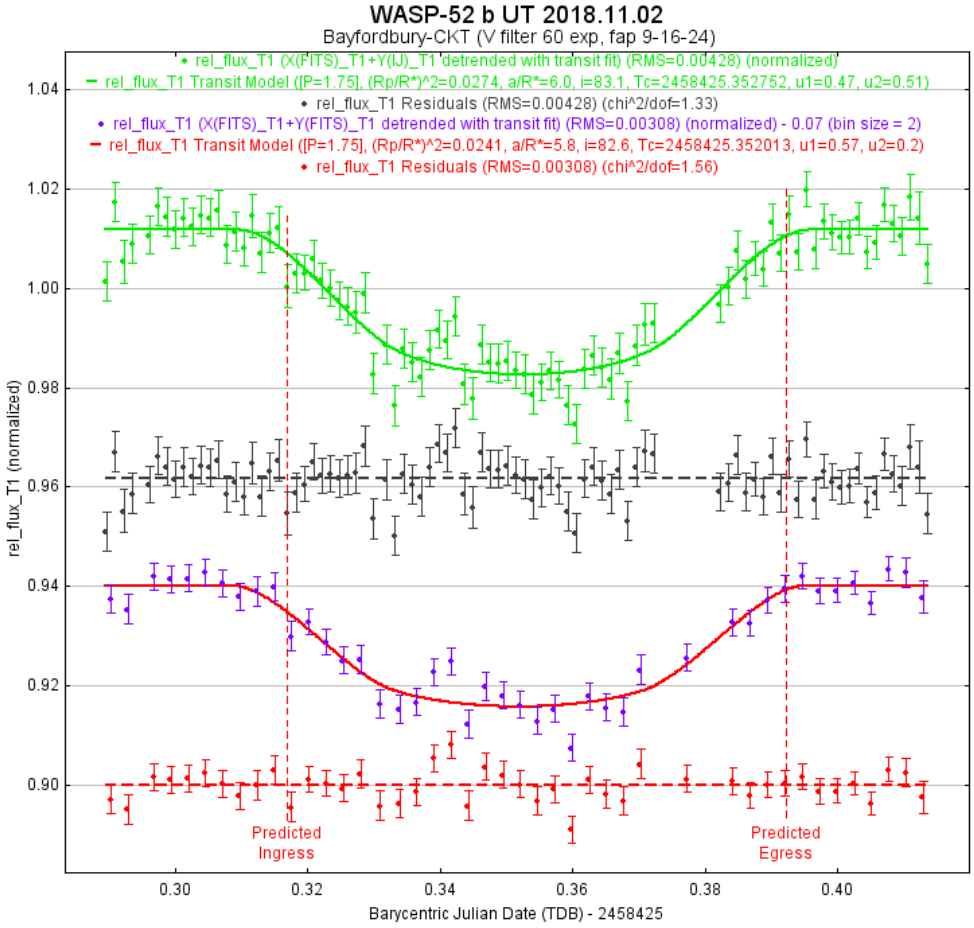

Figure 4.6: WASP-52b transit comparing the binned data and not binned data.

The predicted uncertainty for data that was binned by 2 would be the predicted uncertainty divided by the square root of 2 so would be 3.045 ppt. The RMS of the fit for the data when binned by 2 was 3.082 ppt which means the predicted uncertainty is only off by -1.2 percent.

Table 4.3 and 4.4 show the results from the fit with respect to the non-binned and binned data respectively. Hébrard et al. (2013) is the original paper that confirmed WASP-52 b and is based on 8 observations from 2008 to 2011. Öztürk and Erdem (2019) is based on 8 new observations and re-analyzing older transits to look for TTV.

Table 4.3: Results from fit compared to 2 papers

Parameter	Hébrard et al. 2013	Öztürk & Erdem 2019	Model fit	Error from Hébrard (%)	Error from Öztürk (%)
R_p/R_*	N/A	0.159 ±0.004	0.1656 ±0.0063	N/A	4.2
a/R_*	7.3801 ±0.1098	7.299 ±0.267	5.98	-18.9	-18.1
T_c (BJD_{TDB}) [2458425]	N/A	0.35461 ±0.00181	0.35275 ± 0.0007	N/A	-0.5
Inclination (Deg)	85.35 ±0.20	85.24 ±0.84	83.13	-2.6	-2.5
T14 (d)	0.0754 ±0.0005	N/A	0.0867 ± 0.0007	14.9	N/A
R_p (R_{Jup})	1.27 ±0.03	1.223 ±0.062	1.302 ±0.083	2.5	6.5

Table 4.4: Results from the binned data fit compared to 2 papers

Parameter	Hébrard et al. 2013	Öztürk & Erdem 2019	Model fit bin = 2	Error from Hébrard (%)	Error from Öztürk (%)
R_p/R_*	N/A	0.159 ±0.004	0.1551 ±0.005	N/A	-2.4
a/R_*	7.3801 ±0.1098	7.299 ±0.267	5.78	-21.7	-20.8
T_c (BJD_{TDB}) [2458425]	N/A	0.35461 ±0.00181	0.35201 ±0.0007	N/A	-0.7
Inclination (Deg)	85.35 ±0.20	85.24 ±0.84	82.6	-3.2	-3.1
T14 (d)	0.0754 ±0.0005	N/A	0.08615 ±0.0007	14.3	N/A
R_p (R_{Jup})	1.27 ±0.03	1.223 ±0.062	1.219 ± 0.07	-3.9	-0.3

The table 4.3 and table 4.4 show that the observed radius of the planet is close to the literature and within the errors. It is only -0.3 percent off Öztürk & Erdemwhen the data is binned. The transit time is longer than Hebrard. This is most likely due to the re-positioning before the egress that affected it rather than the transit being longer over the time.

Based on the data by Öztürk & Erdemwhen, the mid-transit time is slightly earlier than predicted by around 2.7 to 3.7 minutes depending on the fit type. This might also be due to the missing data before egress, but it is inside the uncertainties.

4.2.2 HAT-P-20 b on 2018 12 03 with RPT

The goal was to observe HAT-P-20 b an hour before the transit and continue until an hour after the transit. The RPT was busy with other plans so it missed the before out of transit time, so started just before the predicted ingress. There was a power cut at Bayfordbury just after the predicted egress, so the RPT lost power and stopped taking images.

The moon was below the horizon during the observation. There was a little bit of cloud at the start of the observation. There is a gap about a quarter of the way into the transit of about 10 minutes due to the telescope switching RTML plans.

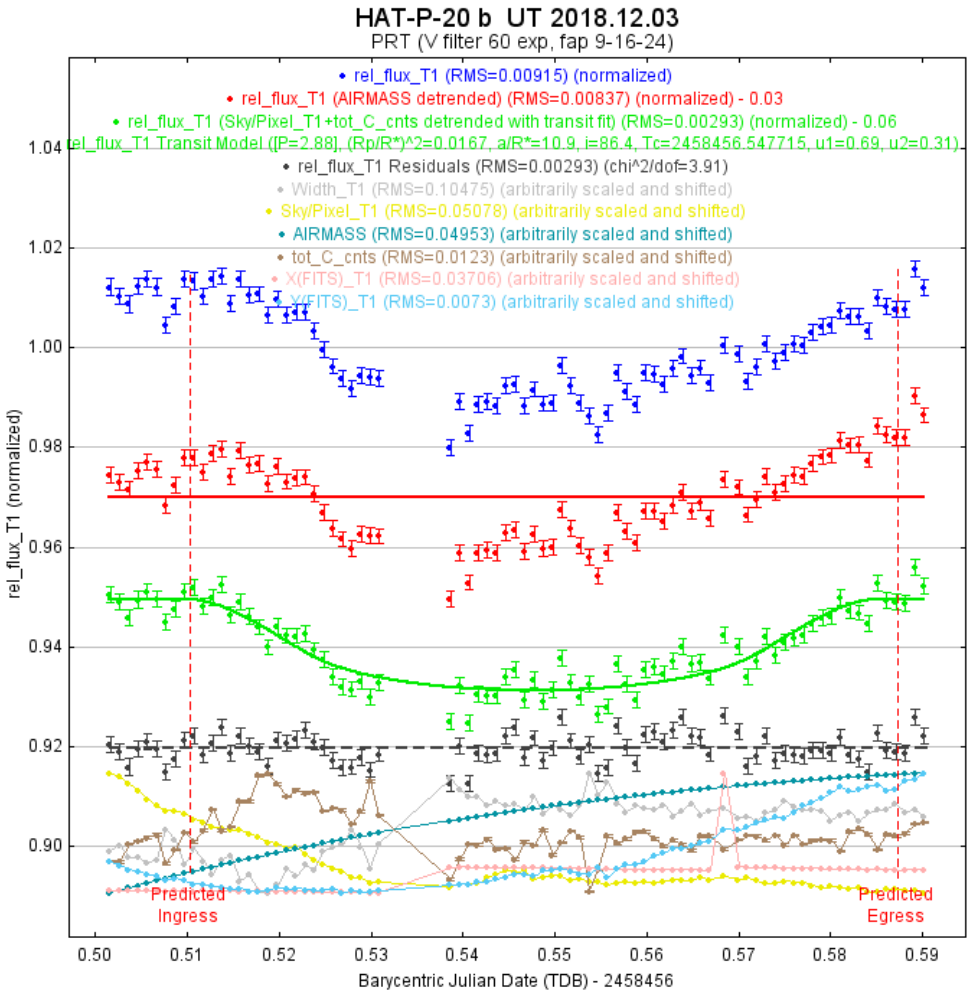

Figure 4.7: HAT-P-20 b transit. Data, then detrended by air mass then the fit using AIJ with the residuals.

The predicted error using 5 reference stars was 3.314 ppt and with no detrending the best fit was 3.319 ppt so only -0.18% off. Due to there being a high variation in the total counts and the sky brightness, the data was detrended.

Figure 4.7 shows the light curve for HAT-P-20 b from RPT. The fit is detrended by sky per pixel and total counts. The RMS over the transit fit was reduced to 2.927 ppt and as the detrended fit was not corrected for airmass the target was calculated at 2.935 ppt. This is a very good fit with the predicted uncertainty as it is only 0.29% off.

G. Á. Bakos et al. (2011) is the original paper that discovered HAT-P-20 b. There are not many papers that have detailed parameters for HAT-P-20 b. Data from 2 of the HAT telescopes which observed it for 6 months together and 2 more follow up observations at higher precision as well were used in G. Á. Bakos et al. (2011).

Table 4.5 shows how the fit parameters compare to G. Á. Bakos et al. (2011). Due to the small amount of off transit time observed, it is very good to see that the planet's radius has a good match to Bakos. The uncertainty in the mid-transit time from Bakos is around 7 minutes due to the period error which appears to be an over estimate.

Table 4.5: HAT-P-20 b RPT results from fit compared to literature

Parameter	Hartman et al. (2014)	Model fit	Error from Hartman (%)
R_p/R_*	0.1284 $\pm$0.0016	0.1293 $\pm$0.0057	0.7
a/R_*	11.17 $\pm$0.29	10.85 $\pm$0.30	-2.9
T_c (BJD_{TDB}) [2458456]	0.54877 $\pm$0.00490	0.54772 $\pm$0.0014	-0.2
Inclination (Deg)	86.8$\pm$0.2	86.38 $\pm$0.30	-0.5
T14 (d)	0.0770 $\pm$0.0008	0.07589 $\pm$0.0007	-1.4
R_p (R_{Jup})	0.867 $\pm$0.033	0.893 $\pm$0.066	3.0

4.2.3 HAT-P-20 b on 2019 02 13 with JHT

The plan was to have 60 minutes of out of transit time either side of the transit with the transit too. However, due to other observing plans, the observations started 30 minutes late. There is no meridian flip. There are, however, 3 clear separate observations as the telescope had to re-position itself. The gaps are around 18 minutes long with the last gap around the predicted egress. Due to this, it is hard to fit a good transit fit to the data.

In addition the CCD temperature had a problem as it was set to $-10°$ during the observations rather than the normal level of $-20°$. This should not have affected the performance too much as the predicted dark error makes up a small amount of the total error at around 0.1%. The moon was around 56% full and up during the observations as well.

The light curve for HAT-P-20 b from the JHT is Figure 4.8. The predicted uncertainty using the target and 5 reference stars based on the targets was 2.763 ppt and the fit gave a RMS of 2.761 ppt. This is only 0.06% off the predicted uncertainty.

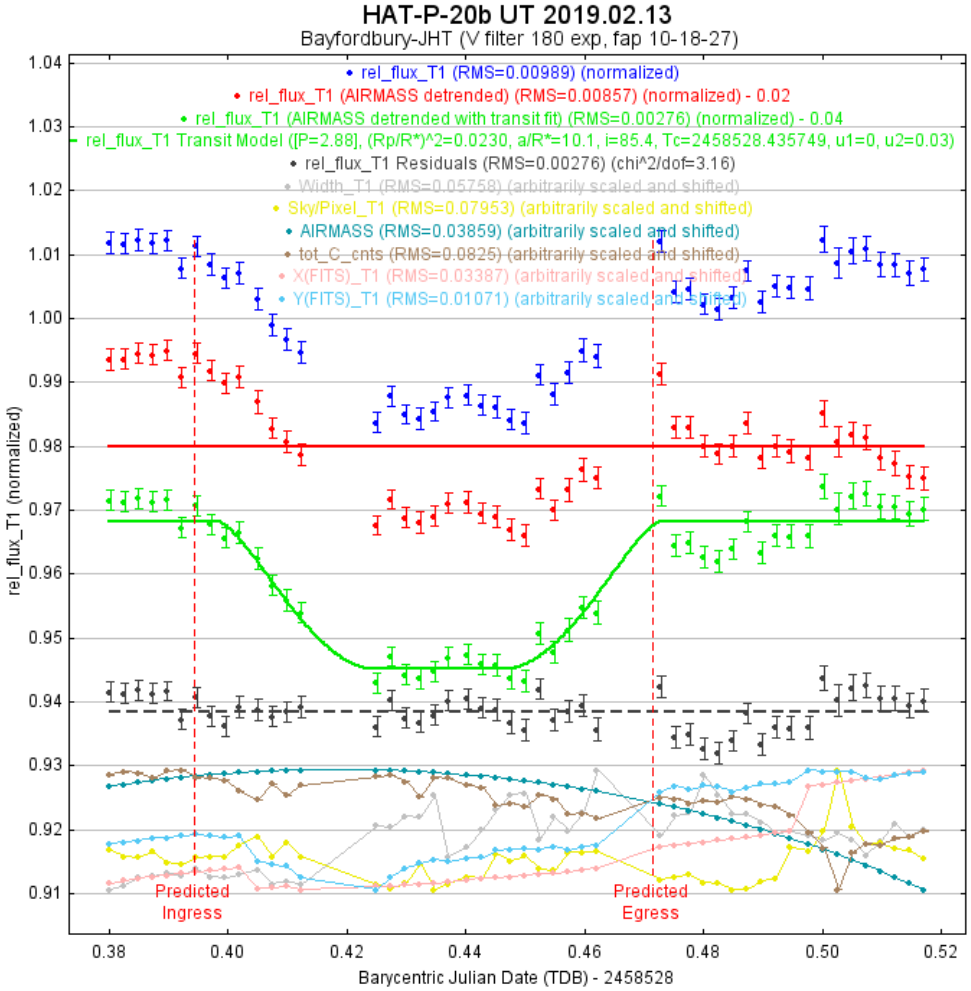

Figure 4.8: HAT-P-20 b transit fit using AIJ target then detrended by air mass, then model fit with residuals.

G. Á. Bakos et al. (2011) is the original paper that confirmed HAT-P-20 b as an exoplanet. Data from 2 of the HAT telescopes which observed it for 6 months together and 2 more follow up observations at higher precision as well were used.

The Table 4.6 shows the transit fit compared to Bakos results. It shows that the ratio of the planets and the planets radius is not well defined. This is most likely due to the telescope re-position at the ingress and egress, which makes the 3 sections harder to compare.

The transit mid-time is slightly later than predicted at around 5.6 minutes, though due to the missing egress and exposure time of 180 seconds. It is hard to know if the change in the transit mid-time is correct or also due to the poor phase coverage.

Table 4.6: Results from fit compared to Bakos.

	G. Á. Bakos et al. (2011)	Model fit	Error from Bakos (%)
$R_{\rm p}/R_*$	0.1284 ±0.0016	0.1516 ±0.008	15.3
a/R_*	11.17±0.29	10.08	-9.7
$T_{\rm c}$ $(BJD_{\rm TDB})$ [2458528]	0.43169 ±0.00501	0.4356 ±0.002	0.9
Inclination (deg)	86.8±0.2	85.40	-1.6
T14 (d)	0.0770± 0.0008	0.0748 ±0.004	-2.8
$R_{\rm p}$ $(R_{\rm Jup})$	0.867± 0.033	1.0468 ±0.086	20.8

4.2.4 KPS-1 b on 2019 05 13 with CKT

The plan was to observe KPS-1 b, 40 minutes before and continue until 40 minutes after the transit. The start was delayed for 10 minutes for an unknown reason. The RTML had started a new plan before the limit of 40 minutes after the transit, which meant it had to wait for the plan to end, so it got an extra 30 minutes.

There was a waxing gibbous (77% full) moon during the transit, above the horizon for the whole observation. There was increased sky brightness towards the end of the observation. The exposure time was selected at 240 seconds.

The predicted uncertainty using 5 reference stars of the same quality as the target (KPS-1) was 3.577 ppt over the observation. The actual RMS from the fit was 3.562 ppt which is only 0.4% off the predicted uncertainty. The light curve was then detrended by the X and Y position of the target over the observation which gives a better RMS fit of 3.159 ppt. The predicted uncertainty for the target by itself was 3.266 ppt which means it was only off by 3.4%.

The light curve for KPS-1 b is displayed in Figure 4.9. It clearly shows that the transit is later than predicted, meaning that the period of the exoplanet is likely off. Also, the transit time is not as long as thought which might be due to the missing data after the predicted egress.

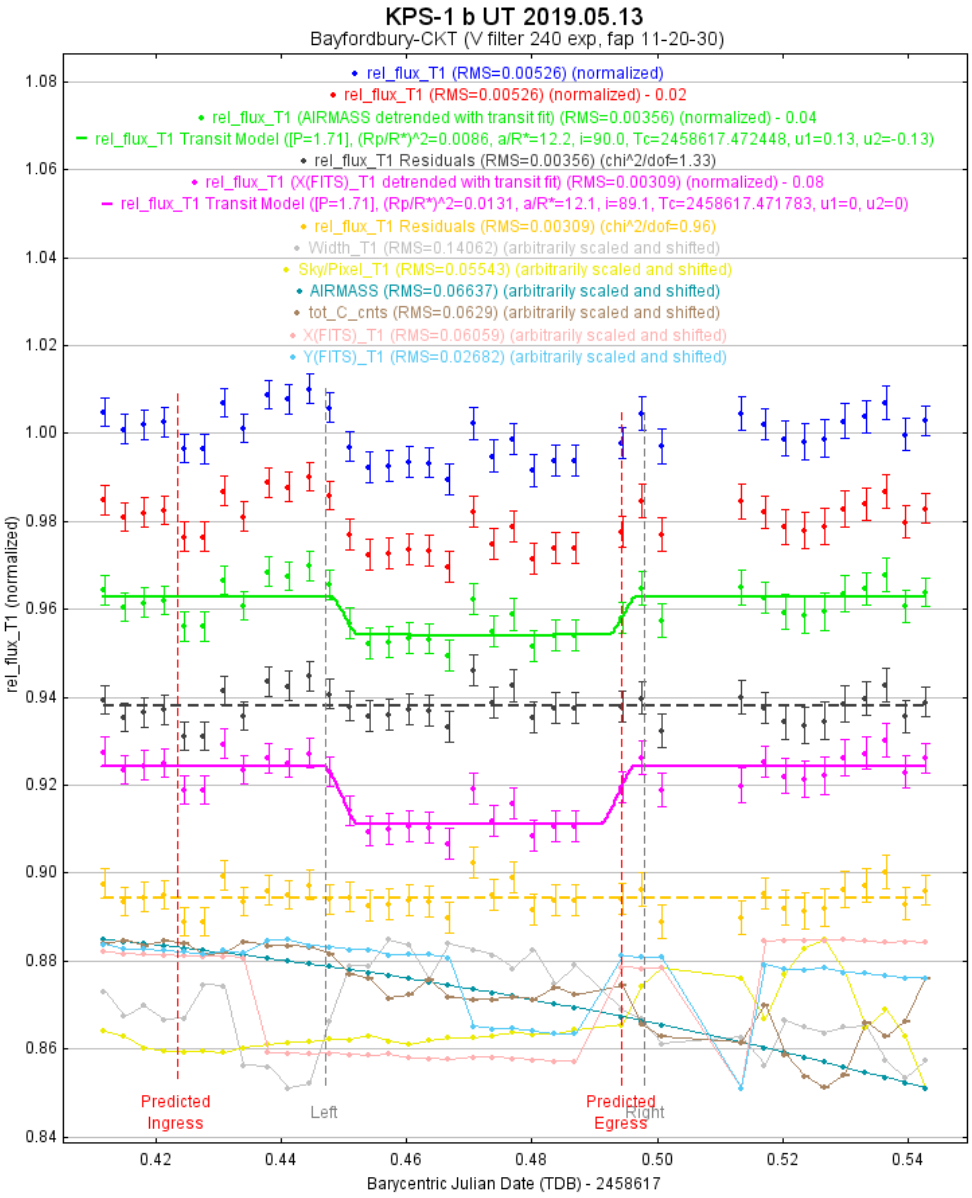

Figure 4.9: KPS-1 b light curve. Target with transit fit showing the difference between the predicted and actual ingress and egress. The plot shows raw transit data, then detrended by airmass, then the transit fit and then the residuals. Then the transit fit detrended by the x and y position of the target and then the residuals of it.

Burdanov et al. (2018) is the only paper currently that describes KPS-1 b as it is a relatively new exoplanet. It was discovered by using amateur astronomer setups to find it. They used 2 telescopes, a 1.65 metre and 1 metre telescope for follow up observations over 5 transits to get better data which was used to work out the system's parameters.

Table 4.7: Results from fits compared to Burdanov

Parameter	Burdanov et al. 2018	Model fit (Air)	Model fit (X&Y)	Error from Burdanov for Air (%)	Error from Burdanov for X&Y (%)
$R_{\rm p}/R_*$	0.1143 $\pm$0.0037	0.0927 $\pm$0.022	0.1113 $\pm$0.015	-18.9	-2.6
a/R_*	N/A	12.21	12.12	N/A	N/A
$T_{\rm c}$ ($BJD_{\rm TDB}$) [2458617]	0.45934 $\pm$0.0391	0.47245 $\pm$0.0028	0.47175 $\pm$0.0028	2.9	2.7
Inclination (Deg)	83.20 $\pm$0.90	89.99	89.99	8.2	8.2
T14 (d)	0.0700 $\pm$0.0025	0.0487 $\pm$0.0028	0.0498 $\pm$0.0028	-30.5	-28.8
$R_{\rm p}$ ($R_{\rm Jup}$)	1.03 $\pm$0.13	0.837 $\pm$0.25	1.004 $\pm$0.22	-18.8	-2.5

Table 4.7 shows the observed transit model compared to Burdanov et al. (2018). There was missing data during the egress and afterwards so the planetary parameters are rather poorly determined.

As the transit start looks like it is later than predicted, the difference in the period was calculated by working out the number of orbits between Burdanov et al. (2018) mid-transit time and the observed mid-transit time. As the transit time is not well defined, the start time of the transit has been also used with the transit duration from Burdanov to recalculate the mid-transit time.

Burdanov et al. (2018) gives the period at 1.706291 $\pm$0.000059 days where as the model fit using airmass as the detrended gives 1.706328 $\pm$0.000014 days and the X and Y detrended gives 1.706326 $\pm$0.000014 days. The new calculated periods are consistent with the period from Burdanov when the uncertainty in the period is used. This shows that the period needs to be known to a precise degree.

Figure 4.10 shows the predicted light curve data against the observed light curve data. There is a good match to the timing of the data until the different sections of the transits. The predicted data shows a deeper transit than the observed data.

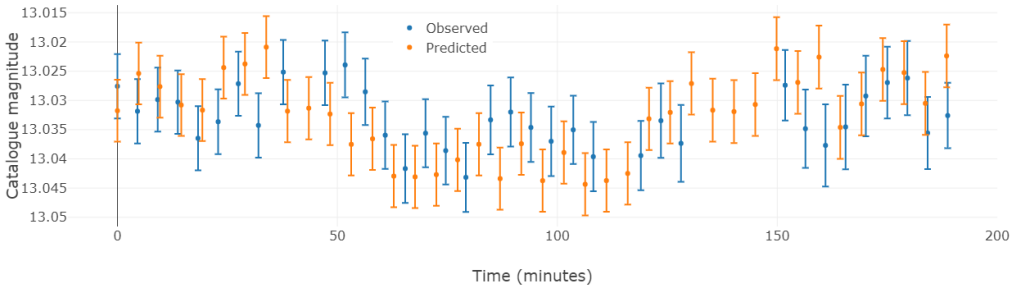

Figure 4.10: KPS 1 b transit with a predicted light curve and the observed light curve.

4.2.5 TOI 1164.01 on 2019 10 16 with CKT

Due to the poor weather at the Bayfordbury site when it was predicted to be clear, something was always attempted to be observed. So a known false positive from TESS was observed. The TOI was a false positive due to the signal coming from a nearby eclipsing binary that was 12 arc-seconds apart from the main target. The TOI gave a transit depth of 8.6 ppt.

Observing in V Filter the NEB is 1.5 magnitudes fainter than the main target in V. The plan was to start the observation 30 minutes before transit and continue until 30 minutes after the transit. However, the plan did not start until about the mid-transit time and stopped due to cloud at the predicted egress.

This was also observed by the JHT. The CKT & JHT data is able to separate the two stars but all the attempted apertures for the JHT are not able to plot the main target without the NEB star affecting the data. It was a bright moon night (91%). As this is thought to be an eclipsing binary, only the transit depth can really be compared as fits for the other observations are not available.

Paul Benni, "observed a full event on 2019 09 21 in gp and ruled out the apparent 8.6 ppt event on target but a 35 $\pm$ 4 ppt event on a star that was 12 arc-seconds away" (Benni 2020). The Gaia radius of the neighbour is $R_{\text{star}} = 2.42\ R_{\text{Sun}}$, so the companion radius is $R_{\text{c}} = 0.453 \pm 0.025\ R_{\text{Sun}}$ (Benni 2020) that would mean it was a eclipsing binary system.

The predicted uncertainty over the observation was 3.373 ppt. Figure 4.11 shows that the main target has a RMS of 3.40 ppt which would be enough to detect a 8.6 ppt transit event. The predicted uncertainty is only -0.78% off.

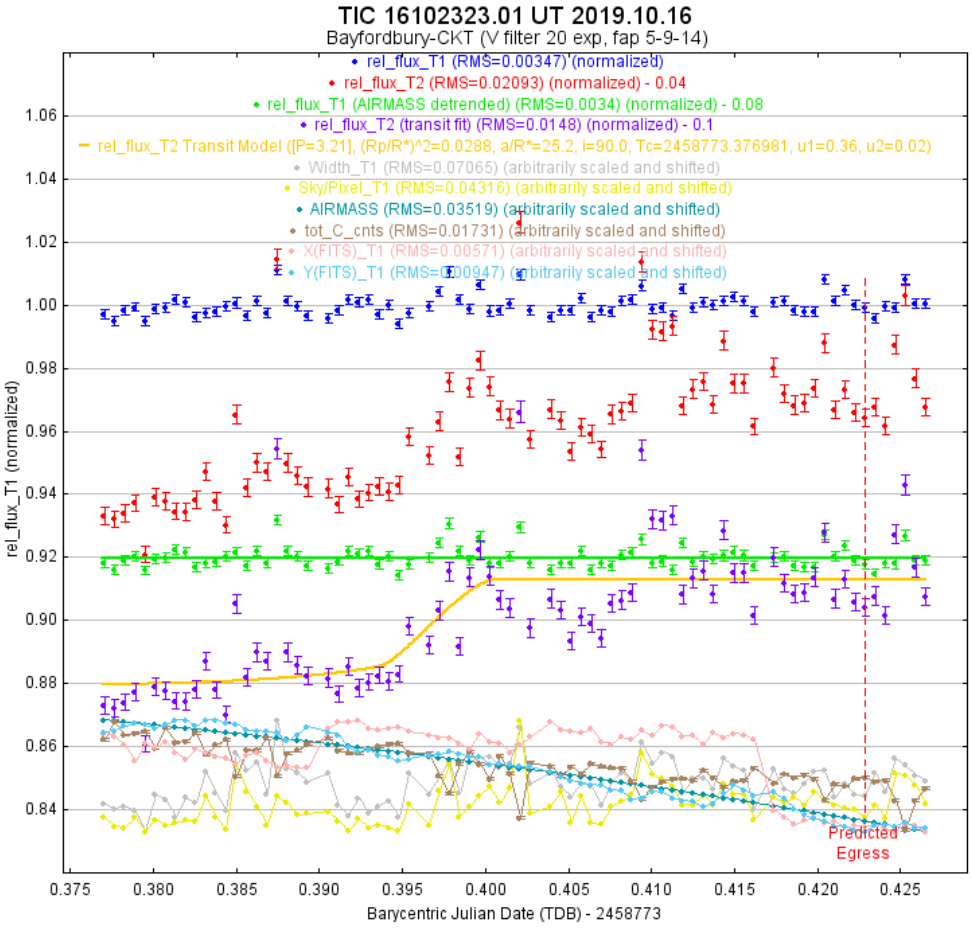

Figure 4.11: Plot of main target (T1) and the NEB (T2). Plotted normally then the target detrended by air mass and finally the fit model for the NEB not detrended.

The fit of the NEB depends on the limb darkening factors used, due to the incomplete event. The transit depth is 28.8 ± 7 mmag which means the companion would be $R_c = 0.411 \pm 0.05\ R_{Sun}$. This is only -9.3% off Paul Benni's observation and within the uncertainty error bars off each other, which is good considering that the CKT data only has less than half the transit that would be expected. This observation re-confirms that the companion is a brown dwarf or a low-mass star and not a planet.

4.2.6 TOI 1455.01 on 2019 12 01 with JHT

The goal was to start observing half an hour before the predicted transit and continue observing up to half an hour after the predicted egress. The JHT was used as it was the only telescope that could see it during the transit. As no previous follow-up had been done, it was observed in R filter as it is the closest filter that the JHT has to TESS.

The exposure time was 60 seconds. TOI 1455.01 had a reported 16.26 ppt transit depth which would be easily detected by the JHT, even though the full predicted precision could not be worked out.

Due to light clouds, the start of the observation was delayed. This meant that there was only 6/7 images before the predicted ingress. At the end of the observation there was high air mass (1.8).

The JHT had a telescope pointing problem at the start of each RTML plan. So the first image of each plan had to be removed due to the pointing error. Figure 4.12 also shows the X and Y changes. It can be seen that there is a saw tooth like pattern that emerges due to the telescope not actively tracking the target, so it drifts over the plan, then gets replaced at the start of each RTML plan. There are 5 different plans with the biggest gap between plan 3 and 4 of around 8 minutes.

There was no setup for the predicted uncertainty for the JHT in R filter. This is mainly due to not having the individual flats for the R filter. Shortly after this transit, the computers that control the telescopes at Bayfordbury went offline. Therefore the individual flats could not be recovered so there was no predicted uncertainty. The data for the fit has been binned to two to get a better RMS of 1.97 ppt versus 2.61 ppt for the un-binned data.

The Figure 4.12 shows the light curve that was produced for the TESS SG1 follow-up. It shows a transit depth of 15.06 ppt. However, as there are only a few images before the transit starts, the transit depth is very dependent on the transit fit, e.g., if air mass was not used as a detrended parameter then the transit depth dropped to around 25 ppt. The transit model fit shows a 4 minute early transit but an 11 minute longer transit. This is mainly due to the limited data before the transit.

The seeing conditions were more than expected at the start and steadily increased until just before the egress when it went constant. Expected seeing was 2-3 arc-seconds whereas it starts at around 4 and goes up to 8 arc-seconds then down to around 3.5.

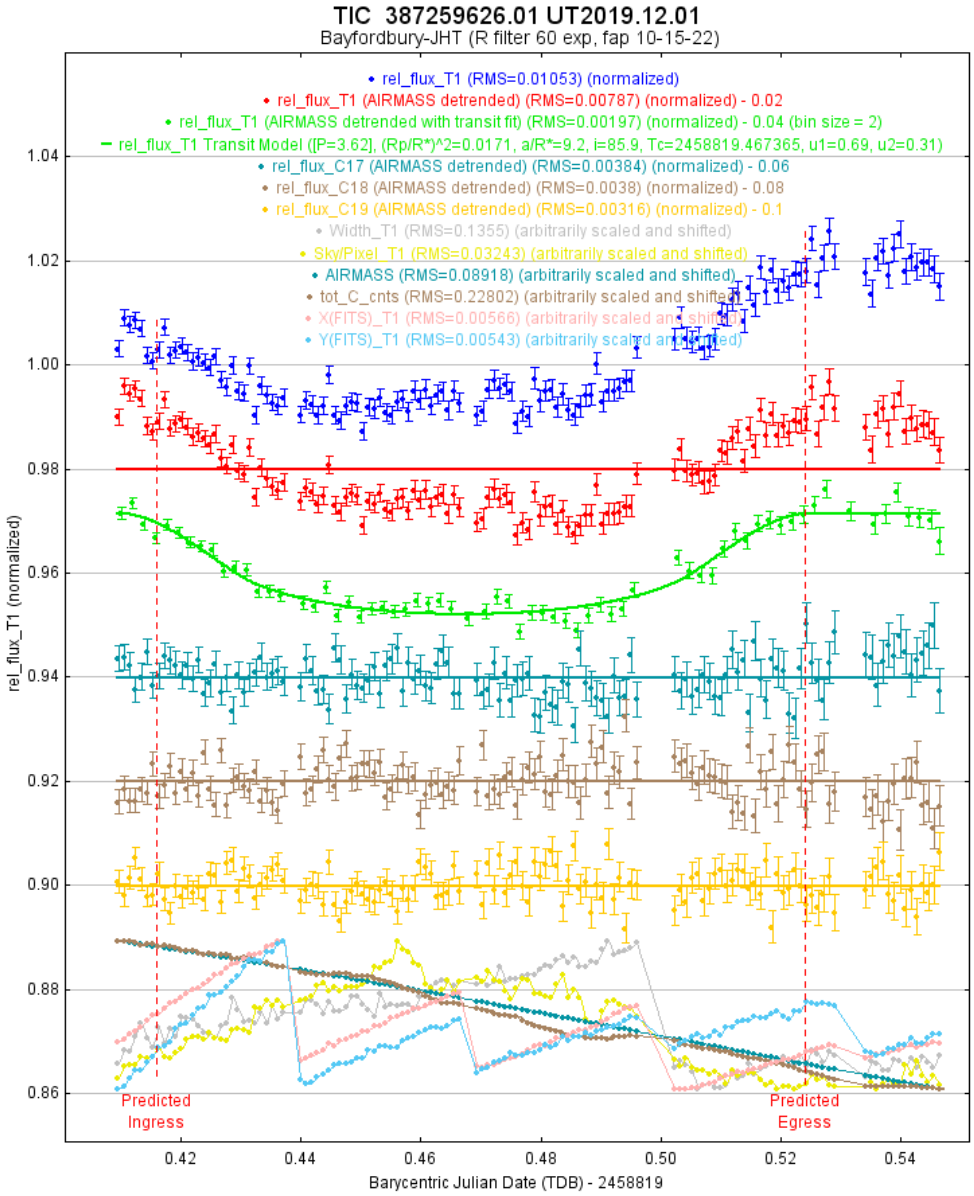

Figure 4.12: Plots of main target, original, detrended by air mass then the transit model. Along with the 3 reference stars used, as this is the light curve that was reported to ExoFOP TESS.

This shows a 1.71 R_{Jup} planet around a F5V star with a period of 3.62 days and semi major-axis of 0.051 Au. This transit was uploaded to ExoFOP TESS. However, on the 13th of December 2019, TrEs observed TOI 1455 for the second time and yielded a velocity shift of 28 km/s (Bieryla 2020). This implied a 0.245 $\pm$0.022 $M_{\odot}$ mass companion, which is an M dwarf companion rather than a Jupiter mass planet.

Due to this it was retired as an SB1 (Spectroscopic Binary - Single-lined) which is when the radial velocity measurements are too large to be caused by an orbiting planet. That means it is a false positive for an exoplanet as the measurements are too large to be caused by an orbiting planet.

4.3 PIRATE Telescope Transits

The PIRATE Telescope Transits are archive transits that were taken to see how good the predictions were. Due to this, it is not possible to state the goal for the observations.

4.3.1 WASP 12 b on 2018 01 14 with PIRATE in R

WASP-12 was observed for around 30 minutes before the transit started. Only the ingress and mid-transit of WASP 12 b was observed alone with the pre-transit due to this, it was hard to analysis the data for the transit time and depth.

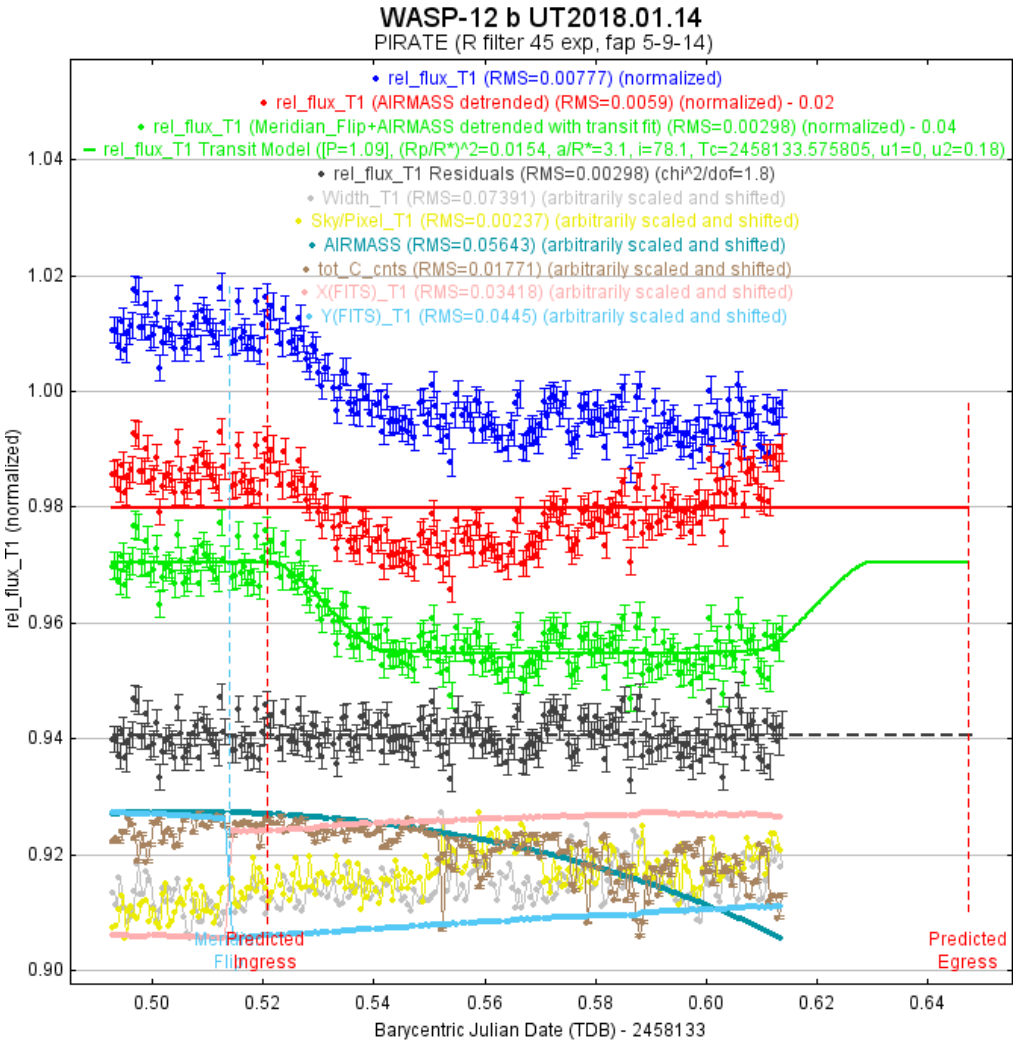

Figure 4.13: WASP-12 b transit light curve, with the raw data, detrended by airmass, the transit fit detrended by airmass and meridian flip, and then the residuals from the fit.

There is no magnitude for WASP-12 in R so this had to be calculated based on counts observed in order to get the predicted uncertainty. The predicted uncertainty was 2.960 ppt based on the full observation and magnitude of 11.45 in R. The RMS from the fit was 2.977 ppt which means the predicted uncertainty was only -0.56% off.

Figure 4.13 shows the light curves from the target. It shows that the fit has the wrong transit duration due to the lack of the data at the egress. Chakrabarty and Sengupta (2019) is the latest follow-up paper for WASP-12 b which is based on 5 transits at high precision with a 1.3 metre telescope.

The ratio of planet to the stellar radius was observed to be 0.1241±0.006. Chakrabarty and Sengupta (2019) reported it to be 0.1170 ±0.0002 based on 5 different observations. Which means that the observed is only 6% off which is very good considering it only has one off transit side. The fit gives the planet's radius of 2.04±0.15 in Jupiter radius whereas Chakrabarty and Sengupta (2019) reports 1.937± 0.056.

Figure 4.14 shows the observed data vs the predicted data. As can be seen, there is a close match between the observed and predicted data, with only a few observed data points being outside the predicted area. This is likely due to the predicted points being placed based on a maximum of 2.5 sigma of the predicted error.

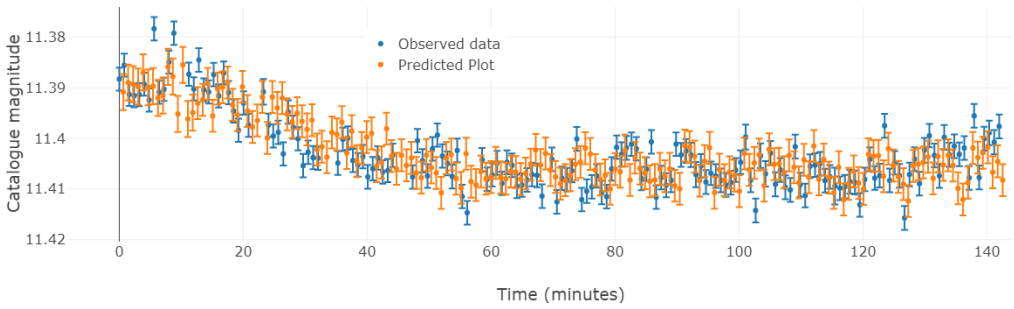

Figure 4.14: WASP 12 b transit with a predicted light curve and the observed light curve

4.3.2 HAT-P-44 b on 2018 04 26 with PIRATE in R

HAT-P-44 b was observed just before the predicted ingress until the start of the egress where no data was taken for some unknown reason. After the transit had finished, it was observed for a further 35 minutes. Figure 4.15 shows the light curve for HAT-P-44 b. There is missing data during the egress, that makes it hard to analyse the transit duration. In addition there is not much out of transit data to get a trustworthy transit depth value.

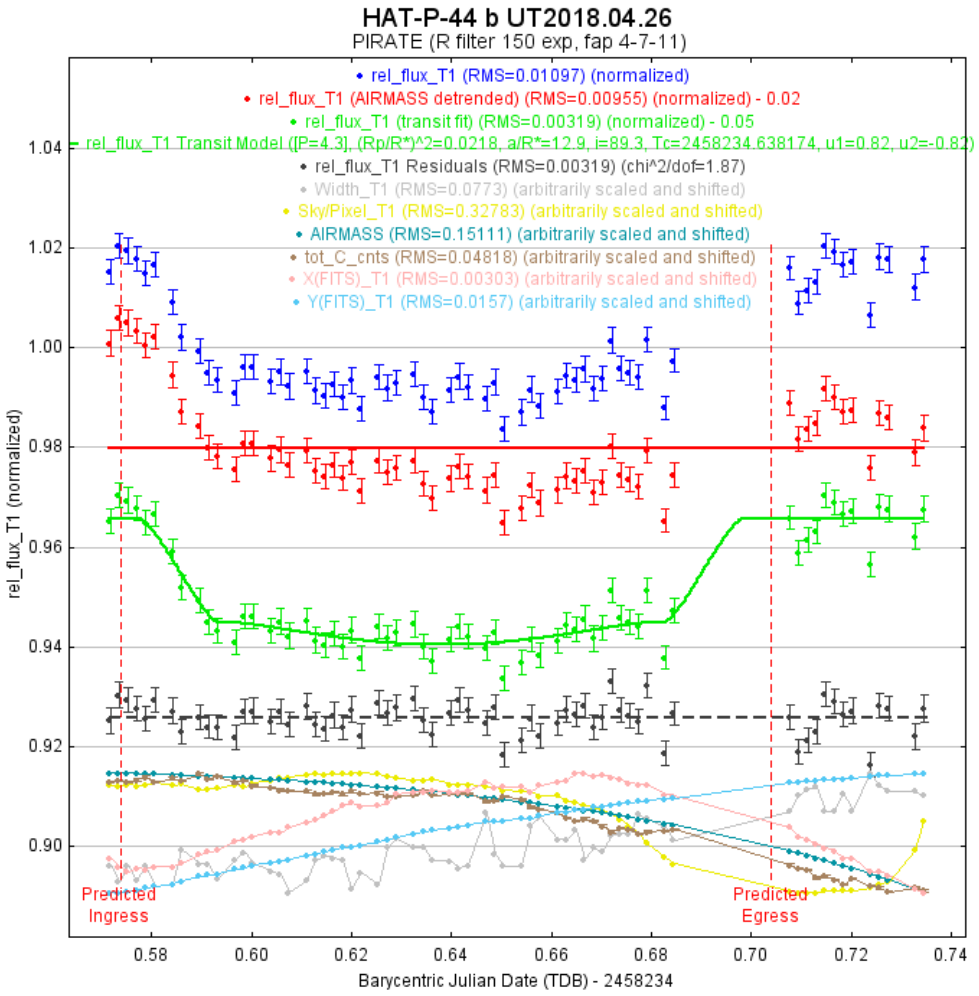

Figure 4.15: HAT-P-44 b light curve. With the raw data then detrended by airmass. Then the transit fit and then the residues from the fit.

The observed fit gave a RMS of 3.186 ppt while the predicted uncertainty was 3.219 ppt for the whole observation which means it is only off by 1.06%. There is high airmass at the end of the observation, which may impact the predicted uncertainty as it uses the average. Looking at the median airmass, the predicted uncertainty becomes 3.194 ppt so only 0.26% away.

Figure 4.16 shows the predicted data for Hat-P-44b compared to the observed data. It shows that the post-out of transit data is a lot higher than the predicted data. The mid-transit depth has been used to place the y axis for the predicted data due to the missing data.

Hartman et al. (2014) is the original paper that declared HAT-P-44 b as an exoplanet. It is the only paper that has the 6 system parameters that are being compared in this paper. The system parameters are based on 2 campaigns from the HAT system each lasting about 3 months with one telescope on each campaign as well as 4 high precise follow-up observations.

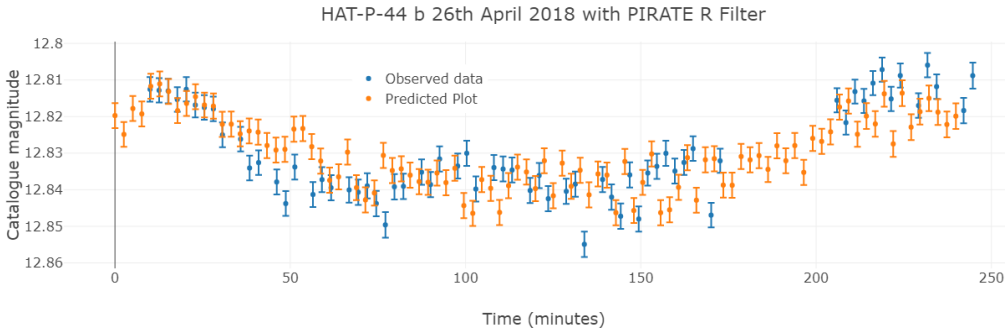

Figure 4.16: HAT-P-44 b transit with a predicted light curve and the observed light curve

Table 4.8 shows the results from the transit fit compared to Hartman. It confirms that the transit time is not well formed due to the missing data around the egress. The ratio of the radii is higher than Hartman, which is mostly due to the little amount of pre-transit data. This means that AIJ has not got a good out of transit measurement.

Table 4.8: Hat-p-44b results table compared to Hartman

Parameter	Hartman et al. 2014	Model fit	Error from Hartman for (%)
R_p/R_*	0.1343 $\pm$0.0010	0.1477 $\pm$0.011	9.9
a/R_*	11.49 $\pm$ 0.8	12.87	12
T_c (BJD_{TDB}) [2458234]	0.65616 $\pm$0.01145	0.63817 $\pm$0.0018	-2.8
Inclination (Deg)	89.1 $\pm$0.4	89.26	0.2
T14 (d)	0.1302 $\pm$0.0008	0.1209 $\pm$0.0018	-7.2
R_p (R_{Jup})	1.242 $\pm$0.1	1.395 $\pm$0.22	12.3

4.4 1x1 or 2x2 Binning

This subsection will look at the analyses of data from PIRATE, comparing the predicted uncertainty over two different binning options that PIRATE uses. Selecting the right binning is important to get the right readout time, field of view and uncertainty.

CCD cameras often have different gains at different binning options. The PIRATE reports the same gain (1.39 e-/ADU) on each 1x1 and 2x2 binning. This means that in theory they should have the same instrument magnitude versus catalogue magnitude profile.

By increasing the binning option, the readout time decreases (Romanishin 2006), for PIRATE the readout time works out to be 4.1 and 3.1 seconds for 1x1 and 2x2 respectively. This is due to fewer data points (pixels) needing to be read out.

This analysis of different binning options could only be done for the Open University PIRATE telescope, as it has a large archived database, which contains images in both 1x1 binning and 2x2 binning. Bayfordbury does not have a large archive for images that are not in 2x2 binning, so this analysis could not happen for Bayfordbury.

4.4.1 PIRATE calibrations

This was done by calibrating 3 filters, R, V and B for PIRATE in the two different binning options, as described in section 3.1.2 and the website tool. These three filters were used as they have a large set of known catalogue magnitudes. The first part of this was to analyse the calibration files, starting with the bias and dark.

Table 4.9 shows the breakdown of the Bias and Dark noise values for the predicted precision. This shows the results from 2 sets of calibrations. The bias noise is the mean of the SD from 10 bias images. The dark is the mean of the SD from 9 dark images, which have a 60 second exposure time. The dark noise is then calculated by removing the bias noise value and then dividing it by the exposure time of the dark.

Table 4.9: Bias and Dark calibration analysis

	1x1 Binning			2x2 Binning		
	Set 1	Set 2	Mean	Set 1	Set 2	Mean
Bias (ADU)	8.593	8.661	8.627	10.999	11.085	11.042
Dark (ADU)	9.020	9.015	9.017	14.511	14.581	14.546
Dark noise (ADU/s)	0.0071	0.0059	0.0065	0.0585	0.0583	0.0584

As PIRATE uses twilight flats, there are stars that appear in the flat field images. This affected the quality of the flats. The flat noise value for the predicted precision was calculated, due to the stars that appeared in the individual flats, but not in the master. The flat noise value was around an order of magnitude off, the expected value (0.0394 vs ~ 0.002). A flat noise value of 0.0394 would give a minimum predicted uncertainty of around 30 ppt, which is too high.

The image created as part of the calculation for the flat noise was analysed. It shows the SD for each pixel location from the individual flats. The stars could easily be seen on this image, as they were around 100 times the background level. As the flat noise value uses the SD of this image, this would completely affect the value calculated.

So a clipping method was used to remove the stars from the images, before making the master. AIJ has an outlier program that was used to remove the stars and replace the values. The SD image produced still showed the stars, but the core of the stars have been removed and flattened. This was the cause of the SD increasing by so much.

Table 4.10: Flat calibration analysis for clipping

Images	Type	Set	SD	Local SD (60 pix)
5	Raw	a	0.033994	0.002775
		b	0.043444	0.003264
		Mean	0.038719	0.003020
	Cliped	a	0.003080	0.002691
		b	0.003463	0.002866
		Mean	0.003272	0.002779
10	Raw	a	0.037311	0.002137
		b	0.041500	0.002198
		Mean	0.039406	0.002168
	Cliped	a	0.002351	0.002092
		b	0.002556	0.001976
		Mean	0.002454	0.002034

Rather than the overall SD from the image, a local SD value was used, based upon a 60 pixels aperture where no stars could be seen. Table 4.10 compares the overall SD and the local SD over 5 and 10 images from 2 different sets of flats. Then the mean of the 2 sets. In addition it compares the SD and the local SD from the raw flats and clipped flats. This is only for the R filter in 2x2 binning.

This shows that without the clipping program, the flat noise value increases by up to more than 10 times than is to be expected by the local SD. It also shows that increasing the number of flats from 5 to 10 images decreases the SD by around 34%.

This process was then completed for the B and V filters, as well as over 1x1 binning. Table 4.11 shows the calculated flat noise value, for the 3 different filters in the 2 different binning options and for the 5 and 10 image sets. The table shows there is an increasing flat noise when comparing B to V and V to R. This is higher than expected from just the change in filters.

Table 4.11: Flat calibration analysis

	B (10^{-3})	V (10^{-3})	R (10^{-3})
1x1 Binning (5)	1.361	1.769	2.993
1x1 Binning (10)	1.014	1.311	2.067
2x2 Binning (5)	1.408	2.449	2.779
2x2 Binning (10)	1.065	1.876	2.034

4.4.2 Flat Problems

The flat noise value that was calculated for B, V and R filters, showed that the R filter was twice the B value. This is likely due to a low-signal to noise rather than a filter difference, as the mean count of the R flats were 8,000 ADU, whereas in B filter was around 30,000 ADU for the 2x2 binning. As PIRATE uses twilight flats, the time that the flats are taken has a huge impact on the counts.

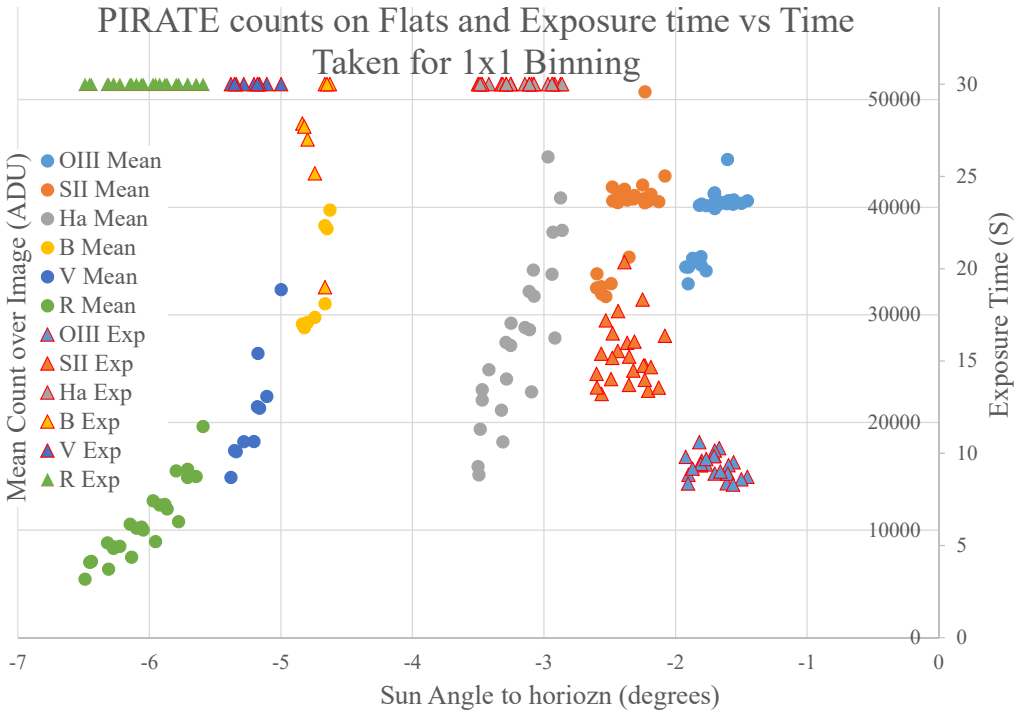

Figure 4.17: Mean Counts (circles) and exposure time (triangle) per flat for each filter for 1x1 binning with respect to the Sun angle at the time of mid-exposure time.

The flats are taken over a period of 4 different twilights, where 1x1 binning option is taken in the morning and 2x2 in the evening. Then over alternating nights the filters change from OIII, SII, Ha, U, I, Lum to OIII, SII, Ha, B, V, R. As the previous work above has worked on B, V and R filters, only these nights were analysed here.

To compare different flats that were taken during different twilights, the angle of the Sun was used at the mid-exposure time of the image being taken, in order to counteract the changing brightness of the Sun over different days. PIRATE has a maximum exposure time for flats of 30 seconds in order to stop one image or filter taking too much time.

Figure 4.17 and Figure 4.18 show the results divided up by 1x1 and 2x2 respectively. The mean count from the flat and exposure time that was used has been plotted for each filter against the Sun angle. The triangles refer to the exposure time of the flat image and the circles refer to the mean count in ADU of that flat. The data shown is for 2 weeks' worth of flats, that were taken with the pattern of OIII, SII, Ha, B, V and R.

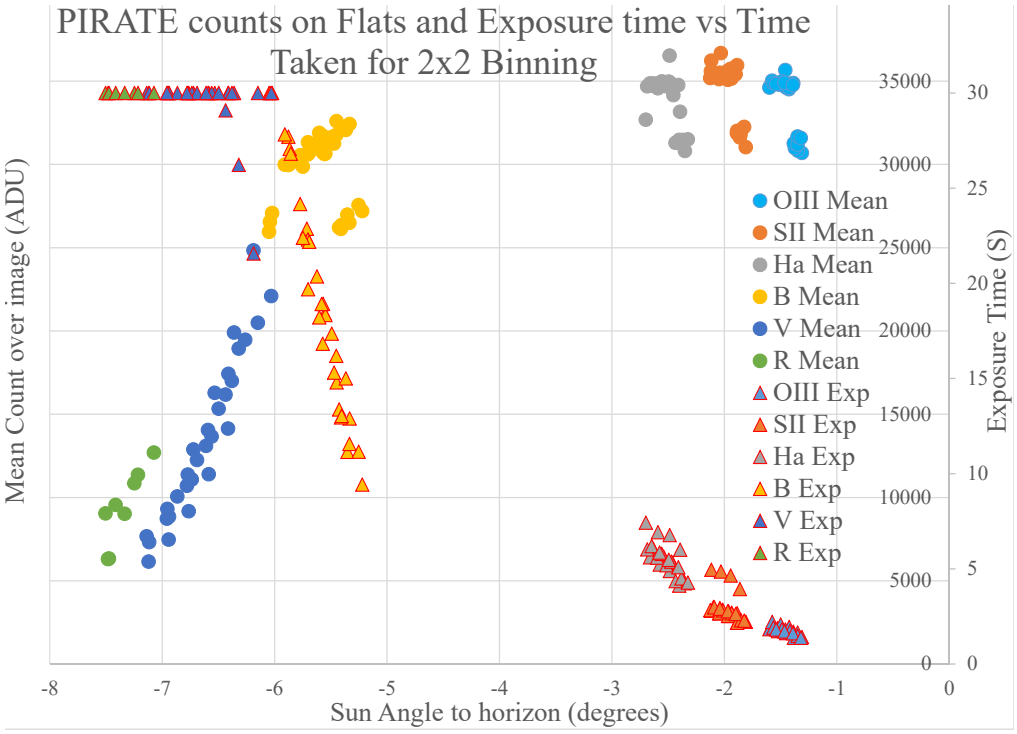

Figure 4.18: Mean Counts (circles) and exposure time (triangle) per flat for each filter for 2x2 binning with respect to the Sun angle at the time of mid-exposure time.

In both binning options the R and V filters, have an under count in terms of the wanted overall mean count of around 35,000 ADU, due to the exposure time of 30 seconds and the Sun angle used. This shows that the calculated flat noise values in table 4.11 is caused by a low signal to noise, rather than a filter difference.

Short exposure (0.05 and 1.5 seconds) flats were also taken, to show the shutter movement pattern. These flats have been removed from the plots. Looking at the OIII 2x2 images with very short exposure times of around 1.5 seconds, they show slight shutter effects on the images, as the exposure time is too short.

4.4.3 Instrument vs Catalogue Magnitude

The next part was to work out the Instrument Magnitude versus Catalogue Magnitude plot for each filter and binning separately. This should not be impacted by the flat field problems, apart from the increased uncertainty due to them. As can be seen in the Figure 4.19, the line of fit for the R filter and 2x2 binning does not appear to be affected.

Using the equation from the line of fit to re-calculate the instrument magnitude from the catalogue magnitude, it shows an SD of 0.26 magnitudes, which is higher than P. J. Beck (2018) found at 0.195 magnitudes for the CKT in V. This means that the fit is not as good as P. J. Beck (2018) but still valid.

This was then repeated for B, V and R filters over the different binning options. The PIRATE archives did not contain enough 2x2 images in B to create a good fit. Table 4.12 shows the gradient and bias from the line of fits for the different filters and binning options.

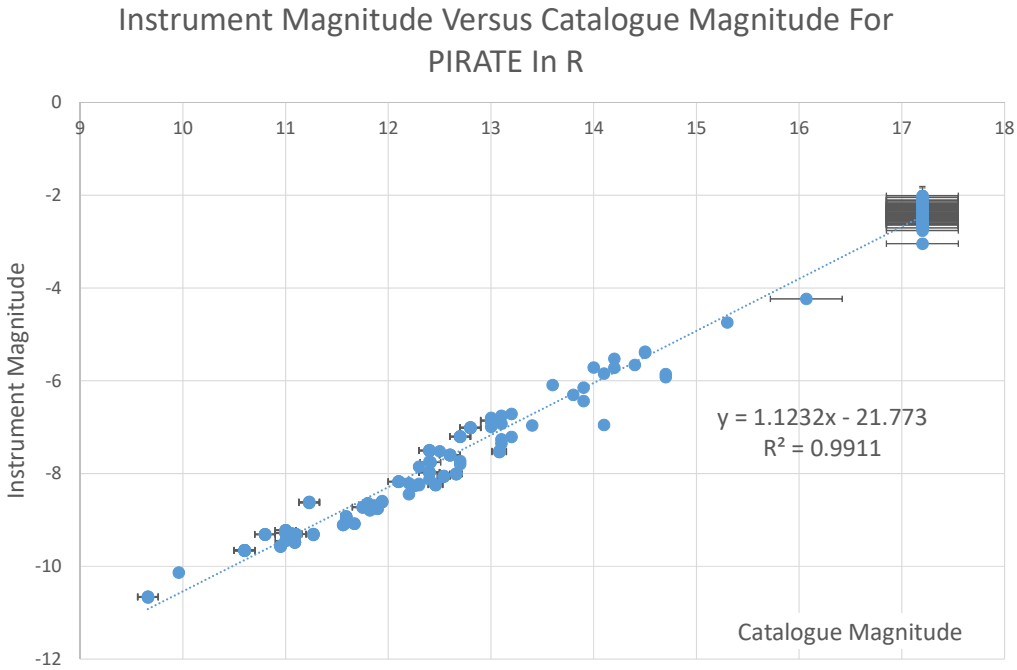

Figure 4.19: Instrument Magnitude $m'_{t=1s,X=1.0}$ for an air mass of 1 and a exposure time of 1 second versus the known catalogue magnitude for each star.

Table 4.12: Instrument Magnitude versus Catalogue Magnitude Filter versus Binning

Binning	B	V	R
1x1	0.9956,-20.146	1.0911, -21.144	1.0810, -21.218
2x2	N/A	0.9503, -19.759	1.1232, -21.773

PIRATE reports the same gain for the different binning options. There appears to be a difference between them based on the instrument versus catalogue magnitude of the 1x1 binning versus the 2x2. This would suggest that they have a different gain value. Using Steve Howell (2000) book and Gary (2007), the gain for each binning was manually calculated based on the flats and bias.

This analyses found that the 1x1 binning had a gain of around 0.975±0.065 (e-/ADU) and 2x2 had 1.38±0.02 (e-/ADU). The ratio of the gains was calculated based on the instrument versus catalogue magnitude from the R and V values. This worked out to be around 0.60 and 0.71 respectively which is close to the ratio of the calculated gain of 0.70±0.06. This shows that there is a gain difference between the different binning options, which affects which binning option is suited for different targets.

4.4.4 1x1 vs 2x2 Binning

As the predicted precision had been worked out for 2 different binning options, they could be compared over different magnitudes and exposure times. This has been done only for the R filter as it had the best fit.

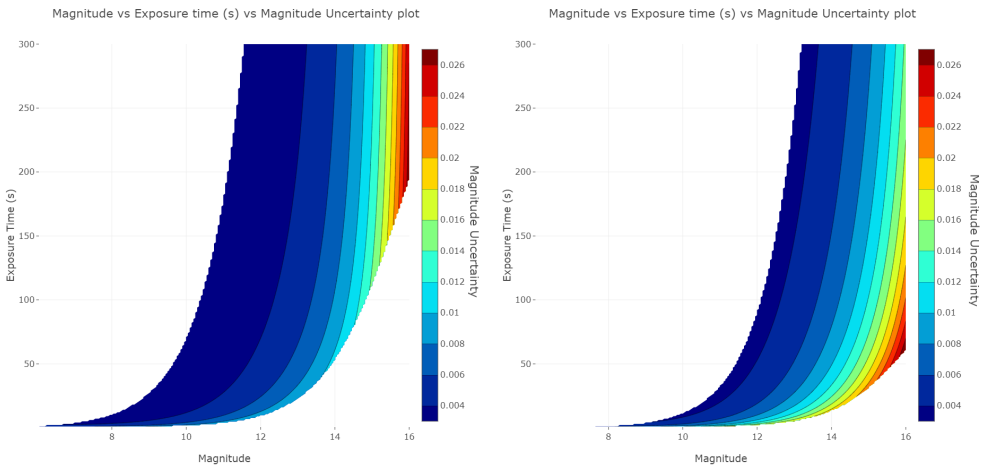

Figure 4.20: Magnitude uncertainty plot over different magnitudes and exposure time for the R filter. Showing the different uncertainties for the different binning options for an airmass of 1. Left: 1x1 binning, Right: 2x2 binning

Figure 4.20 and figure 4.21 are created by a tool on the transit follow up tool website. It maps out the predicted precision over different exposure time and magnitude. There are 2 section that are left empty as no actual performance expected there. The top left section is due to the star hitting the linearity limit so no actual performance. The bottom right is removed when the sky background count per pixel is half the predicted peak pixel value.

Figure 4.20 shows the 1x1 (left) and 2x2 (right) binning magnitude uncertainty plots over different catalogue magnitudes and exposure times. It shows that the 1x1 has better performance at very bright magnitudes where 2x2 has no predicted performance and that 2x2 can see better at fainter magnitudes.

For example at 200 seconds and 16 magnitude 1x1 binning has around 24 mmag magnitude uncertainty verses 18 mmag for the 2x2 binning. At 50 seconds and 14 magnitude 1x1 binning has around 10 mmag magnitude uncertainty verses around 9 mmag for the 2x2 binning.

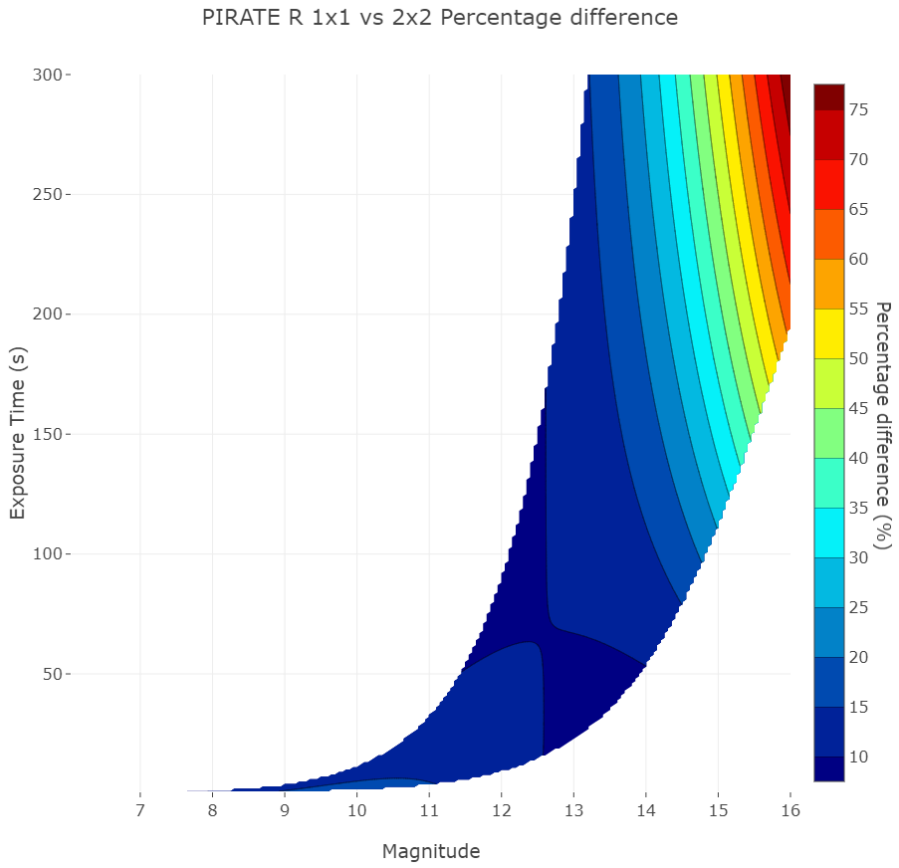

Figure 4.21: Percentage improvement of the predicted uncertainty for R 2x2 binning verses 1x1.

In order to compare them directly, the same exposure and catalogue magnitude has been used for each. Figure 4.21 shows the percentage improvement that going from 1x1 to 2x2 binning has, where they both have a predicted performance in the R filter. This is based on the current flats, so the values would likely change when the flats improve.

This shows that the 1x1 binning is better at short exposure times on bright targets, where the star on the 2x2 binning would be saturated. But the 2x2 binning is better everywhere else assuming the same exposure time. This is for the assumed seeing of 2 arcseconds.

For example a magnitude 8 star, at airmass of one on the 2x2 would only have an exposure time of 1 second, which gives a predicted uncertainty of 5.86 mmag. The 1x1 binning would have up to 10 seconds of exposure time before being saturated. If an exposure time of 2 seconds was used the uncertainty would be 4.84 mmag. However, due to the increased exposure time and readout time for the 1x1 binning, there would be around a third less images than with the 2x2 binning.

5 Discussion

In general, the observed data transit fits, for the confirmed exoplanets do achieve agreement with the literature with a few exceptions. The exceptions are where there is missing data around the transit or little off-transit data to get a good transit fit model. This can be seen for the case of TOI 1455 as it has only a small amount of data before the beginning of the transit, so the transit depth can move more than 10 ppt.

For the TESS transits that have been looked at, two of them (TOI 689.01 and 1164.01) are false positives due to having nearby eclipsing binaries. The other 2, TOI 516.01 and 1455.01, have observed transits. However, the follow-up radial velocity showed that they were both spectroscopic binaries.

The transits that have been observed by PIRATE, WASP-12 b and HAT-P-44 b are hard to fit exactly due to one being a partial and the other missing data during the egress respectively.

For the Bayfordbury telescopes, the transit observations can be hard to fit too, due to missing data areas. This is mostly due to bad weather and the change of a RTML plan, which controls the telescope.

KPS-1 b is the only confirmed exoplanet transit that has a significant shift in the mid-transit time. However, this is not due to another planet but due to the period not being accurate enough. None of the other observed exoplanets show any significant evidence of TTV. However, since the uncertainty in the predicted mid-transit time can be in the order of a few minutes, it can be hard to distinguish small changes in the period.

The mid-transit uncertainties that have been achieved of around 2 minutes shows the ability to distinguish TTVs on the order of a few minutes or less. This means that unknown exoplanets could be found but exomoons would not be.

Bayfordbury has observed HAT-P-20 b twice in the past 2 years with different telescopes. It has also been observed 6 other times over the last 4 years. The data could be folded to give better parameters, especially the ratio of the radii of the planet and star.

There were problems that cannot be helped during this work;

- Power outages at the telescope site.

- Wild fires near the telescope. The TRT Sierra Remote Observatories (SRO) was closed due to wild fires in California in late October 2019[1] and the lost power for about a month afterwards.
- Other plans on the telescopes that blocked the telescopes schedules.
- The computer that controlled the telescope crashed.

5.1 RMS of fit vs Predicted uncertainty

The difference between the predicted uncertainty and the observed RMS is on average only 0.027 ppt or 27 parts per million (ppm) off, from the transit fits that have been recorded in this work. It is also with one exception within one percent of the achieved RMS. The exception is for TOI 689.01 on the SBO, which probably arises from the flat fielding problem.

There is no easy way to calculate what the uncertainty is in the predicted uncertainty. However, looking at the airmass and magnitude, a change in the airmass of 0.05 gives a difference of around 30 ppm, while a magnitude change of 0.05, perhaps caused by activity, gives a difference of around 20 ppm. Both of them would lead to an uncertainty of around 36 ppm.

The values change for the airmass and magnitude both depend on the system setup and magnitude of star relative to the observational equipment. There are also changes in the sky condition which would affect how accurate the predicted uncertainty is. The error from the sky as a proportion of the rest was very low (<5%) apart from TOI 516.01 due to it being an 18.5 magnitude star in the filter being used so the delta to sky was around 1 magnitude.

5.1.1 Binned data

The previous observations for transits at Bayfordbury used longer exposure times in order to maximize the signal to noise ratio. This means that there were less data points than a shorter exposure time would have given. This was partly because the analysis tool that was used before could not automatically bin data, so it was done manually.

WASP-52 b is the only transit that was observed for which binning the data down made sense as it was a near complete transit with data either side of the transit. TOI 1455.01 was also binned, but does not have a predicted uncertainty due to not being able to get the individual calibration images.

[1] https://www.bbc.co.uk/news/world-us-canada-50229657

Table 5.1: RMS and Predicted uncertainty compared for WASP-52b binned and not

	RMS from Fit (ppt)	Predicted uncertainty (ppt)	Percentage error (%)
Bin 1	4.275	4.306	0.72
Bin 2	3.082	3.045	-1.20

Table 5.1 shows the RMS and predicted uncertainty for WASP-52 b for the data that was not binned and which was by 2. The non-binned prediction gives an over estimate, whereas the binned prediction gives a under estimate. The difference is because the prediction uses the theoretical maximum that can be achieved when binning to that degree.

This shows the benefit of binning data down as, the predicted uncertainty for WASP-52b using a 120 second exposure time is 3.322 ppt. That is the exposure time for the CKT WASP-52b data doubled to what the effective binned data exposure time is. The predicted uncertainty is higher for the 120 second exposure time than the binned data using the shorter exposure time.

This shows that lowering the exposure time, so that more images are collected, and binning the data down, would end up getting a better precision than just increasing the exposure time. The predicted uncertainty for the binned data is still within the expected error from the un-binned data, but it is only one data point. This means it is hard to generalize until more data like this is available.

5.1.2 Problems with predicted precision

One of the problems with the predicted precision, is that a telescope has to be calibrated correctly before it can be used. This can be a problem for filters that have a smaller collection of standard stars with a known catalogue magnitude than other filters, as it takes more images to get a good instrument versus catalogue magnitudes plot.

For example, of the confirmed planets, there are 1,595 that have a V filter value and only 199 which have an R filter value. This means that the V filter has around 8 times more stars than R filter. This is only an estimate but shows the problem.

This can also be a problem even when the predicted precision has been correctly calculated for the setup. If the star does not have a known magnitude in the filter that is going to be observed in, there is no predicted precision because the predicted total counts cannot be predicted. There are different ways around this that have been found.

An educated estimate for the magnitude can be worked out by looking at the magnitude in other filters and looking at the spectral type of the star. Another way is to get images beforehand and input the total counts into the predicted uncertainty model. Alternatively if only the transit images are available, then the total counts from the target can be used to work out the catalogue magnitude. This is what happened for the Pirate transits and TOI 516.01.

5.2 Telescope sites

Three different telescope sites/networks are used for this work, they are discussed separately to show the information learnt about the each one.

5.2.1 Bayfordbury

No modelling was performed for where the TOIs were likely to be and what effect that would have on observing them at Bayfordbury. However, as each telescope at Bayfordbury use a different equatorial mount, it affects where each of them can look. It was only noted that the TOIs would be closer to the celestial pole due to TESS looking at the pole over the entire year.

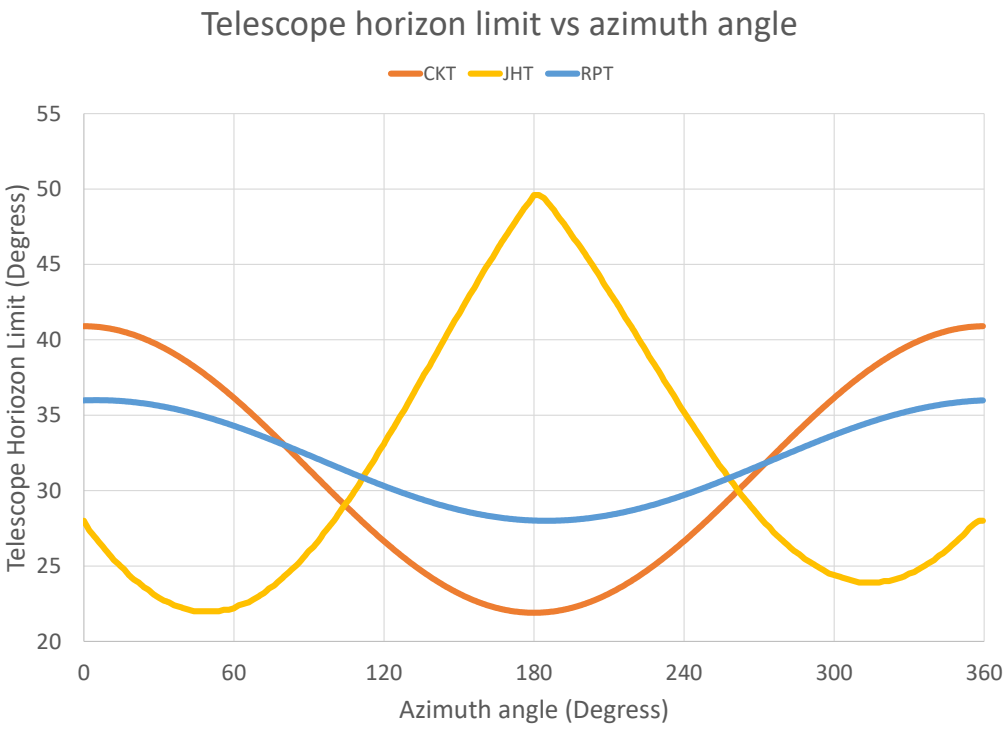

Figure 5.1: Plot showing the horizon limits for the different Bayfordbury telescopes over the azimuth.

It turned out that due to the different telescope mounts at Bayfordbury, only the JHT could see most of the newly released TOI for the full transit duration. The CKT and JHT could observe them but not for the whole transit observation. This is due to the newly released TOIs having an azimuth of around 270-360 for the first month and are normally low in the sky due to how TESS observes outwards but by time it gets released it is behind the Earth's orbit.

Figure 5.1 shows the horizon limits for the different telescopes at Bayfordbury due to using equatorial mounts. It can be seen that the JHT has the right drop for TESS at around 310 degrees rather than the CKT. But later on the older TOIs could be seen with the CKT and not the JHT.

The Bayfordbury telescopes used to have a time separation of around 50 seconds between images due to having to readout the image then calibrate it and plate solve it before the next image could be taken. This impacted the choice of exposure time that was used. The image processing system was updated to get around 21 seconds between images by changing the way the plate solving system was used. This means that shorter exposure times could now be used. Before this, the time difference between images would have been longer than looking at the target for short exposure times (10-30 seconds).

WASP-59b was observed by the CKT on the 10th of August 2018 but due to telescope maintenance over the summer the telescope had been moved so the positioning was out. All the images were around 1.2 degrees off from the target star. Which meant the star could not be seen in the images. So could not be analysed.

5.2.2 Thai Robotic Telescopes

The Thai Robotic Telescope network has 3 separate sites. This work has used SBO and SRO. There have been problems with the calibration images not being taken, which meant most of the data was unreliable. This is mostly due to flat field images not being taken. If they were, then the signal to noise of them were a problem.

It was found that when the flat field images should have been taken the telescope dome was still closed. The problem with the signal to noise of the flats was due to them being taken while the sky was still dark. The angle of the Sun when the flats were obtained was around -12 degrees, which for the exposure times of around 3 seconds meant the counts from the sky were too low (5,000 ADU).

The aim was to use the Thai Robotic Telescope network to look for TOIs due to having two separate sites that could together cover most of the TOIs. First the SBO was used as it is located in Australia, so could see the TOIs from the first year of TESS during which it scanned the southen sky. Then the SRO could be used for the second year of TESS when it scanned the north, as it is located in North America.

The aim was not achieved due to the problems with the flats, which led to a large predicted uncertainty that would not be helpful for any observations of the possible TOIs.

NGTS-6 b was observed by the SBO. However, weather stopped images being taken during the actual transit. There were images obtained before the transit and after the transit though not during the transit itself.

TOI-1194.01 was observed by SRO on the 31st of December 2019, but no flat field calibration images were produced. There were no flat field images in the filter that was used or in the archive that was available. Therefore the data was unreliable as it had too much noise to see the transit that had been observed by others.

5.2.3 PIRATE

The PIRATE telescope was the only network from which no new transits were obtained. This is in part due to the analyses of flat field images that left only the winter of 2019, at the PIRATE site. That is the most varied weather of the year, so getting a clear night that had a good TOI to go for was not achievable.

Looking back at the PIRATE transits that were analysed above from 2018. The R 2x2 flats had a flat noise value of 0.864×10^{-3} for 10 images. This is a significant difference from the current flats at around 2.034×10^{-3}. This is likely due to the change of flats acquisition, as the exposure times for the 2018 flats are around 3 seconds and the mean counts are around 40,000 ADU.

This suggests that improving the flat field images would lead to a reduction of the uncertainty, using the flat noise value from 2018 of 0.864×10^{-3}. The improvement works out to be around 5-20% depending on the exposure time, catalogue magnitude and other error factors with an average performance improvement of around 6.8% with a SD of 6.4%. For example, for a 12 magnitude star the uncertainty would go from 3.377 mmag to 2.725 mmag producing an improvement of 19.3%.

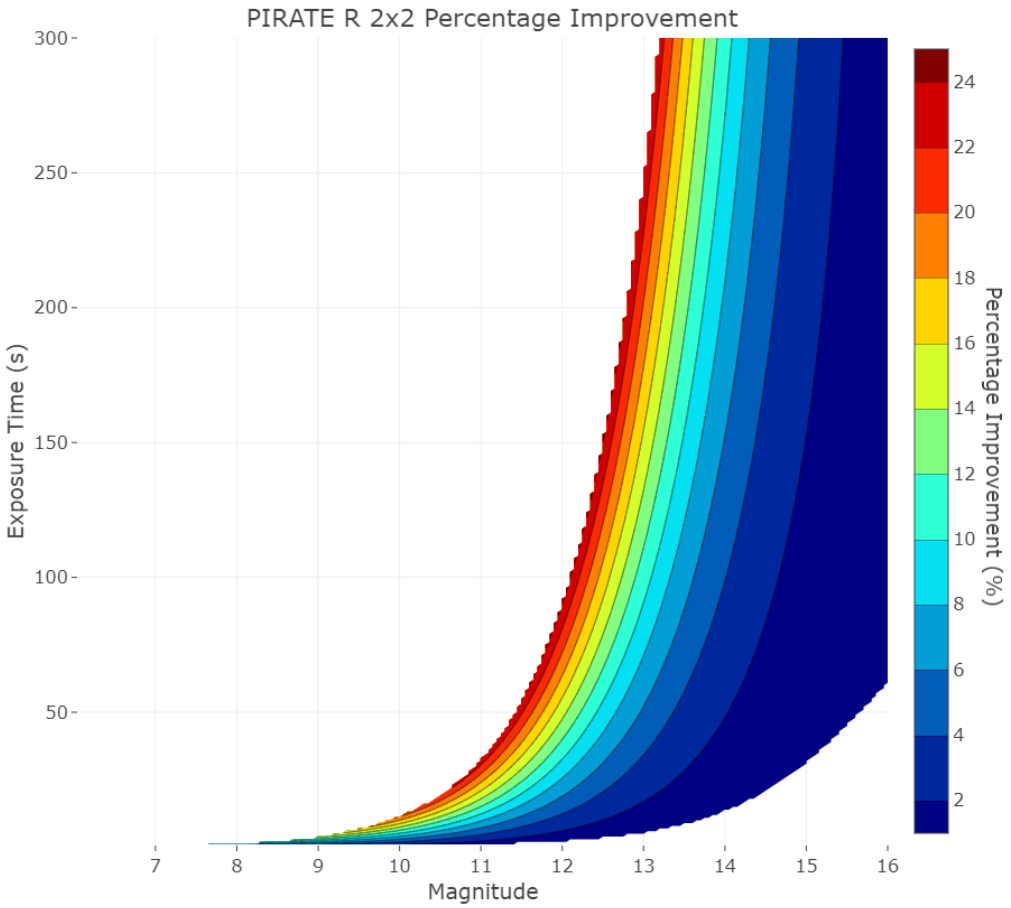

Figure 5.2: Percentage improvement for the PIRATE in R 2x2, assuming the flats go back to where they were in 2018. Only for magnitudes and exposure times that are valid based on the linearity limit and the expected seeing.

Figure 5.2 shows the percentage improvement over different magnitudes and exposure times, which would be expected if the flats went back to the old value. It is empty where no significant performance is expected either due to saturation (left-side) or sky count overtaking the target magnitude (bottom-left).

It shows that the most significant improvement is for stars that are just below the linearity point. With this evidence the Open University has started a program to optimise the flat fielding acquisition for PIRATE. However, at this time no improved flats have been acquired.

The current flats give the predicted uncertainty for WASP-12 b and HAT-P-44 b as 3.584 ppt and 3.798 ppt respectively. This is 21.08% and 19.98% off the predicted uncertainty using the better flats respectively. This gives more evidence that the flats are off from what they used to be.

5.3 Website

The Website takes in the calculated values of a setup into it, in order to predict the precision. This means that it can easily break down the errors which can lead to improvements in the telescope.

The Website is able to predict exoplanet transits, which means that it can work out what the airmass is going to be for that particular exoplanet transit, leaving the magnitude of the star in the filter that is going to be used and the exposure time needing to be worked out.

5.3.1 Improvements to telescopes

This work has been shown to improve telescopes, as can be seen from PIRATE. Improving the PIRATE flat fields has been shown to give a theoretical 5 to 20 % improvement in the predicted uncertainty.

One of the ways to improve the setup is to look at one of the plots that the website can produce. Figure 2.2 shows the percentage breakdown of the errors that come from a system, so it can be seen where the biggest error is. Then it can be looked into to see if it can be improved or not.

However, as the flat fields for all the telescope systems that were tested were not optimized, this could not be done. The best way to improve all of the telescope systems was to improve the flat field calibration images. It can also be used to find the best filter to observe a target in, in order to get the best uncertainty for that target, given no filter requirements.

5.3.2 Transit predictions

For TOIs, the TESS transit finder was used more than the website for predicting the transit times. This is in part due to it containing information, based on what other observations of that object have found, as well as what the TESS team would like to see. E.g. the next observation should be a high precision (<1.0 ppt/min) full transit in a blue (U, u', B, g') filter to check for chromaticity.

This is something that the website could not automatically copy, due to these comments being on a secure server. But the website was used for predicting the weather and the uncertainty expected which could not be done on the TESS transit finder.

One of the things that KPS-1 b shows, is that the period of the exoplanet needs to be very well known in order not to lose the transit time. As the number of exoplanets increases (Heller and Kiss 2019), the time focused on each exoplanet is likely to decrease, even assuming an increase the overall telescope time. However, the effect of this will likely be to focus most observing resources on smaller mass exoplanets that are Earth-like and relatively less well studied.

It is important to have an area (Website - Swarthmore Transit Finder) where the uncertainty in the mid-transit time can be monitored, so that the community can be alerted to when a transit's uncertainty is too long. This is what the TESS transit finder has become for the TOIs.

5.4 Identification of Further Work

The key areas where further work would be particularly useful are to:-

1. Investigate the effect that different spectral type of reference stars compared to the target has on the produced error.
2. Change the way that the telescope information is uploaded to the website, so that the filter and binning options can be selected and changed when looking at transits. Or automatically suggest which filter and binning to use to achieve the lowest uncertainty.
3. Investigate the importance of auto-guiding and flat field noise from the predicted equation. For example, NGTS has achieved an RMS of 0.04 pixels for the tracking (Wheatley et al. 2017) whereas Bayfordbury has an RMS of around 3 pixels, with no active tracking.
4. Investigate the impact on data binning on the predicted uncertainty of the data. In particular, investigate the difference whether or not it affects the difference between the predicted uncertainty and the achieved RMS for the un-binned data.

6 Conclusions

This work outlines the approach taken in the website, The Transit Follow Up Tool, to predict the precision for a given telescope, detector and site. Once the calibration of the setup is done it only requires the catalogue magnitude, exposure time and air mass to predict the photometric precision of a transit observation.

Comparing the predicted precision from each setup to the achieved RMS of the transit fits, they are all within 0.1 ppt with the most extreme difference being only 0.07 ppt off. Given that P. J. Beck (2018) found this to be 1.8 ppt (2 mmag), this shows that increasing the number of reference stars, as Beck only used one, can help bring the predicted precision closer to the achieved.

KPS-1 b is the only confirmed exoplanet transit that has a significant shift in the mid-transit time, but it is most likely due to the period not being known correctly. None of the other confirmed exoplanets show any significant evidence of TTV. TOI 516.01 showed a shift in the mid-transit time, which was also due to the period not being known correctly, rather than another planet causing it.

The calibration of the PIRATE telescope over the 2 different binning options, 1x1 and 2x2 has helped to show that for the PIRATE 2x2 binning gives a 10-30% improvement when compared to 1x1 binning, depending on what the magnitude is and what exposure time is used.

The website can break down the predicted precision into the different error types. This can help to improve the uncertainty, as can be seen from PIRATE. This should improve precision in mmag by approximately 5-20% depending on the magnitude of the star and exposure time used.

In summary, one of the most important parts in getting high precision photometry is to take good calibration images. As Bruce Gary (2007) says "The longer I try to improve flat fields the more I've come to believe that perfect flat fields are fundamentally impossible". This can be especially true for twilight flats, as the timing of the flats has to be right for each filter.

7 References

Agol, E. (2012). "Basic light curve models". URL: http://nexsci.caltech.edu/workshop/2012/talks/Agol_Sagan2012.pptx.pdf.

Alonso, R. et al. (2007). "The Transatlantic Exoplanet Survey (TrES): A Review". *Astronomical Society of the Pacific Conference Series,* 366, p. 13.

Bakos, G. Á. et al. (2011). "HAT-P-20b-HAT-P-23b: Four Massive Transiting Extrasolar Planets". *ApJ,* 742, p. 116. DOI: 10.1088/0004-637X/742/2/116.

Bakos, G. et al. (2004). "Wide-Field Millimagnitude Photometry with the HAT: A Tool for Extrasolar Planet Detection". *PASP,* 116, p. 266. DOI: 10.1086/382735.

Baldry, I. K. (1999). "Time-Series Spectroscopy of Pulsating Stars". *University of Sydney,* URL: http://www.astro.ljmu.ac.uk/~ikb/thesis/baldry-ch3.pdf.

Barclay, Thomas, Joshua Pepper, and Elisa V. Quintana (2018). "A Revised Exoplanet Yield from the Transiting Exoplanet Survey Satellite (TESS)". *The Astrophysical Journal Supplement Series* 239, p. 2. DOI: 10.3847/1538-4365/aae3e9.

Batalha, Natalie M. (2014). "Exploring exoplanet populations with NASA's Kepler Mission". *Proceedings of the National Academy of Sciences,* 111, pp. 12647–12654. DOI: 10.1073/pnas.1304196111.

Beck, P. J. (2018). "Precision Photometry at the University of Hertfordshire's Bayfordbury Observatory". *University of Hertfordshire,* URL: http://hdl.handle.net/2299/19912.

Beck, P. J et al. (2019). "Efficient Follow-up of Exoplanet Transits Using Small Telescopes". *PASP,* 131, p. 084402. DOI: 10.1088/1538-3873/ab1eb4.

Benni, P. (2020). "Observing Notes for TIC ID 16102323". URL: https://exofop.ipac.caltech.edu/tess/edit_obsnotes.php?id=16102323.

Bessell, M. S. (2005). "Standard Photometric Systems". *ARA&A,* 43, p. 293. DOI: 10.1146/annurev.astro.41.082801.100251.

Bieryla, A. (2020). "Observing Notes for TIC ID 387259626". URL: https://exofop.ipac.caltech.edu/tess/edit_obsnotes.php?id=387259626.

Borucki, William J. (2020). "Science Merit Function for the KEPLER Mission". arXiv, 2005.07831.

Burdanov, A. et al. (2018). "KPS-1b: The First Transiting Exoplanet Discovered Using an Amateur Astronomer's Wide-field CCD Data". *PASP,* 130, p. 074401. DOI: 10.1088/1538-3873/aabde2.

Chakrabarty, A. and S. Sengupta (2019). "Precise Photometric Transit Follow-up Observations of Five Close-in Exoplanets: Update on Their Physical Properties". *AJ,* 158, p. 39. DOI: 10.3847/1538-3881/ab24dd.

Claret, A. and S. Bloemen (2011). "Gravity and limb-darkening coefficients for the Kepler, CoRoT, Spitzer, uvby, UBVRIJHK, and Sloan photometric systems". *A&A,* 529, A75. DOI: 10.1051/0004-6361/201116451.

Collins, K. (2019). "TFOP SG1 email". QLP depth.

Collins, K. et al. (2017). "AstroImageJ: Image Processing and Photometric Extraction for Ultra-Precise Astronomical Light Curves (Expanded Edition)". *AJ,* 153, p. 77. DOI: 10.3847/1538-3881/153/2/77.

Cowen, Ron (2013). "The wheels come off Kepler". *Nature,* 497, p. 417. DOI: 10.1038/497417a.

Crossfield, I. (2019). "Observing Notes for TIC ID 318937509". URL: https://exofop.ipac.caltech.edu/tess/edit_obsnotes.php?id=318937509.

Csizmadia, S. et al. (2013). "The effect of stellar limb darkening values on the accuracy of the planet radii derived from photometric transit observations". *A&A,* 549, A9. DOI: 10.1051/0004-6361/201219888.

Deleuil, Magali and Malcolm Fridlund (2018). "CoRoT: The First Space-Based Transit Survey to Explore the Close-in Planet Population". *Handbook of Exoplanets*, pp. 1135–1158. DOI: 10.1007/978-3-319-55333-7_79.

Dravins, D. et al. (1998). "Atmospheric Intensity Scintillation of Stars. III. Effects for Different Telescope Apertures". *PASP,* 110, p. 610. URL: http://www.jstor.org/stable/10.1086/316161.

Eastman, J., R. Siverd, and S. B.Gaudi (2010). "Achieving Better Than 1 Minute Accuracy in the Heliocentric and Barycentric Julian Dates". *PASP,* 122, p. 935. DOI: 10.1086/655938.

Foreman-Mackey, Daniel et al. (2016). "The Population of Long-Period Transiting Exoplanets". *AJ,* 152, p. 206. DOI: 10.3847/0004-6256/152/6/206.

Fressin, François et al. (2013). "The False Positive Rate of Kepler and the Occurrence of Planets". *ApJ,* 766, p. 81. DOI: 10.1088/0004-637X/766/2/81.

Gary, B. L. (2007). "Exoplanet Observing For Amateurs". URL: http://brucegary.net/book_EOA/EOA.pdf.

Gilliland, Ronald et al. (2011). "Kepler Mission Stellar and Instrument Noise Properties". *The Astrophysical Journal Supplement Series,* 197, p. 6. DOI: 10.1088/0067-0049/197/1/6.

Girardin, E., K. Collins, and A. Bieryla (2019). "ExoFOP TIC 318937509". URL: https://exofop.ipac.caltech.edu/tess/target.php?id=318937509.

Grossman, A. and J. Turner (2019). "Dark Sky". URL: https://darksky.net/.

Han, E. et al. (2014). "Exoplanet Orbit Database. II. Updates to Exoplanets.org". *PASP,* 126, p. 827. DOI: 10.1086/678447.

Hartman, J.D. et al. (2014). "HAT-P-44b, HAT-P-45b, and HAT-P-46b: Three Transiting Hot Jupiters in Possible Multi-planet Systems". *AJ,* 147, p. 128. DOI: 10.1088/0004-6256/147/6/128.

Hébrard, G. et al. (2013). "WASP-52b, WASP-58b, WASP-59b, and WASP-60b: Four new transiting close-in giant planets". *A&A,* 549, p. 134. DOI: 10.1051/0004-6361/201220363.

Heller, R. and L. Kiss (2019). "Exoplanet Vision 2050". arXiv, 1911.12114.

Howell, S. B. (2000). "Handbook of CCD Astronomy". *Cambridge University Press* 1.

Jansen, Rolf A. and Rogier A. Windhorst (2018). "The James Webb Space Telescope North Ecliptic Pole Time-domain Field. I. Field Selection of a JWST Community Field for Time-domain Studies". *PASP,* 130, p. 124001. DOI: 10.1088/1538-3873/aae476.

Jensen, E. (2013). "Tapir: A web interface for transit/eclipse observability". *Astrophysics Source Code Library,* p. 1306.

Kipping, David M. (2009). "Transit timing effects due to an exomoon". *Monthly Notices of the Royal Astronomical Society,* 392, pp. 181–189. DOI: 10.1111/j.1365-2966.2008.13999.x.

Lang, D. et al. (2010). "Astrometry.net: Blind Astrometric Calibration of Arbitrary Astronomical Images". *AJ,* 139, p. 1782. DOI: 10.1088/0004-6256/139/5/1782.

Latham, D. W. et al. (1989). "The unseen companion of HD114762: a probable brown dwarf". *Nature,* 339, p. 38. DOI: 10.1038/339038a0.

Louie, Dana R. et al. (2018). "Simulated JWST/NIRISS Transit Spectroscopy of Anticipated Tess Planets Compared to Select Discoveries from Space-based and Ground-based Surveys". *PASP,* 130, p. 044401. DOI: 10.1088/1538-3873/aaa87b.

Ofir, A. (2016). "Planetary Transits How can one measure the mass size density and atmospheric composition of a planet one cannot even see?" URL: https://palereddot.org/planetary-transits-how-can-one-measure-the-mass-size-density-and-atmospheric-composition-of-a-planet-one-cannot-even-see/.

Öztürk, O. and A. Erdem (2019). "New photometric analysis of five exoplanets: CoRoT-2b, HAT-P-12b, TrES-2b, WASP-12b, and WASP-52b". *MNRAS,* 486, p. 2290. DOI: 10.1093/mnras/stz747.

Poddaný, Stanislav, Luboš Brát, and Ondřej Pejcha (2010). "Exoplanet Transit Database. Reduction and processing of the photometric data of exoplanet transits". *New Astronomy,* 15, p. 297. URL: http://www.sciencedirect.com/science/article/pii/S1384107609001213.

Pollacco, D. L. et al. (2006). "The WASP Project and the SuperWASP Cameras". *PASP,* 118, p. 1407. DOI: 10.1086/508556.

Relles, H., J. Kielkopf, and P. Evans (2019). "Observing Notes for TIC ID 445822015". URL: https://exofop.ipac.caltech.edu/tess/edit_obsnotes.php?id=445822015.

Ricker, G. R. et al. (2014). "Transiting Exoplanet Survey Satellite". *Journal of Astronomical Telescopes, Instruments, and Systems,* 1, p. 014003. URL: http://dx.doi.org/10.1117/1.JATIS.1.1.014003.

Romanishin, W. (2006). "An Introduction to Astronomical Photometry Using CCDs". *University of Oklahoma*. URL: http://vitaly.neustroev.net/teaching/docs/wrccd22oct06.pdf.

Schmude, R. W. (1994). "Atmospheric Extinction Coefficients Measured at Texas A&M University Observatory". *International Amateur-Professional Photoelectric Photometry Communications,* 57, p. 12.

Southworth, J. et al. (2009). "High-precision photometry by telescope defocusing - I. The transiting planetary system WASP-5". *MNRAS,* 396, p. 1023. DOI: 10.1111/j.1365-2966.2009.14767.x.

Sullivan, P. W. et al. (2015). "The Transiting Exoplanet Survey Satellite: Simulations of planet detections and astrophysical false positives". *ApJ,* 809, p. 77. DOI: 10.1088/0004-637x/809/1/77.

Todorov, Kamen (2008). "Determining the Temperature of Exoplanet HAT-P-1b". *Physics, Astronomy and Geophysics Honors Papers* 1.

Wheatley, P. J. et al. (2017). "The Next Generation Transit Survey (NGTS)". *MNRAS,* 475, p. 4476. DOI: 10.1093/mnras/stx2836.

Wilson, Paul Anthony (2015). "The exoplanet transit method". URL: https://www.paulanthonywilson.com/exoplanets/exoplanet-detection-techniques/the-exoplanet-transit-method/.

Wolszczan, A. and D. A. Frail (1992). "A planetary system around the millisecond pulsar PSR1257+ 12". *Nature,* 355, p. 145. DOI: 10.1038/355145a0.

Zissell, R. E. (2000). "Shutter Mapping Correction for Short CCD Exposures". *Journal of the American Association of Variable Star Observers,* 28, p. 149.

8 Abbreviations

ADU	Analogue-to-digital units
AIJ	AstroImageJ
APT	Aperture Photometry Tool
CCD	Charge Coupled Device
CKT	Chris Kitchen Telescope
ExoFOP	Exoplanet Follow-up Observing Program
FWHM	Full Width Half Maximum
JHT	Jim Hough Telescope
NEB	Nearby Eclipsing Binary
PIRATE	Physics Innovations Robotic Telescope Explorer
QLP	Quick Look Pipeline
RMS	Root Mean Square
RPT	Robert Priddey Telescope
RTML	Real Time Markup Language
SBO	Spring Brook Observatory
SD	Standard Deviation
SG	Sub Groups
SRO	Sierra Remote Observatories
TESS	Transiting Exoplanet Survey Satellite
TFOP	TESS Follow-up Observing Program
TNT	Thai National Telescope
TOI	TESS Objects of Interest
TRT	Thai Robotic Telescope
TTV	Transit Time Variations
ppt	parts per thousand
ppm	parts per million

9 Acknowledgements

Support is acknowledged from Prof H Jones, Dr R Errmann and Prof W Martin for the supervision and advice during the conduct of this project.

Support is also acknowledged from Supachai Awiphan for the help and telescope time for the TRT. David Campbell and Dr Samantha Rolfe for helping resolve various technical issues at Bayfordbury. Dr Ulrich Kolb, Richard Busuttil and Samuel Jackson for help giving access to the PIRATE archive.

Also offer special recognition of the work of Peter Beck who passed away in 2019. This work has been built upon his work, specifically chapters 2.1 from his MSc by research degree thesis (P. J. Beck 2018).

This research has made use of APT and Python for the analysis of data. The Exoplanet transit tool of the Czech Astronomical Society has been used in developing the online resource.

This research has made extensive use of the SIMBAD database, operated at CDS, Strasbourg, France and the NASA Exoplanet Archive. The Exoplanet Follow-up Observation Program websites, which are operated by the California Institute of Technology, under contract with the National Aeronautics and Space Administration under the Exoplanet Exploration Program. I have been supported by a Brian May scholarship.

10 Appendices

10.1 Transits

This section displays the transits that had been observed too late to go into the thesis.

10.1.1 TOI 1694.01 on 2020 02 05 with TNT

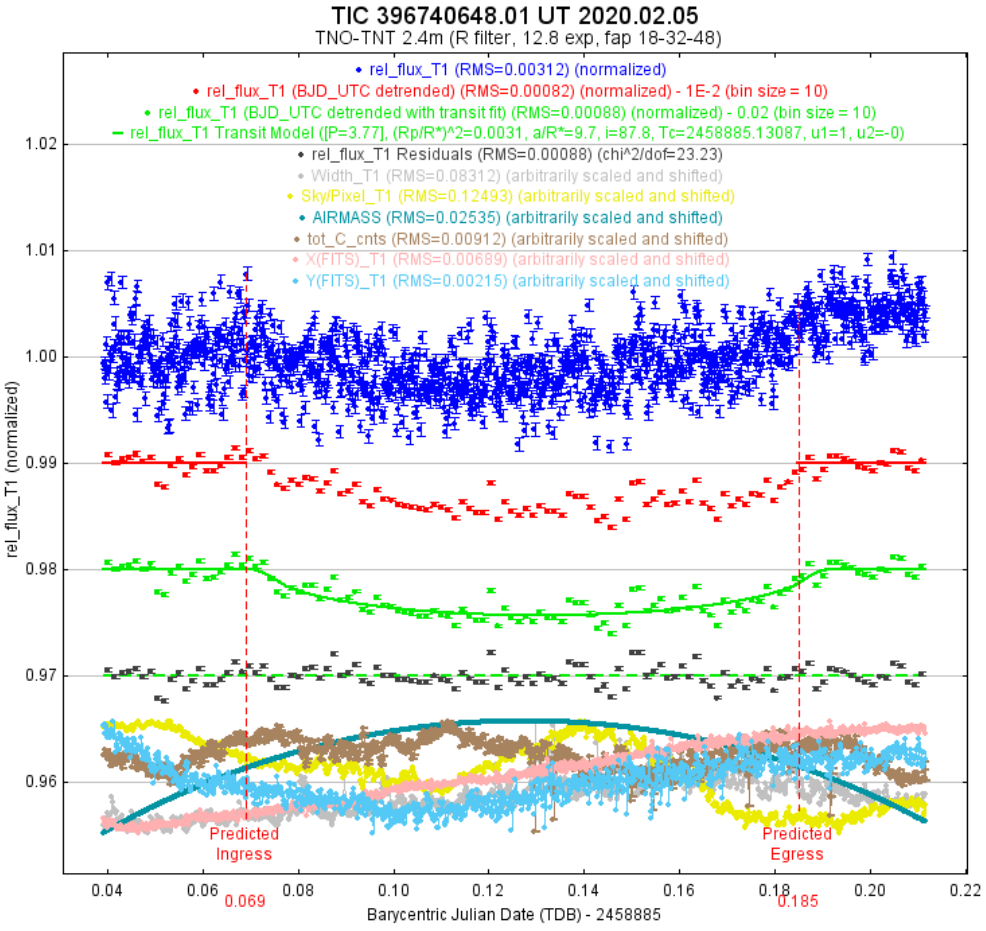

Figure 10.1: TOI 1694.01 transit fit using AIJ. The target then detrended by BJD_{UTC}, with the model fit detrended and the residuals from the fit.

Found a Transit on target with a slightly smaller transit depth than reported. The transit fit gave a depth of 3.09 ppt rather than the expected 4.36 ppt. The transit time is also slightly longer (around 5 minutes) than predicted.

Figure 10.1 shows the light curve of TOI 1694.01, as it was observed with an exposure time of 12.8 seconds.

As the FOV for TNT is small, only 3 good reference stars appear outside the TESS aperture so the results give a tentative transit. The data was binned by 10 to give an approximate 130 seconds cadence.

10.1.2 TOI 1516.01 on 2020 02 06 with JHT

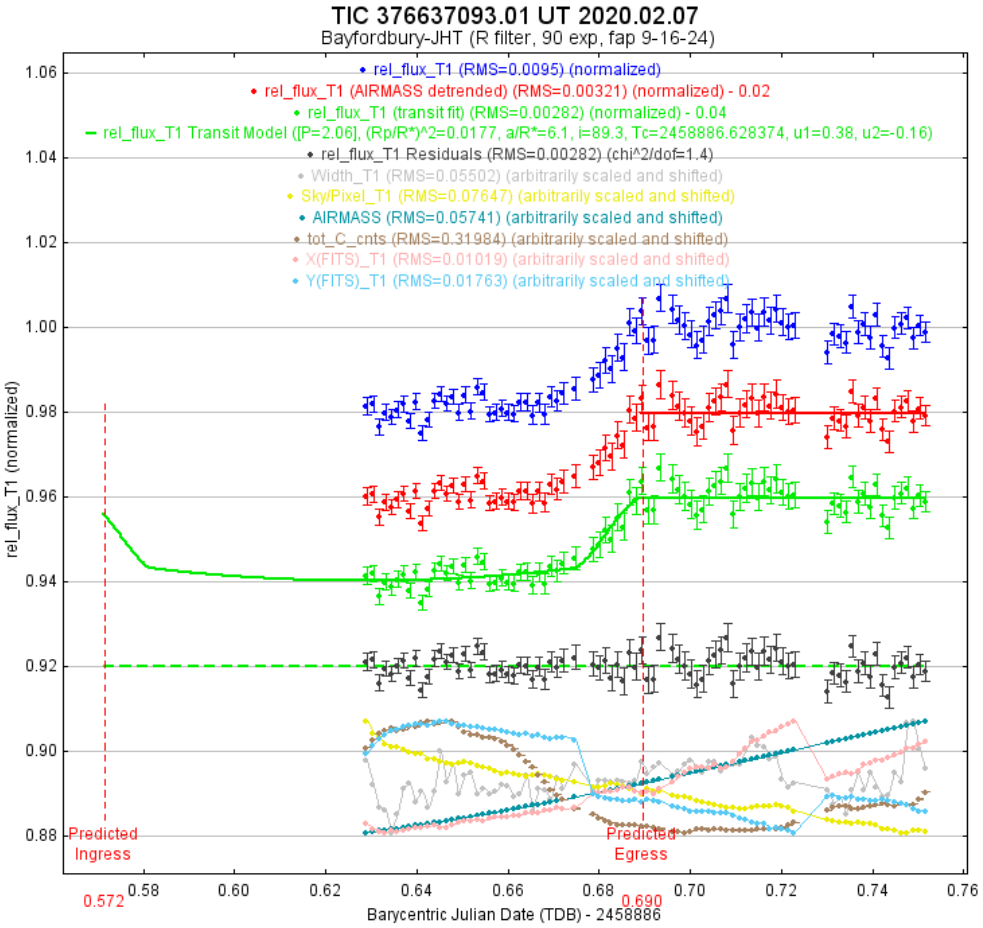

Figure 10.2: TOI 1516.01 transit fit using AIJ. The target then detrended by air mass, with the model fit and the residuals from the fit.

Observed partial transit of TOI 1516 due to high moon (93% full) and some clouds. Figure 10.2 shows the light curve of TOI 1516.01. The light curve is not detrended as it is only half the transit. It does, however, confirm that TESS signal is on target and around the correct depth that was reported at 16.57 ppt versus the raw fit of 17.7 ppt.

10.2 Telescopes

Table 10.1 shows the list of telescopes used, where they are located and who controls them. Table 10.2 to Table 10.4 shows what filters (Johnson) were available for the different telescopes and what cameras were used. The National Astronomical Research Institute of Thailand is abbreviated as NARIT.

Table 10.1: List of telescopes

Name	Location	Latitude	Longitude	Organization
SBO	Australia, New South Wales	-28.191	153.265	NARIT
SRO	USA, California	37.070	-119.413	NARIT
GMGO	China, Yunnan	26.695	105.031	NARIT
TNT	Thailand, Chiang Mai Province	18.574	98.482	NARIT
CKT	UK, Hertfordshire	51.482	-0.09	University of Hertfordshire
JHT	UK, Hertfordshire	51.482	-0.09	University of Hertfordshire
RPT	UK, Hertfordshire	51.482	-0.09	University of Hertfordshire
PIRATE	Tenerife	28.300	-16.509	Open University

Table 10.2: NARIT technical list

Name	Camera	Filter
SBO	Proline PL16803	B, V, R, I, Lum, RED, Green, Blue
SRO	Proline PL16803	Blue, Green, Red, Lum, H-alpha, S-II, O-III
GMGO	DW936_BV	U, B, V, R, I
TNT	ULTRASPEC	U, B, V, R, I

Table 10.3: Bayfordbury technical list

Name	Camera	Filter
CKT	SBIG STL-6303E	Clear, R, V, B, H-alpha
JHT	SBIG STL-6303E	Clear, R, V, B, I, H-alpha, S-II, O-III
RPT	Moravian Instruments G4-9000	Clear, R, V, B, I

Table 10.4: Open University technical list

Name	Camera	Filter
PIRATE	FLI ProLine PL16803	U, B, V, R, I

10.3 Predicted precision

Table 10.5 shows the values used for the predicted precision for the different telescopes.

For the Pirate telescope, the total counts that were used to predict the precision as the transits observed did not have a known magnitude in the filter. HAT-P-44 b used 133,000 ADU and air mass of 1.25 using an exposure time of 150 seconds. WASP-12 b used 164,000 ADU and air mass of 1.05 using an exposure of 45 seconds.

For the Thai telescopes, the SBO for TOI 689.01 used 808,200 ADU with an air mass of 1.45 and exposure time of 60 seconds. For the TNT on the TOI 516.01 used 25,800 ADU with an air mass of 1.25 and exposure time of 200 seconds.

Table 10.5: The values that were used for the calculation of the predicted precision

	TNT	SBO	CKT	RPT	JHT	PIRATE
Filter	B	R	V	V	V	R
Bias	2.095	8.93	6.37	14.86	6.37	11.042
Dark	0.005	0.001	0.0028	0.69	0.0028	0.0584
Flat	0.004933	0.001925	0.00211	0.00211	0.00211	0.000864
Scintil-ation	0.001633	0.004478	0.007313	0.007313	0.007313	0.005911
Sky Constant	3.71	0.72	3.95	6.71	3.95	7.33
Sky SD	0.7	0.078	0.078	0.255	0.078	0.252
E	0.4	0.1	0.2	0.2	0.2	0.1
Gradient	N/A	N/A	1.0023	1.0857	1.0023	1.1232
Bias	N/A	N/A	-20.2122	-21.455	-20.2122	-21.773

10.4 TOI Help

Below is the list of documents needed when following up TOIs

1. Photometry table
2. Configuration file

3. Aperture file
4. Light curve plot
5. Image with apertures
6. A plate solved image
7. Seeing profile
8. Notes and results file
9. Delta Dmag vs RMS plot
10. NEB table
11. NEB depth plot files
12. Zoomed in field of view

10.5 Telescope Sites

10.5.1 Submitting Robotically Controlled Observations at Different Sites

For the Bayfordbury Observatory, observing plans are submitted using RTML code that for exoplanets are generated by the transit follow-up tool.

For the TRT, the observatory's website is used to input the position of the object and the binning needed before setting the type of mode, priority of the plan. Then adding the filter and exposure time being used.

For PIRATE, the Open University‘s website uses a single page to load in the required information for the telescope.

10.5.2 Location of the Images

All images reported in this thesis are available by arrangement from the appropriate organization;
University of Hertfordshire Bayfordbury Observatory
Thai Robotic Telescope
Open University - Astro Drive

10.6 Instrument vs Catalogue

The Table 10.6 shows the Instrument vs Catalogue data for PIRATE for R filter and 2x2 binning. With the object name, exposure time, air mass, the count and its uncertainty. As well as the peak pixel value, R magnitude and its uncertainty if it has one, the calculated instrument magnitude for air mass of 1 and exposure time of 1. With the predicted count calculated using Figure 2.1 and the difference between the counts and predicted counts in magnitudes. The source for the catalogue magnitude and error was SIMBAD database.

Table 10.6: Instrument vs Catalogue table

Object	$Texp$ (s)	Air mass	Count (ADU)	Count Uncer-tainty (ADU)	Peak Pixel (ADU)	R Mag	R Mag error	Inst cat per sec air of 1	Pred-icted Count (ADU)	Delta Mag
UCAC2 19890828	60	1.845	110084	367	31608	12.46	0.07	-8.243	71699	-0.466
UCAC2 19890828	60	1.852	109596	365	30702	12.46	0.07	-8.239	71657	-0.461
UCAC2 19890828	60	1.859	110397	365	27163	12.46	0.07	-8.248	71607	-0.470
UCAC2 19890851	60	1.840	244099	521	49971	11.56	0.04	-9.108	182001	-0.319
UCAC2 19890851	60	1.852	244364	517	56506	11.56	0.04	-9.110	181807	-0.321
UCAC2 19890815	60	1.840	56928	290	15893	13.08	0.07	-7.527	37772	-0.445
UCAC2 19890815	60	1.845	57005	286	16025	13.08	0.07	-7.529	37754	-0.447
UCAC2 19890815	60	1.852	56154	284	15687	13.08	0.07	-7.513	37732	-0.432
UCAC2 19890815	60	1.859	57272	282	14731	13.08	0.07	-7.535	37705	-0.454
UCAC2 19890699	60	1.845	233616	509	54432	11.59	0.03	-9.060	176356	-0.305
UCAC2 19890699	60	1.859	232221	506	50731	11.59	0.03	-9.055	176127	-0.300
UCAC2 20140719	60	1.840	92770	346	19062	12.54	0.06	-8.057	66036	-0.369
UCAC2 20140719	60	1.845	93099	344	28216	12.54	0.06	-8.062	66004	-0.373
UCAC2 20140719	60	1.852	92206	341	19839	12.54	0.06	-8.052	65966	-0.364
UCAC2 20140719	60	1.859	93046	340	27185	12.54	0.06	-8.062	65919	-0.374
UCAC2 19890637	60	1.840	88343	340	22298	12.66	0.06	-8.004	58327	-0.451
UCAC2 19890637	60	1.845	88275	337	17541	12.66	0.06	-8.004	58299	-0.450
UCAC2 19890637	60	1.852	88982	336	20577	12.66	0.06	-8.013	58264	-0.460
UCAC2 19890637	60	1.859	88919	334	17609	12.66	0.06	-8.013	58223	-0.460
2MASS J14110426 +4701401	150	1.229	1446	192	872	17.20	0.35	-2.483	1408	-0.029
TYC 3463-582-1	150	1.128	1084816	1188	29540	10.60	0.1	-9.661	1311590	0.206
TYC 3463-582-1	150	1.116	1088883	1190	27614	10.60	0.1	-9.664	1313020	0.203
TYC 3463-582-1	150	1.106	1082285	1187	23861	10.60	0.1	-9.656	1314306	0.211
TYC 3463-582-1	150	1.096	1084475	1188	23342	10.60	0.1	-9.657	1315457	0.210
TYC 3463-582-1	150	1.088	1088184	1190	24329	10.60	0.1	-9.660	1316473	0.207
TYC 3463-58-1	150	1.128	1078805	1186	25116	10.60	0.1	-9.655	1311590	0.212
TYC 3463-58-1	150	1.116	1082881	1188	23176	10.60	0.1	-9.658	1313020	0.209
TYC 3463-58-1	150	1.106	1077299	1185	20361	10.60	0.1	-9.651	1314306	0.216
TYC 3463-58-1	150	1.096	1079968	1187	20206	10.60	0.1	-9.653	1315457	0.214
TYC 3463-58-1	150	1.088	1083210	1188	20111	10.60	0.1	-9.655	1316473	0.212
TYC 3463-348-1	150	1.128	765862	1045	18271	11.00	0.1	-9.283	867134	0.135
TYC 3463-348-1	150	1.116	769472	1047	16653	11.00	0.1	-9.287	868079	0.131
TYC 3463-348-1	150	1.106	765690	1045	14605	11.00	0.1	-9.280	868930	0.137
TYC 3463-348-1	150	1.096	768849	1047	14671	11.00	0.1	-9.284	869690	0.134
TYC 3463-348-1	150	1.088	773353	1049	14730	11.00	0.1	-9.289	870362	0.128
TYC 3460-285-1	150	1.128	788774	1056	29056	10.80	0.1	-9.315	1066454	0.327
TYC 3460-285-1	150	1.116	790094	1057	26563	10.80	0.1	-9.316	1067617	0.327
TYC 3460-285-1	150	1.106	786021	1055	24606	10.80	0.1	-9.309	1068663	0.334
TYC 3460-285-1	150	1.096	789516	1057	23461	10.80	0.1	-9.313	1069598	0.330
TYC 3460-285-1	150	1.088	790327	1057	27985	10.80	0.1	-9.313	1070424	0.329
TYC 3460-642-1	150	1.128	725175	1025	28482	11.00	0.1	-9.224	867134	0.194
TYC 3460-642-1	150	1.116	728741	1027	26527	11.00	0.1	-9.228	868079	0.190
TYC 3460-642-1	150	1.106	726682	1026	23359	11.00	0.1	-9.224	868930	0.194
TYC 3460-642-1	150	1.096	726741	1026	23626	11.00	0.1	-9.223	869690	0.195
TYC 3460-642-1	150	1.088	728662	1027	25699	11.00	0.1	-9.225	870362	0.193
TYC 3463-587-1	150	1.128	785678	1055	18538	11.10	0.1	-9.311	781912	-0.005
TYC 3463-587-1	150	1.116	787756	1056	16735	11.10	0.1	-9.312	782765	-0.007
TYC 3463-587-1	150	1.106	781743	1053	14744	11.10	0.1	-9.303	783532	0.002
TYC 3463-587-1	150	1.096	785896	1055	14690	11.10	0.1	-9.308	784218	-0.002
TYC 3463-587-1	150	1.088	786265	1055	14639	11.10	0.1	-9.307	784824	-0.002
GPM 202.306244 +47.237732	150	1.128	276627	777	9825	12.10	0.1	-8.177	277893	0.005
GPM 202.306244 +47.237732	150	1.116	276930	777	8886	12.10	0.1	-8.177	278196	0.005
GPM 202.306244 +47.237732	150	1.106	275453	776	7816	12.10	0.1	-8.170	278469	0.012
GPM 202.306244 +47.237732	150	1.096	275759	776	7879	12.10	0.1	-8.171	278713	0.012
GPM 202.306244 +47.237732	150	1.088	277017	777	7790	12.10	0.1	-8.175	278928	0.007
GPM 202.105136 +47.314843	150	1.128	230647	746	8888	12.40	0.1	-7.980	203748	-0.135

Continued on next page

Table 10.6 – *Continued from previous page*

Object	$Texp$ (s)	Air mass	Count (ADU)	Count Uncertainty (ADU)	Peak Pixel (ADU)	R Mag	R Mag error	Inst cat per sec air of 1	Predicted Count (ADU)	Delta Mag
GPM 202.105136 +47.314843	150	1.116	230816	746	8579	12.40	0.1	-7.980	203971	-0.134
GPM 202.105136 +47.314843	150	1.106	229020	745	7565	12.40	0.1	-7.970	204170	-0.125
GPM 202.105136 +47.314843	150	1.096	230018	746	7522	12.40	0.1	-7.974	204349	-0.128
GPM 202.105136 +47.314843	150	1.088	230788	746	8477	12.40	0.1	-7.977	204507	-0.131
GPM 202.612494 +47.039826	150	1.128	148890	689	5072	12.40	0.1	-7.505	203748	0.341
GPM 202.612494 +47.039826	150	1.116	149310	690	4705	12.40	0.1	-7.507	203971	0.339
GPM 202.612494 +47.039826	150	1.106	148189	689	4203	12.40	0.1	-7.497	204170	0.348
GPM 202.612494 +47.039826	150	1.096	148911	689	4090	12.40	0.1	-7.502	204349	0.344
GPM 202.612494 +47.039826	150	1.088	150177	690	4335	12.40	0.1	-7.510	204507	0.335
GPM 202.235932 +47.295371	150	1.128	163161	700	6140	12.60	0.1	-7.604	165668	0.017
GPM 202.235932 +47.295371	150	1.116	163038	699	5735	12.60	0.1	-7.602	165848	0.019
GPM 202.235932 +47.295371	150	1.106	162022	699	5106	12.60	0.1	-7.594	166011	0.026
GPM 202.235932 +47.295371	150	1.096	163041	700	5138	12.60	0.1	-7.600	166156	0.021
GPM 202.235932 +47.295371	150	1.088	163191	699	5714	12.60	0.1	-7.600	166285	0.020
GPM 202.263602 +46.931821	150	1.128	112876	662	5159	12.70	0.1	-7.204	149386	0.304
GPM 202.263602 +46.931821	150	1.116	113231	662	4797	12.70	0.1	-7.206	149549	0.302
GPM 202.263602 +46.931821	150	1.106	112552	662	4440	12.70	0.1	-7.199	149695	0.310
GPM 202.263602 +46.931821	150	1.096	112862	662	4302	12.70	0.1	-7.201	149826	0.308
GPM 202.263602 +46.931821	150	1.088	113480	662	4636	12.70	0.1	-7.206	149942	0.303
GPM 202.811648 +46.927299	150	1.128	95196	648	3379	12.80	0.1	-7.019	134704	0.377
GPM 202.811648 +46.927299	150	1.116	94697	648	3248	12.80	0.1	-7.012	134851	0.384
GPM 202.811648 +46.927299	150	1.106	94076	648	3055	12.80	0.1	-7.004	134983	0.392
GPM 202.811648 +46.927299	150	1.096	95004	648	3019	12.80	0.1	-7.014	135102	0.382
GPM 202.811648 +46.927299	150	1.088	94757	648	3122	12.80	0.1	-7.010	135206	0.386
GPM 202.840490 +47.374990	150	1.128	82596	639	2913	13.00	0.1	-6.865	109528	0.306
GPM 202.840490 +47.374990	150	1.116	82667	639	2637	13.00	0.1	-6.865	109648	0.307
GPM 202.840490 +47.374990	150	1.106	81509	638	2537	13.00	0.1	-6.848	109755	0.323
GPM 202.840490 +47.374990	150	1.096	82149	638	2474	13.00	0.1	-6.856	109851	0.316
GPM 202.840490 +47.374990	150	1.088	82932	639	2474	13.00	0.1	-6.865	109936	0.306
WASP-16	25	1.670	141615	447	10431	11.00	0.1	-9.450	137482	-0.032
WASP-16	25	1.520	142811	443	9387	11.00	0.1	-9.444	139401	-0.026
TYC 6147-30-1	25	1.670	124403	426	10219	11.06	0.1	-9.309	129208	0.041
TYC 6147-30-1	25	1.520	123916	420	8872	11.06	0.1	-9.290	131012	0.060
UCAC2 23635524	25	1.670	100660	395	9140	11.67	0.04	-9.079	68743	-0.414
UCAC2 23635524	25	1.520	102174	391	7665	11.67	0.04	-9.080	69703	-0.415
UCAC4 346-070257	25	1.670	75095	360	6834	11.89	0.05	-8.761	54524	-0.348
UCAC4 346-070257	25	1.520	75422	355	6061	11.89	0.05	-8.751	55285	-0.337
TYC 3162-665-1	60	1.543	175544	433	37293	11.75	0.1	-8.720	153670	-0.144
TYC 3162-665-1	60	1.519	177924	443	28667	11.75	0.1	-8.732	154017	-0.157
2MASS J20062120 +4430520	60	1.543	72551	293	13135	12.41	0.1	-7.761	77636	0.074
2MASS J20062120 +4430520	60	1.519	72423	304	13004	12.41	0.1	-7.756	77811	0.078
TYC 1501-372-1	13	1.406	141598	378	10661	9.96	0.02	-10.133	214827	0.453
HD 140753	15	1.966	250430	505	36217	9.66	0.1	-10.653	321086	0.270
HD 140753	15	1.949	251936	507	37501	9.66	0.1	-10.658	321587	0.265
HD 140753	15	1.929	255027	510	38539	9.66	0.1	-10.669	322158	0.254
HD 140753	15	1.914	255539	510	36241	9.66	0.1	-10.670	322620	0.253
UCAC2 24368299	15	1.966	91733	311	16553	10.95	0.03	-9.563	84538	-0.089
UCAC2 24368299	15	1.949	92585	312	13941	10.95	0.03	-9.571	84670	-0.097
UCAC2 24368299	15	1.929	92040	311	15449	10.95	0.03	-9.563	84820	-0.089
UCAC2 24368299	15	1.914	93333	313	14830	10.95	0.03	-9.576	84942	-0.102
UCAC2 24368261	15	1.966	84852	300	11830	11.09	0.03	-9.478	73139	-0.161
UCAC2 24368261	15	1.949	84860	299	10627	11.09	0.03	-9.476	73253	-0.160
UCAC2 24368261	15	1.929	86052	301	11902	11.09	0.03	-9.490	73384	-0.173
UCAC2 24368261	15	1.914	85368	300	11960	11.09	0.03	-9.479	73489	-0.163

Continued on next page

Table 10.6 – *Continued from previous page*

Object	$Texp$ (s)	Air mass	Count (ADU)	Count Uncertainty (ADU)	Peak Pixel (ADU)	R Mag	R Mag error	Inst cat per sec air of 1	Predicted Count (ADU)	Delta Mag
2MASS J15460525-1936371	15	1.966	38282	207	3491	11.23	0.1	-8.614	63278	0.546
2MASS J15460525-1936371	15	1.949	39050	209	3801	11.23	0.1	-8.634	63377	0.526
2MASS J15460525-1936371	15	1.929	38362	207	3550	11.23	0.1	-8.612	63489	0.547
2MASS J15460525-1936371	15	1.914	38957	209	3471	11.23	0.1	-8.628	63580	0.532
UCAC2 24368285	15	1.966	72642	278	13279	11.27	0.04	-9.309	60713	-0.195
UCAC2 24368285	15	1.949	72502	278	13617	11.27	0.04	-9.306	60808	-0.191
UCAC2 24368285	15	1.929	73722	280	12161	11.27	0.04	-9.322	60916	-0.207
UCAC2 24368285	15	1.914	73248	279	10463	11.27	0.04	-9.313	61003	-0.199
UCAC2 24368225	15	1.966	52160	239	5849	11.59	0.05	-8.950	43602	-0.195
UCAC2 24368225	15	1.949	50981	236	6122	11.59	0.05	-8.923	43670	-0.168
UCAC2 24368225	15	1.929	51360	237	6533	11.59	0.05	-8.929	43748	-0.174
UCAC2 24368225	15	1.914	51958	238	5862	11.59	0.05	-8.940	43811	-0.185
UCAC2 24368434	15	1.966	41983	216	6236	11.86	0.05	-8.714	32977	-0.262
UCAC2 24368434	15	1.949	41158	214	6971	11.86	0.05	-8.691	33028	-0.239
UCAC2 24368434	15	1.929	41469	215	7397	11.86	0.05	-8.697	33087	-0.245
UCAC2 24368434	15	1.914	42265	217	7300	11.86	0.05	-8.716	33134	-0.264
UCAC2 24368471	15	1.966	38155	207	6230	11.94	0.04	-8.610	30357	-0.248
UCAC2 24368471	15	1.949	38281	207	5415	11.94	0.04	-8.612	30405	-0.250
UCAC2 24368471	15	1.929	38137	207	5598	11.94	0.04	-8.606	30459	-0.244
UCAC2 24368471	15	1.914	37729	206	4929	11.94	0.04	-8.593	30502	-0.231
2MASS J14110426 +4701401	150	1.063	1386	198	836	17.20	0.35	-2.420	1429	0.034
2MASS J14110426 +4701401	150	1.068	1053	201	849	17.20	0.35	-2.123	1429	0.331
2MASS J14110426 +4701401	150	1.075	1126	201	897	17.20	0.35	-2.196	1428	0.258
2MASS J14110426 +4701401	150	1.083	1271	200	962	17.20	0.35	-2.328	1427	0.126
2MASS J14110426 +4701401	150	1.093	1691	200	943	17.20	0.35	-2.640	1425	-0.186
2MASS J14110426 +4701401	150	1.104	1693	203	966	17.20	0.35	-2.642	1424	-0.188
2MASS J14110426 +4701401	150	1.117	1176	206	906	17.20	0.35	-2.248	1422	0.206
2MASS J14110426 +4701401	150	1.132	1073	205	927	17.20	0.35	-2.149	1420	0.305
2MASS J14110426 +4701401	150	1.149	1669	204	927	17.20	0.35	-2.630	1418	-0.177
2MASS J14110426 +4701401	150	1.167	1482	202	966	17.20	0.35	-2.504	1416	-0.050
2MASS J14110426 +4701401	150	1.188	1449	198	914	17.20	0.35	-2.481	1413	-0.027
2MASS J14110426 +4701401	150	1.210	1496	194	896	17.20	0.35	-2.518	1410	-0.064
2MASS J14110426 +4701401	150	1.235	1448	191	750	17.20	0.35	-2.486	1407	-0.032
2MASS J14110426 +4701401	150	1.263	1258	186	724	17.20	0.35	-2.335	1403	0.119
2MASS J14110426 +4701401	150	1.294	1233	179	788	17.20	0.35	-2.316	1399	0.138
2MASS J14110426 +4701401	150	1.327	1336	157	581	17.20	0.35	-2.407	1395	0.047
2MASS J14110426 +4701401	150	1.497	1259	110	399	17.20	0.35	-2.360	1373	0.094
2MASS J14110426 +4701401	150	1.550	1594	111	393	17.20	0.35	-2.621	1367	-0.167
2MASS J14110426 +4701401	150	1.064	1155	197	861	17.20	0.35	-2.222	1429	0.232
2MASS J14110426 +4701401	150	1.070	1355	199	828	17.20	0.35	-2.396	1429	0.058
2MASS J14110426 +4701401	150	1.121	1033	206	1004	17.20	0.35	-2.107	1422	0.347

Continued on next page

Table 10.6 – *Continued from previous page*

Object	$Texp$ (s)	Air mass	Count (ADU)	Count Uncer-tainty (ADU)	Peak Pixel (ADU)	R Mag	R Mag error	Inst cat per sec air of 1	Pred-icted Count (ADU)	Delta Mag
2MASS J14110426 +4701401	150	1.271	1766	185	752	17.20	0.35	-2.704	1402	-0.250
2MASS J14110426 +4701401	150	1.302	1425	173	729	17.20	0.35	-2.475	1398	-0.021
2MASS J14110426 +4701401	150	1.510	1307	108	335	17.20	0.35	-2.402	1372	0.052
2MASS J14110426 +4701401	150	1.565	1371	112	420	17.20	0.35	-2.459	1365	-0.005
2MASS J14110426 +4701401	150	1.626	1212	115	334	17.20	0.35	-2.332	1357	0.122
2MASS J14110426 +4701401	150	1.065	1388	201	977	17.20	0.35	-2.423	1429	0.031
2MASS J14110426 +4701401	150	1.071	1199	200	898	17.20	0.35	-2.264	1428	0.190
2MASS J14110426 +4701401	150	1.079	1490	195	942	17.20	0.35	-2.501	1427	-0.047
2MASS J14110426 +4701401	150	1.088	1670	200	917	17.20	0.35	-2.625	1426	-0.171
2MASS J14110426 +4701401	150	1.098	1369	199	968	17.20	0.35	-2.411	1425	0.043
2MASS J14110426 +4701401	150	1.110	1225	204	999	17.20	0.35	-2.291	1423	0.163
2MASS J14110426 +4701401	150	1.124	978	203	888	17.20	0.35	-2.048	1421	0.406
2MASS J14110426 +4701401	150	1.140	1378	203	938	17.20	0.35	-2.422	1419	0.032
2MASS J14110426 +4701401	150	1.157	1030	199	873	17.20	0.35	-2.108	1417	0.346
2MASS J14110426 +4701401	150	1.177	1220	198	887	17.20	0.35	-2.293	1414	0.161
2MASS J14110426 +4701401	150	1.199	1401	197	864	17.20	0.35	-2.446	1412	0.008
2MASS J14110426 +4701401	150	1.223	1508	195	977	17.20	0.35	-2.528	1409	-0.074
2MASS J14110426 +4701401	150	1.249	1552	196	805	17.20	0.35	-2.562	1405	-0.108
2MASS J14110426 +4701401	150	1.278	1860	184	844	17.20	0.35	-2.761	1401	-0.307
2MASS J14110426 +4701401	150	1.310	1239	169	691	17.20	0.35	-2.323	1397	0.131
2MASS J14110426 +4701401	150	1.345	1301	144	554	17.20	0.35	-2.380	1393	0.074
2MASS J14110426 +4701401	150	1.523	1327	109	380	17.20	0.35	-2.420	1370	0.034
2MASS J14110426 +4701401	150	1.579	1258	111	412	17.20	0.35	-2.367	1363	0.087
2MASS J14110426 +4701401	150	1.642	1292	116	367	17.20	0.35	-2.402	1355	0.052
2MASS J14110426 +4701401	150	1.711	1310	150	546	17.20	0.35	-2.424	1347	0.030
2MASS J14110426 +4701401	150	1.067	952	197	949	17.20	0.35	-2.013	1429	0.441
2MASS J14110426 +4701401	150	1.073	1437	197	952	17.20	0.35	-2.461	1428	-0.007
2MASS J14110426 +4701401	150	1.081	1508	197	926	17.20	0.35	-2.514	1427	-0.060
2MASS J14110426 +4701401	150	1.090	1642	199	935	17.20	0.35	-2.607	1426	-0.154
2MASS J14110426 +4701401	150	1.101	2454	205	1115	17.20	0.35	-3.045	1424	-0.591

Continued on next page

Table 10.6 – *Continued from previous page*

Object	$Texp$ (s)	Air mass	Count (ADU)	Count Uncertainty (ADU)	Peak Pixel (ADU)	R Mag	R Mag error	Inst cat per sec air of 1	Predicted Count (ADU)	Delta Mag
2MASS J14110426 +4701401	150	1.114	1196	204	979	17.20	0.35	-2.265	1423	0.188
2MASS J14110426 +4701401	150	1.128	1109	203	968	17.20	0.35	-2.185	1421	0.269
2MASS J14110426 +4701401	150	1.144	1158	205	906	17.20	0.35	-2.234	1419	0.220
2MASS J14110426 +4701401	150	1.162	1326	201	901	17.20	0.35	-2.382	1416	0.071
2MASS J14110426 +4701401	150	1.182	1334	197	856	17.20	0.35	-2.391	1414	0.063
2MASS J14110426 +4701401	150	1.204	1164	196	934	17.20	0.35	-2.245	1411	0.209
2MASS J14110426 +4701401	150	1.256	1617	188	853	17.20	0.35	-2.607	1404	-0.153
2MASS J14110426 +4701401	150	1.286	1094	178	791	17.20	0.35	-2.186	1400	0.268
2MASS J14110426 +4701401	150	1.319	1478	164	619	17.20	0.35	-2.516	1396	-0.062
2MASS J14110426 +4701401	150	1.355	1567	137	548	17.20	0.35	-2.583	1392	-0.129
2MASS J14110426 +4701401	150	1.537	1415	110	371	17.20	0.35	-2.491	1368	-0.037
2MASS J14110426 +4701401	150	1.595	1486	111	472	17.20	0.35	-2.549	1361	-0.095
2MASS J14110426 +4701401	150	1.659	1155	121	421	17.20	0.35	-2.283	1353	0.171
2MASS J14110426 +4701401	150	1.730	1448	174	652	17.20	0.35	-2.535	1344	-0.081
GSC 04383-00633	180	1.865	87315	666	8969	13.00	∼	-6.801	122808	0.370
GSC 04383-00434	180	1.865	322808	824	29202	12.30	∼	-8.221	253351	-0.263
GSC 04383-00935	180	1.865	207549	749	18230	12.40	∼	-7.741	228452	0.104
GSC 04383-00094	180	1.865	80567	663	8458	13.20	∼	-6.714	99855	0.233
GPM 148.966758 +69.202551	180	1.865	144847	707	13276	13.10	∼	-7.351	110738	-0.292
GSC 04383-00322	180	1.865	23445	616	3737	14.50	∼	-5.373	26020	0.113
GSC 04383-00613	180	1.865	335927	834	31448	12.26	0.03	-8.264	264054	-0.261
[PR95] 50454	180	1.865	23905	616	3748	14.50	∼	-5.395	26020	0.092
GPM 148.510154 +69.115590	180	1.865	133685	699	13052	13.10	∼	-7.264	110738	-0.204
[PR95] 20127	180	1.865	32121	620	4467	14.00	∼	-5.715	43646	0.333
GSC 04383-01123	180	1.865	100376	682	11113	14.10	∼	-6.952	39357	-1.017
GSC 04383-00790	180	1.865	47801	635	5348	13.90	∼	-6.147	48403	0.014
UCAC3 318-46125	180	1.865	8216	610	2445	16.07	0.35	-4.235	5128	-0.512
[PR95] 40188	180	1.865	38834	628	4619	14.70	∼	-5.921	21157	-0.659
[PR95] 40174	180	1.865	13133	607	2834	15.30	∼	-4.744	11373	-0.156
GSC 04383-01028	180	1.865	104230	675	10202	13.00	∼	-6.993	122808	0.178
GPM 148.815133 +69.255798	180	1.865	396288	868	32024	12.20	∼	-8.443	280964	-0.373
[PR95] 20013	180	1.865	26969	619	3691	14.20	∼	-5.526	35489	0.298
GSC 04383-01023	180	1.865	36157	628	4779	14.10	∼	-5.844	39357	0.092
[PR95] 60021	180	1.865	36511	634	4882	14.70	∼	-5.854	21157	-0.592
GSC 04383-00244	180	1.865	229912	764	18727	12.30	∼	-7.852	253351	0.105
GPM 149.391696 +69.229356	180	1.865	101383	676	9697	13.40	∼	-6.963	81192	-0.241
GSC 04383-01005	180	1.865	83766	661	8671	13.10	∼	-6.756	110738	0.303
GSC 04383-00582	180	1.865	30520	620	4270	14.40	∼	-5.660	28856	-0.061
GSC 04383-00430	180	1.865	62357	644	6292	13.90	∼	-6.436	48403	-0.275
[PR95] 20031	180	1.865	32300	619	4479	14.20	∼	-5.721	35489	0.102
GPM 149.016337 +69.339459	180	1.865	127336	697	10913	13.20	∼	-7.211	99855	-0.264
TYC 4383-504-1	180	1.865	331580	835	27867	12.30	∼	-8.250	253351	-0.292
[OKN2006] H	180	1.865	205174	749	16620	12.70	∼	-7.729	167498	-0.220
UCAC4 797-019488	180	1.865	546686	953	41664	11.82	0.04	-8.793	416272	-0.296
TYC 4383-573-1	180	1.865	318935	821	28622	12.20	∼	-8.208	280964	-0.138
TYC 4383-767-1	180	1.865	474461	914	45036	11.80	∼	-8.639	424974	-0.120
[PR95] 30062	180	1.865	45402	640	5311	13.60	∼	-6.091	66017	0.406
GPM 149.799475 +69.097931	180	1.865	168804	723	15530	12.50	∼	-7.517	206000	0.216
GPM 149.634987 +69.264895	180	1.865	97809	672	9006	13.10	∼	-6.924	110738	0.135
GPM 149.345925 +68.789929	180	1.865	294540	810	29353	12.40	∼	-8.121	228452	-0.276
GPM 149.724929 +68.930312	180	1.865	55262	638	6571	13.80	∼	-6.304	53679	-0.032

Continued on next page

Table 10.6 – *Continued from previous page*

Object	$Texp$ (s)	Air mass	Count (ADU)	Count Uncer-tainty (ADU)	Peak Pixel (ADU)	R Mag	R Mag error	Inst cat per sec air of 1	Pred-icted Count (ADU)	Delta Mag
GPM 149.286779 +69.383037	180	1.865	218069	763	16708	12.70	∼	-7.795	167498	-0.286
UCAC2 19890828	60	1.840	109937	370	27101	12.46	0.07	-8.241	71734	-0.464

10.7 Website

The website was originally built so that the RTML code for the Bayfordbury telescopes could easily be created rather than manually writing it. Then it was noticed that transit predictions from other websites did not include any way of knowing how much out of transit time could be viewed. So the website was changed to display the user defined out of transit time.

The code originally started in PYTHON but was then rewritten into PHP code so that it could be used online.

The website code is written in PHP version 5.6. It also uses HTML, CSS and some JAVASCRIPT. A running version of the website can be viewed on
http://observatory.herts.ac.uk/exotransitpredict
The code is archived at GitHub
https://github.com/lukerobson/followup

The code has changed a lot over time to add new features and remove old code. It uses a function page that contains most of the code as well as an input page and output page.

At the start the code used the exoplanet list from exoplanets.org that had a CSV file that was then formatted to remove unnecessary details and turn some of the information into a different format.

The most notable, the mid-transit time of transit in JD, is converted into the start time of the transit in unix time. Transit time in minutes, RA and DEC converted into decimal format. Also, the period of the planet in days, transit depth in magnitude, magnitude of the star in V-band, name of the star and finally Log RHK value setting to zero if not available.

It was then noticed that there was sometimes a difference in transit time between the times produced from the data source and Exoplanet Transit Database. So multiple sources of information for the website that update from the source were added.

The prediction times have 2 types: *All* and *Single*. *All* finds the transits for all the exoplanets in that database during that period. The *Single* finds the transits for a particular exoplanet during that period.

Basic Functions

The *Next Transit* function is the key to the prediction of the transit times. It works out the next transit of the exoplanet between midday and the next midday for the location entered. It computes and saves when the sun will be out of the way (-18, -12, -6, -1 degrees below horizon) and the star will be above the minimum angle.

The *Get Data CSV* function selects which data source is going to be used and gets the data from it. There are two types, one for *Single* and the other for *All*.

The *Timeline* function produces a plot that shows the transits for each night on a timeline to see if two transits in a night can be observed.

The *Alt Az* function produces a plot to show the altitude and azimuth of the object over the transit. The *Find Now Time* function works out the local midday time for the location.

The functions *Table Make* that has 2 types, both of which do a similar thing of creating a table containing the transit information.

Peak pixel value

The Peak pixel value is important to know so that the saturation of the CCD is not reached based purely on the object that is being observed.

$$peakval = \frac{objcount}{2\pi(0.51 * seeingpx)^2} + bgcount \tag{10.1}$$

Where *objcount* comes from eq.2.15.

$$seeingpx = seeing/scale \tag{10.2}$$

Where scale comes from eq.1.1 and the seeing is based on the observation site and the conditions.

$$bgcount = (t_{\text{exp}} bgcount) + pedestal \tag{10.3}$$

Where *pedestal* is 70 and *bgcount* is based on the sky background count per second.

The user selects the exposure time and enters the magnitude of the star in the filter and the website will output the peak pixel value. This helps select the exposure time so that the saturation of the CCD is not reached.

Predicted Plots

The website can create a predicted plot based on the transit details and predicted precision. The trapezoidal transit model is used as the basis of the plot so that only the transit time and depth is needed for it to be worked out. An assumption that it uses is that the first contact to second contact and the third contact to fourth contact are a quarter each of the total transit time. So the second contact to the third contact is half the transit time.

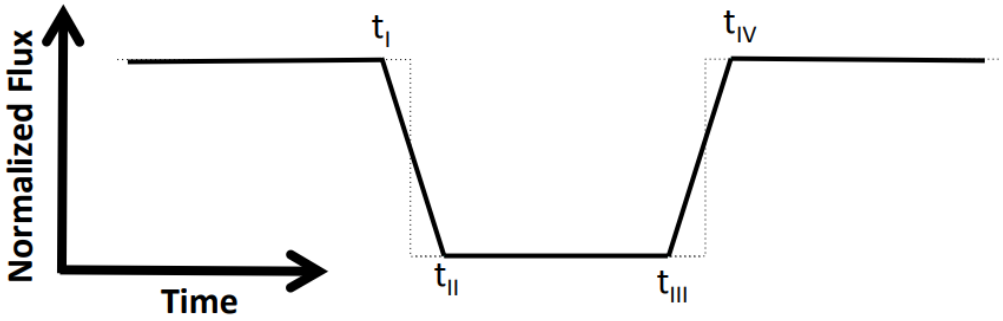

Figure 10.3: Plot showing the trapezoidal transit model and the four contact positions from Agol (2012)

Then it uses the exposure time and time separation between the images to work out the number of images before, during and after the transit.

Then using the predicted precision, a random number between 0.035 and 0.965 and a normal distribution function, the predicted precision is turned into a standard deviation between about -2.5 and 2.5. This is then multiplied by the predicted precision and then added to the value of the trapezoidal model for that time. The used predicted precision is then the uncertainty in the value.

Due to the random numbers used each time, the plots cannot be recreated unless the data is saved. As transit depth, transit duration, magnitude of star all vary and with different exposure times, this can be used to help work out which of the many available transits should be observed and for what exposure time.

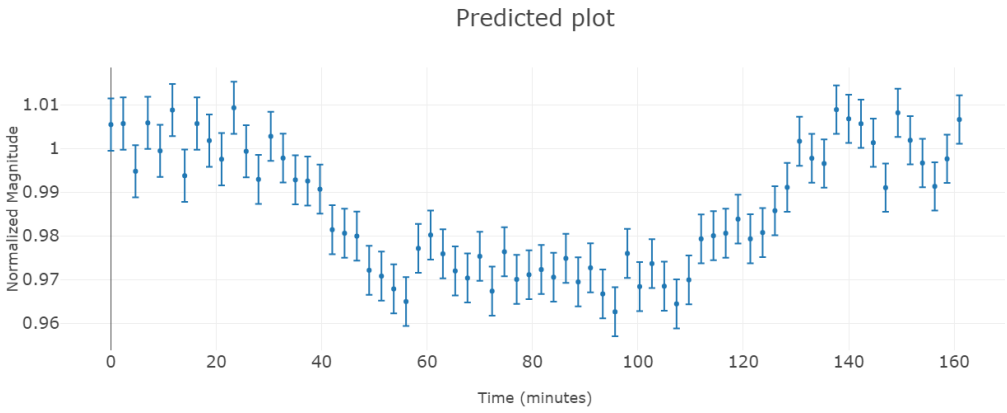

Figure 10.4: Example of the predicted plot for WASP-52 b with the CKT and a 90 second exposure

Error Plots

The website is able is produce a lot of different plots based on the predicted precision and the peak pixel value.

1. Magnitude vs Exposure time vs Uncertainty plot (3D surface)
2. Magnitude vs Exposure time vs Uncertainty - with set value (3D surface)
3. Magnitude vs Exposure time vs Uncertainty plot with seeing (3D surface)
4. Magnitude vs Air mass vs Uncertainty plot (3D surface)
5. Magnitude vs Error type vs Uncertainty (2D multiple lines)
6. Error type vs Magnitude (2D)

Figure 10.6 shows the breakdown of the errors for the CKT in V. There are jumps in the errors as the exposure time changes over. It uses 1, 2, 3, 4, 5, 10, 15, 20, 30, 45, 60, 90, 120, 180 and 300 seconds exposure time. There are 6 entries, but bias and dark are so small in percentage that they do not display with sky, only appearing as the target's brightness approaches the sky background magnitude. In the key for figure 10.6 the total counts is refereed to as total.

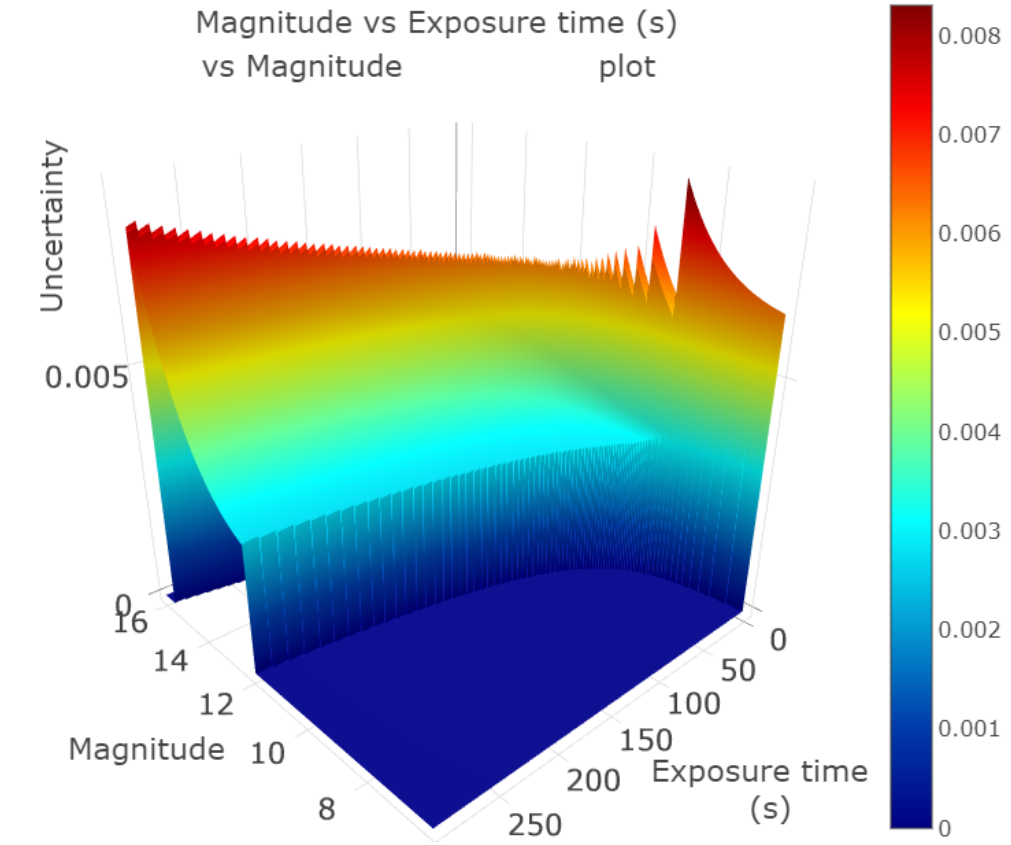

Figure 10.5: Magnitude vs Exposure time vs Uncertainty plot (3D surface)

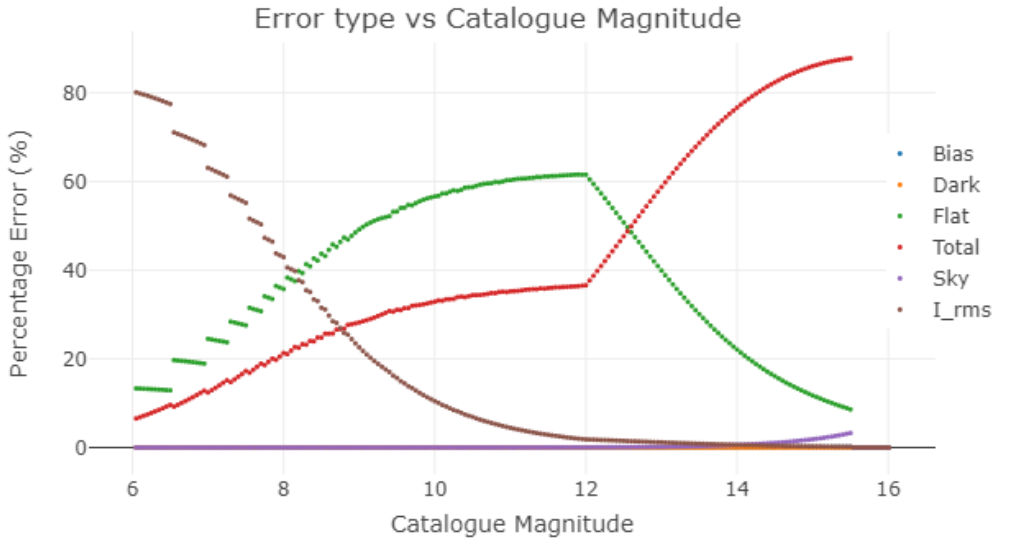

Figure 10.6: Error type vs Magnitude (2D)